LATVIAN JOURNAL of PHYSICS and TECHNICAL SCIENCES

ISSN 0868 - 8257

4

(Vol. 62)

2025

CONTENTS

D. Haritonova, A. Zarins, A. Rubans
Reconfigurable Optical System for Space Object Tracking 3

D. Bozorova, S. Gofurov, M. Ziyayev, A. Kokhkharov,
Z. Kadirova, O. Abdiraimova, O. Ismailova
Heteremolecular Structure Formation in Binary Solutions of Dimethylformamide-Water and Tetrahydrofuran-Water: FTIR and Refractometry 14

G. Valdmanis, L. Zemite, D. Kronkalns, L. Jansons
Transport Poverty: An Urgent Issue in the Future of the EU Climate and Energy Policy 29

T. Rohman, S. F. Junjunan, M. A. Moelyadi
Investigation of Pertamax (Gasoline) Pool Fire in Confined Compartment 46

G. G. Ismayilov, F. B. Ismayilova, A. R. Nagizadeh
Analysis of Structural Reliability of Main Gas Pipelines 57

K. Belovs, N. Kocanovs, R. Kocanova, I. Geipele, J. Naimaviciene
Strategic Development Areas of the Latvian Road Building Industry 65

N. Nutt, L. Nei, M. Olle
Using Chalk Instead of Paints in Paper Plaster 80

A. M. Abd El-Hameed, A. S. Farahat, L. H. Basmsm
A Report on the Sources used for LEO Plasma Experimental Simulation 87

LATVIAN JOURNAL of PHYSICS and TECHNICAL SCIENCES

LATVIJAS FIZIKAS un TEHNISKO ZINĀTŅU ŽURNĀLS

Published six times a year since February 1964
Iznāk sešas reizes gadā kopš 1964. gada februāra

4 (Vol. 62) • 2025

RĪGA

Language Editor: O. Ivanova
Computer Designer: I. Begicevs

INDEXED (PUBLISHED) IN

www.scopus.com
www.sciendo.com
EBSCO (Academic Search Complete, www.epnet.com), INSPEC (www.iee.org.com).
VINITI (www.viniti.ru), Begell House Inc/ (EDC, www.edata-center.com).

Issuers: Institute of Physical Energetics,
Institute of Solid State Physics, University of Latvia
Registration Certificate Number: 000700221

Editorial Contacts:
14 Dzerbenes Street, Riga, LV-1006
LATVIA
tel: +371 26245896
M: +371 29363105
leo@lza.lv

sciendo

LATVIAN JOURNAL OF PHYSICS
AND TECHNICAL SCIENCES
2025, N 4

DOI: 10.2478/lpts-2025-0025

RECONFIGURABLE OPTICAL SYSTEM FOR SPACE OBJECT TRACKING

D. Haritonova*, A. Zarins, A. Rubans

Institute of Geodesy and Geoinformatics,
University of Latvia
3 Jelgavas Str., Riga, LV-1004, LATVIA
*e-mail: diana.haritonova@lu.lv

The growing quantity of space debris poses a serious hazard to functioning satellites. Mitigating space debris is critical to ensure the safe and sustainable use of space in Earth's orbit. Near-Earth objects such as asteroids can pose a serious threat to infrastructure and life on the ground. As space debris and near-Earth object observation communities use similar techniques and processes to measure space objects, the need for synergy is growing. This paper presents the ability of small sensors to detect and track such objects using the implemented technology – CCD image stacking in equatorial coordinates. The experimental optical system is intended for both positional astrometric and laser ranging observations – its optical scheme is reconfigurable. Here we provide the technical characteristics of the system and a description of its functionality using comprehensive control and analysis software. We propose a method of image stacking, which has several advantages in searching space objects by different optical systems and their combinations. This method enables increasing the brightness of space objects, visualizing their motion relative to stars, and stacking images obtained by optical systems with different technical parameters.

Keywords: *Charge-coupled device, near-Earth objects, optical sensors, space debris, tracking.*

1. INTRODUCTION

The rapid expansion of human space activities has significantly increased the quantity of space debris in Earth's orbital environment. This poses a serious threat to all space operations and exploration missions [1]. The development of automated algorithms for detecting space objects has become a subject of interest. The importance of these algorithms lies in their accuracy, speed, repeatability, and maximum objectivity and is apparent in many fields and large surveys.

The acquisition of space debris orbital data through observations is critical. Current ground-based tracking systems of space surveillance networks (SSN) include the use of radars and passive-optical and active-optical telescopes for cataloging and characterising space debris. Lasers are extremely precise but have limitations in terms of the energy of emitted pulses, which is important for targets without retroreflectors and a relatively small field of view [2], [3]. Passive-optical systems, which are used mainly to determine the astrometric position of an object, are of considerable importance in many applications [4]–[6]. Observation by such systems is a well-suited method for monitoring the geosynchronous protected region [7].

Progress in imaging technologies has changed the properties of the star position measurement process. Currently, CCD matrices provide high sensitivity and allow immediate astrometric processing, and the accuracy and number of star coordinates substantially increase. This ensures fast and efficient methods for the precise identification of space objects for different observation communities.

Here, we provide the technical characteristics of an experimental optical tracking system (OTS), which is designed as an alternative to custom-made systems. We propose a method of CCD image stacking implemented in equatorial coordinates, which increases the efficiency of capturing space debris and faint near-Earth objects (NEOs) via different optical systems and their combinations.

2. CONCEPTUAL AND EXPERIMENTAL PART

2.1. Concept and Design of OTS

The OTS includes twin receiving optical tube assemblies (OTAs), which are symmetrically set on an Alt-Alt mount (Fig. 1). This type of mount ensures continuous tracking of objects in different regions of the sky, unlike Alt-Az and equatorial mounts, which have 'blind spots' in the zenith and celestial pole, respectively. The system's optical scheme is reconfigurable. The design implies that one OTA is equipped with a CCD matrix and that the other OTA can be fitted with a laser collimator and a reflected light pulse detector for satellite laser ranging (SLR) purposes or with other instruments.

The following configurations of the OTS are most promising:

- one or both OTAs are equipped with a CCD for positional astrometric observations;

- one OTA with an analogue signal receiver (e.g., PMT – photomultiplier tube) for registration of reflected SLR pulses, another OTA with a digital receiver (CCD) for visual guidance;
- both OTAs are equipped with analogue signal receivers for registration of reflected SLR pulses in the coincidence scheme or the gate and window scheme (in noisy environments).

Fig. 1. Assembly of the optical tracking system.

Each OTA has an advanced coma-free (ACF) 0.41 m F/10 optic (focal length: 4 m) with a high transparency coating.

The drive of the mount has two stepper motors with wormwheel gearboxes and two incremental encoders. It is controlled by the FPGA. Technical parameters are summarised in Table 1.

Table 1. Technical Specifications of the Mount

Description	Technical parameters
Stepper motor drive	200 steps/rev, up to 256 mkstep/step
1:85 wormwheel gearboxes	with about 10–15 arcsec backlash
Drive resolution	up to 0.32 arcsec/mkstep
18 000 division (72 arcsec) relative encoders	with up to 100 x interpolation
Encoder pulse resolution	up to 0.36 arcsec, accuracy 2–3 arcsec
Slewing speed	up to 5–10 dg/s
Tracking speed	up to 2 dg/s
Mount control software: Windows PC via FPGA	up to 1000 control cycles/sec

The OTS design outline and its control parts are shown in Fig. 2. Descriptions of all numbered components are given in Table 2.

One of the principal design goals for

the system is laser ranging capability. The laser ranging in automatic (blind) mode requires a pointing accuracy exceeding the divergence of the transmitted beam. As subarcminute beam divergence is a common choice for ranging distant objects, the pointing accuracy should be within a few arcseconds. Therefore, an error model must be applied in the control software to introduce the necessary pointing corrections.

The system is now equipped with two CCD matrices for astrometric observations: 8.3 Mpix (3326 × 2504) and 16.8 Mpix (4096 × 4096) CCD matrices. A more advanced model ensures a field of view of 0.5° × 0.5° with a minimum pixel size of 0.46 arcseconds.

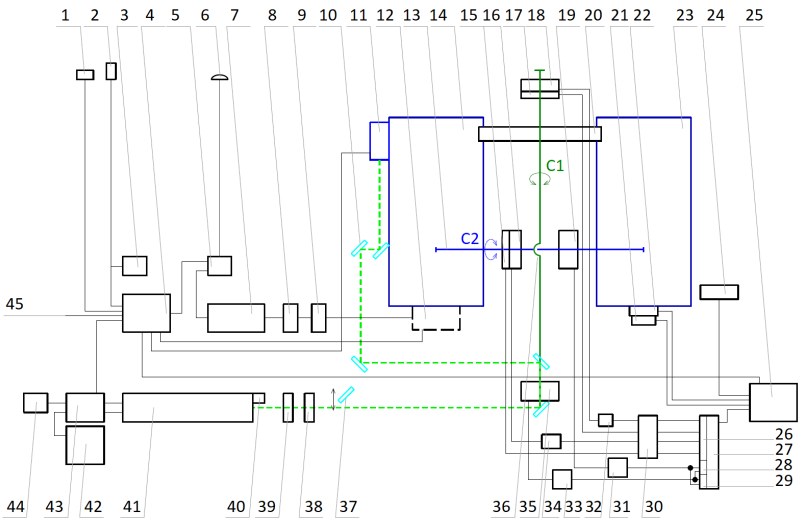

Fig. 2. OTS design scheme. The primary rotation Axis C1 is shown in green, and the secondary rotation Axis C2 is shown in blue. The Coudé path for the transmitted laser beam enters along C1. The transmitting collimator is attached to the side of the receiving OTA. Descriptions are given in Table 2.

Table 2. Descriptions of the Numbered Components of the OTS Design Scheme

No	Item	No	Item	No	Item
1	All sky camera	16	Encoder II	31	Power unit II
2	Meteo sensor	17	Limit and zenith switch I	32	IBV 102 I
3	Digital barometer	18	Encoder I	33	Power unit I
4	PC I	19	Drive II	34	IBV 102 II
5	GNSS receiver	20	Tie	35	Drive I
6	GNSS antenna	21	CCD sensor	36	Rotation Axis I (C1)
7	Event timer	22	Microfocuser	37	Adjustment mirror
8	CFD	23	OTA II	38	Filter set
9	Filter set	24	Dome control	39	SHG
10	Laser beam path	25	PC II	40	Infrared detector
11	Optical transmitter	26	Slot CN4 CN6	41	Laser
12	Analog receiver	27	PC extension board	42	Cooling unit I
13	Rotation Axis II (C2)	28	Slot CN3	43	Cooling unit II
14	OTA I	29	Slot CN5	44	Manual control keyboard
15	Limit and zenith switch II	30	TTL/LVTTL board	45	Internet

2.2. Control and Analysis Software

The control software is developed using MS VisualStudio C++ and C#. This software consists of several semiautonomous modules supporting positioning, astrometry, ephemeris, and SLR functionality.

The positioning (mount control) module uses angular encoders to determine the current positions of the OTS; it calculates the step frequency needed to track the object and controls mount motor step pulse generation. GNSS event timing can be used for tracking purposes and acquisition of the CCD image exposure time. The object tracking process uses a motion model, which is based on a precalculated (by the ephemeris module for satellites or by the astrometry module for stellar objects) polynomial approximation of the topocentric horizontal rectangular coordinate dependency on time. The values of the target coordinates are calculated and corrected by the mount error model in real time.

a)

b)

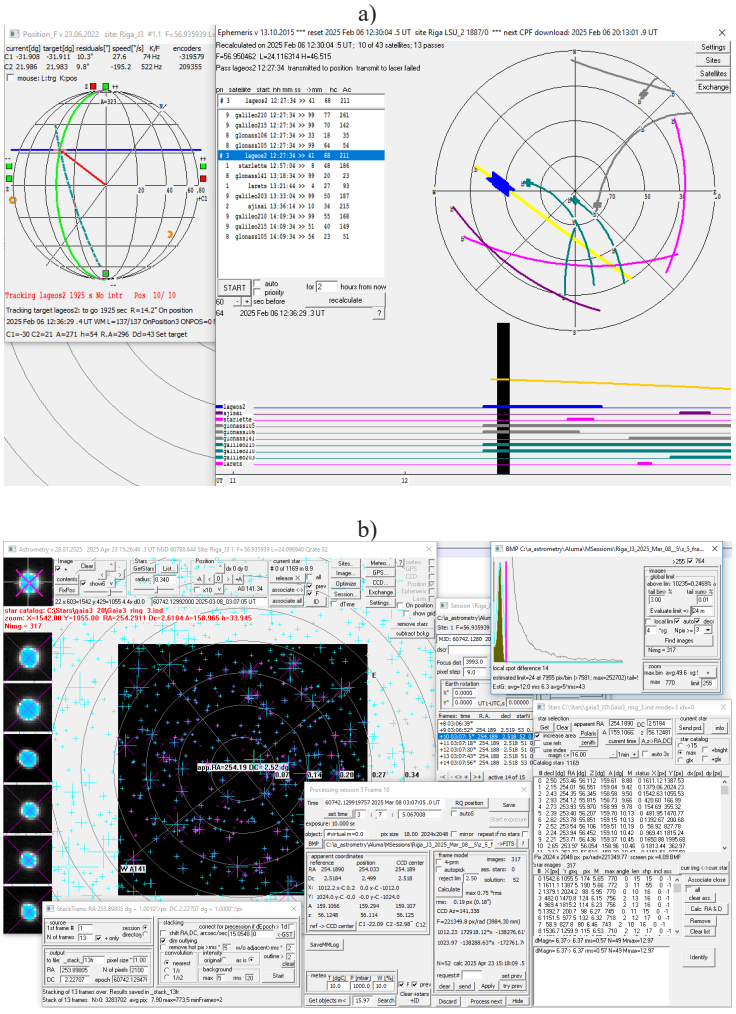

Fig. 3. Software interfaces: a) positioning and ephemeris modules; b) astrometry module.

Ephemeris is a separate module (see Fig. 3a) for satellite prediction data acquisition and management, tracking model generation, situation visualization, and providing current pass prediction to the positioning module. The module uses the consolidated prediction format (CPF) as a data source. Other data sources and formats, e.g., the two-line element set (TLE) format, can also be implemented.

The functions of the module responsible for SLR functionality include control of the event timer and collimator's divergence, as well as control of the receiver's diaphragm and filter wheel. It ensures the collection, analysis, and storage of calibration data and laser ranging data, as well as the generation and export of normal point data.

The astrometry module supports image acquisition and near-real-time analysis (see Fig. 3b). It controls the CCD camera settings, contrast enhancement, and object image recognition, ensures reference star selection and identification, and determines the object coordinates. The module includes the vector astrometry software package NOVAS for calculating the apparent places of stars [8]. A subset of the Gaia star catalog (data release EDR3), consisting of astrometry and star magnitude data for stars brighter than magnitude 21, is used.

2.3. Image Stacking Method

Astronomical images are usually stacked to detect moving space objects or to produce a single image of a faint object with a superior signal-to-noise ratio. As all the summed pixel intensities contain a random noise component, stacking leads to a relative decrease in the noise level (up to a factor of $1/\sqrt{N}$) [9], resulting in better contrast of the target object. In common practice, image stacking is performed by comparing patterns on frames or directly overlaying images, and it requires images obtained using the same optics and under similar circumstances.

We propose a method of CCD image stacking implemented in equatorial coordinates. This allows stack images, which have different scales, distortions, framing and epochs. The method requires an astrometric solution for all involved images, i.e., transformation from image (pixel) coordinates to equatorial coordinates. The stacking mechanism is based on the calculation of coinciding positions on source images via a frame astrometric model. The stacked image is generated in a rectangular coordinate system, with coordinates of right ascension and declination.

3. TEST RESULTS AND DISCUSSION

To ensure correctness of star identities and sufficient accuracy of the astrometric solution, several tens or more stars are beneficial (see Fig. 4a). For the used set of instrumentation typical RMS of astrometric solution is 0.2–0.4 arcseconds at pixel size close to 1 arcsecond. Figure 4b shows the effect of the number of reference stars used within various solutions (from 6 up to 85 stars were used) on the position of a test star selected close to the centre of the frame.

According to Fig. 4a, RMS of astrometric solution slowly decreases with an increasing number of reference stars starting from 20 stars. For less than 20 reference stars considerable wandering of RMS values is observed; low RMS values in the case of 6–7 stars are caused by partial absorption

of random measurement errors in astrometric model parameters. This is also reflected in more pronounced wandering of the test star's position in Fig. 4b. However, the wandering does not exceed 0.1 arcseconds even for the case of 6 reference stars. Similar results, with wandering up to 0.2 arcseconds, were obtained also for locations of test stars on the edges of the frame. Such accuracy is quite satisfactory for the purposes of image stacking.

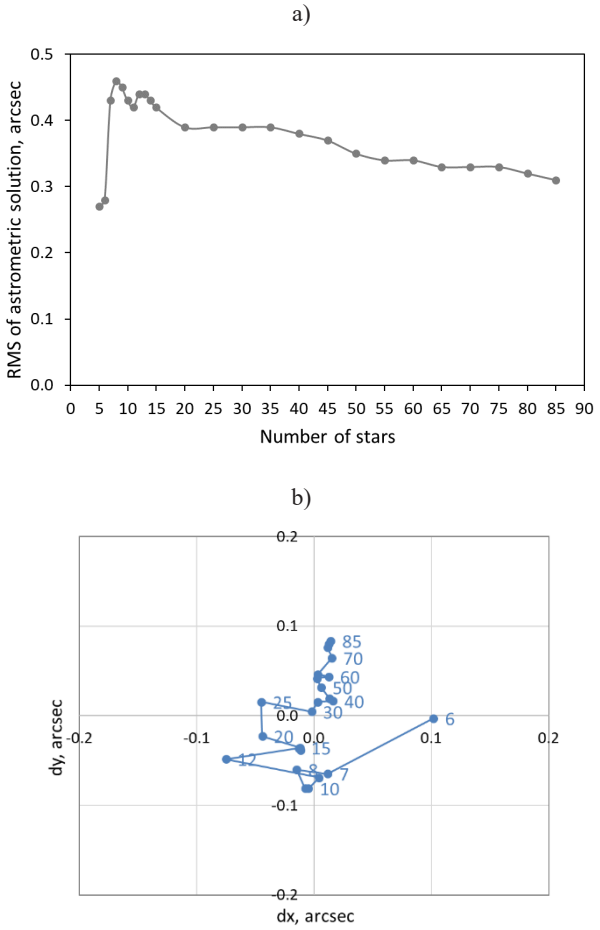

Fig. 4. a) RMS of astrometric solutions using increasing number of reference stars on the frame; b) Positions of selected star on the frame within different astrometric solutions with reference stars from 6 up to 85 (number of stars is indicated).

3.1. Geostationary Satellite Detection and Tracking

Figure 5 shows an example of an image stacking application for satellite observations in the geostationary Earth orbit (GEO). The frames are taken in static mode with 0.8 s exposures. Notably, the northern geographical location of the OTS means that the geostationary arc is only approximately 25° above the horizon and that an arc of approximately 50° is observable. In this case, the advantage of the method is the improved RMS value of the astrometric fit compared to that of single-frame solutions.

However, limitations may be related to the exposure time. Long streaks of star images make the identification process less accurate [10].

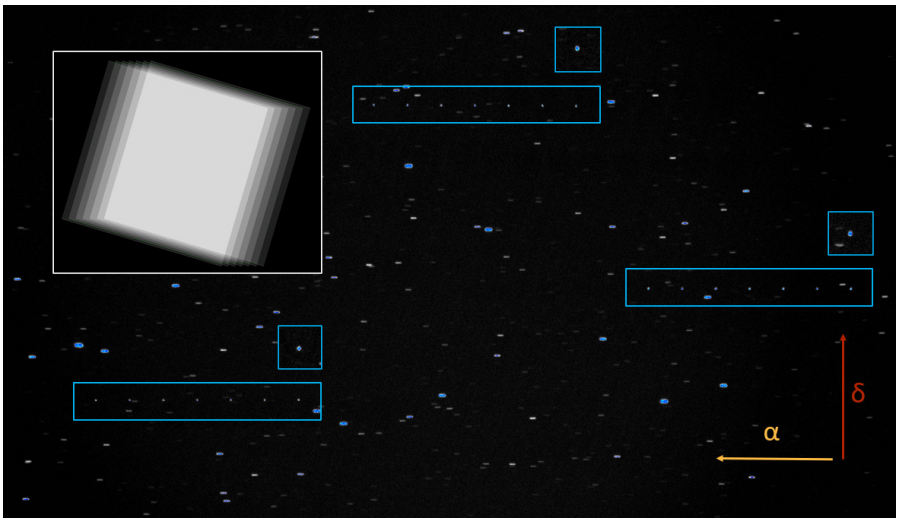

Fig. 5. Stack of 7 0.8-s frames in the region of the geostationary arc (31.5° E point) with three captured satellites; the image in the blue square is a stacked image (the scale is the same) of 7 single images of each GEO satellite.

To increase the brightness of small objects, e.g., pieces of GEO debris, stacking should be combined with the method of image shifting. Here, this is realised via the known rate of Earth rotation. Figure 5 shows the image in the blue square, which is a stacked image (the scale is the same) of 7 single images of each satellite applying the shifting technique. This allows increasing the brightness of an object. Thus, it is possible to detect space debris, which is not visible on a single CCD frame.

According to past and ongoing GEO surveys, in most cases, optical telescopes with diameters of 1 m or less were used, with sensitivity limits in the magnitude range of 15–20, corresponding to objects larger than 15 cm [11]. Using such systems for observation and applying methods of image stacking and shifting could increase the brightness of fainter GEO objects and detect their positions.

3.2. NEO Detection and Tracking

Current NEO survey programs such as Pan-STARRS and CSS (Catalina Sky Survey) usually conduct observations via the same strategy and data analysis process; several CCD images with exposure times of up to a few minutes are taken and compared to detect moving NEOs. The proposed method of image stacking has advantages over such an observation strategy: it increases the brightness of the asteroid during one session with a set of consequent images with relatively short exposure, i.e., it prolongs the "effective exposure time" of the object, and representatively shows the trajectory of its movement during the entire observation period.

Figure 6 presents an example of an image stacking application for asteroid observation. This is a stack of 25 5-s frames obtained in star-tracking mode during a 5-hour period in five batches.

Fig. 6. Stack of 25 5-s images with moving asteroid during a 5-h period. The orientations and overlaps of the images are shown.

The resulting stacked image allows for the detection of faint NEOs and the determination of their coordinates. Additionally, it is possible to combine images obtained by several telescopes simultaneously to increase the brightness of small and fast-moving NEOs, which cannot be detected via common observation strategies.

3.3. A Combination of Frames from a Set of Sensors

Figure 7 shows an example of stacking using images obtained by two CCD cameras simultaneously. The streak is a satellite observed by the OTS in static (not tracking) mode. This proves that the use of equatorial coordinates enables the processing and stacking of optical frames of various origins, with different orientations of the CCD matrices and different scales and distortions of images.

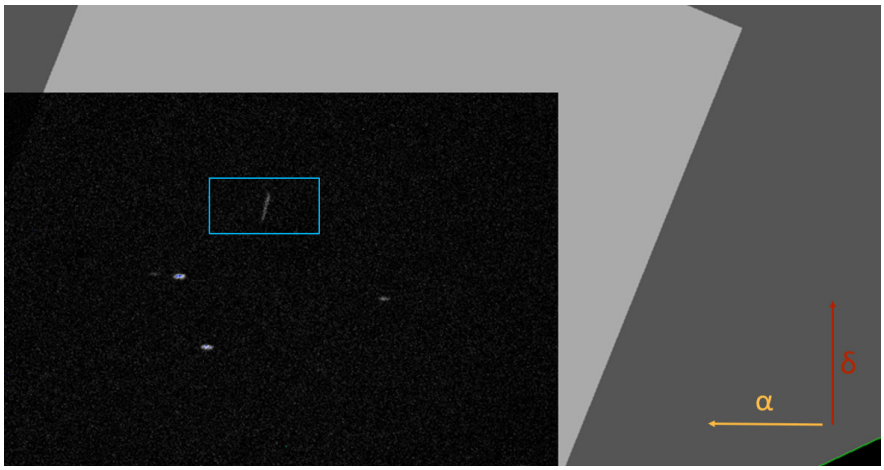

Fig. 7. Stack of 2 1-s images obtained by both cameras of OTS simultaneously, with a satellite streak.

If input frames have different source parameters, the question of differentiating their weights in the stacked frame arises. In this case, an estimate of the effective light flux (product of the exposure time, telescope aperture area, and sensitivity factor) can be used. This is implemented in our software, but other options are possible. More experimental results obtained by different optical systems are needed to evaluate this choice.

Stacking images from a set of sensors could be useful for detecting and tracking objects in low Earth orbit (LEO), which results in increased risks of collisions due to the high density of orbital debris [6], [12]. Combining images from multiple sensors simultaneously can increase the brightness of faint streaks of debris.

4. CONCLUSIONS

In this paper, the design of a combined active and passive optical measurement system has been presented with experimental results obtained via the new method for astronomical imaging, i.e., the method of CCD image stacking in equatorial coordinates.

We have shown that it has several advantages in tracking and detecting space objects and can be adapted for various observation strategies: in star or target tracking mode or in static mode. The main strengths are the ability to increase the brightness of faint objects via small sensors and the ability to combine images obtained by multiple optical systems, ensuring the detection of small and fast-moving objects. As such stacking requires the presence of astrometric solution for all source frames, an effect of small number of reference stars on accuracy of stacking was evaluated. We have found that for stacking purposes accuracy is quite satisfactory even for very few (10–20) reference stars per frame. More results obtained via different optical systems and their combinations are needed to fully evaluate the effectiveness of the proposed method.

ACKNOWLEDGEMENTS

The research has been financed by the Recovery and Resilience Facility project "Internal and External Consolidation of the University of Latvia", No. 5.2.1.1.i.0/2/24/I/CFLA/007, Agreement No. LU-BA-PG-2024/1-0004.

The preparation of the optical tracking system for observations has been supported by the European Regional Development Fund activity "Postdoctoral Research Aid", No. 1.1.1.2/VIAA/4/20/619. Valuable support has been given by MikroTik and the University of Latvia Foundation in the procurement of a new CCD matrix and focuser, project No. 2283.

REFERENCES

1. Inter-Agency Space Debris Coordination Committee. (Jan., 2025). *Space Debris Mitigation Guidelines*. IADC-02-01 Revision 4.

2. Rodriguez-Villamizar, J., Cordelli, E., & Schildknecht, T. (2021). The Stare and Chase Observation Strategy at the Swiss Optical Ground Station and Geodynamics Observatory Zimmerwald: From Concept to Implementation. *Acta Astronaut., 189*, 352–367. DOI: 10.1016/j.actaastro.2021.08.032
3. Wagner, P., Hampf, D., Sproll, F., Hasenohr, T., Humbert, L., Rodmann, J., & Riede, W. (2016). Detection and laser ranging of orbital objects using optical methods. *Proc. SPIE* 9977, *Remote Sens. Sys. Eng. VI*, 99770D. DOI: 10.1117/12.2236919
4. Danescu, R. G., Itu, R., Muresan, M. P., Rednic, A., & Turcu, V. (2022). SST Anywhere – A Portable Solution for Wide Field Low Earth Orbit Surveillance. *Remote Sens.*, *14* (8), 1905. DOI: 10.3390/rs14081905
5. Yanagisawa, T., Kamiya, K., & Kurosaki, H. (2021). New NEO Detection Techniques using the FPGA. *Publ. Astron. Soc. Jpn*., *73* (3), 519–529. DOI: 10.1093/pasj/psab017
6. Wagner, P., & Clausen, T. (2022). APPARILLO: A Fully Operational and Autonomous Staring System for LEO Debris Detection. *CEAS Space J.*, *14* (2), 303–326. DOI: 10.1007/s12567-021-00380-6
7. Schildknecht, T. (2007). Optical Surveys for Space Debris. *Astron. Astrophys. Rev*., *14* (1), 41–111. DOI: 10.1007/s00159-006-0003-9
8. Kaplan, G. H. (2005). *The IAU resolutions on astronomical reference systems, time scales, and Earth rotation models*. USNO Circular No. 179, Washington, D.C. 20392.
9. Zhang, Y., Wang, J., Su, J., Cheng, X., & Zhang, Z. (2021). Astrometric Observations of a Near-Earth Object Using the Image Fusion Technique. *Astron. J.*, *162* (6), 250. DOI: 10.3847/1538-3881/ac2c6f
10. Kouprianov, V. (2008). Distinguishing Features of CCD Astrometry of Faint GEO Objects. *Adv. Space Res*., *41* (7), 1029–1038. DOI: 10.1016/j.asr.2007.04.033
11. Blake, J. A., Chote, P., Pollacco, D., Feline, W., Privett, G., Ash, A., … & Watson, C. (2021). DebrisWatch I: A Survey of Faint Geosynchronous Debris. *Adv. Space Res*., *67* (1), 360–370. DOI: 10.1016/j.asr.2020.08.008
12. Cegarra Polo, M., Yanagisawa, T., & Kurosaki, H. (2022). Real-Time Processing Pipeline for Automatic Streak Detection in Astronomical Images Implemented in a Multi-GPU System. *Publ. Astron. Soc. Jpn*., 74 (4), 777–790. DOI: 10.1093/pasj/psac035

sciendo

LATVIAN JOURNAL OF PHYSICS
AND TECHNICAL SCIENCES
2025, N 4

DOI: 10.2478/lpts-2025-0026

HETEREMOLECULAR STRUCTURE FORMATION IN BINARY SOLUTIONS OF DIMETHYLFORMAMIDE-WATER AND TETRAHYDROFURAN-WATER: FTIR AND REFRACTOMETRY

D. Bozorova[1,2]*, S. Gofurov[2], M. Ziyayev[3], A. Kokhkharov[1],
Z. Kadirova[2,4,5], O. Abdiraimova[4], O. Ismailova[1,2,6]

[1]Institute of Ion-Plasma and Laser Technologies,
33 Durmon Yuli Str., Tashkent, 100125, UZBEKISTAN
[2]Uzbekistan-Japan Innovation Center of Youth,
2B University Str., Tashkent 100195, UZBEKISTAN
[3]Namangan State University,
Namangan, 160107, UZBEKISTAN
[4]National University of Uzbekistan named after Mirzo Ulugbek,
4 University Str., Tashkent 100174, UZBEKISTAN
[5]Tashkent Institute of Chemical Technology,
32 Navoi Str., Tashkent, 100011, UZBEKISTAN
[6]Turin Polytechnic University in Tashkent,
17 Little Ring Road, Almazar district, Tashkent, 100195, UZBEKISTAN
*e-mail: bozorova191@gmail.com

Along with other works that employ a more complex and time-consuming approach to analyse the formation of heteromolecular structures in aqueous solutions of dimethylformamide and tetrahydrofuran, we propose a new technique based on the combined use of refractometry and IR spectroscopy. The formation of intermolecular complexes is analysed by measuring the excess refractive index and the ratio of OH absorption bands of bound molecules to those of free ones in the concentration range of 0÷1 mole fraction of components. It has been shown that the formation of heteromolecular structures occurs within a narrow concentration range of 0.3 to 0.4 mole fractions of dimethylformamide and tetrahydrofuran, which corresponds to the maximum number of realized hydrogen bonds in the dimethylformamide-water and tetrahydrofuran-water systems.

Keywords: *Excess refractive index, heteromolecular structures, infrared spectroscopy.*

1. INTRODUCTION

There are various experimental methods for investigating the properties of water and aqueous-organic solutions: dielectric [1], [2] and infrared spectroscopy [3]–[11], Raman spectroscopy [12]–[15], and terahertz spectroscopy [16]–[20], X-ray diffraction [21]–[23], neutron diffraction [24]–[28], proton magnetic resonance spectroscopy [29]–[31] and others. All these methods are highly sensitive to various structural and relaxation changes in molecules of liquids, allowing to establish specific mechanisms of their mutual dissolution in a wide range of component concentrations and solution temperatures and to register the formation of mono- and heteromolecular associates in solutions, as well as clathrate formations in aqueous mixtures almost any organic solvents.

Establishing a connection between the kinematic, dynamic, and spectral characteristics of molecules allows for a deeper understanding of the mechanism of intermolecular interactions in each particular case.

Understanding the processes of hydrogen bond formation plays a significant role in determining the structure and physicochemical properties of many structures and materials, and is intensively studied in physics, chemistry, biology, and interdisciplinary research. Systems with hydrogen bonds find use in various applied studies, for example, in crystal design [30], [31], [32], in the creation of systems with self-assembly [33], [34] and molecular recognition [35], [36], in hydrothermal synthesis [37], [38] and others.

For example, in [39], it was assumed from the similarity of the shapes of the OH group valence vibration lines in CCl4 solutions that such mixtures form complexes in an aprotic medium, but no direct evidence of the stoichiometry of the complexes was presented. Non-valent interactions in solution can also be studied by NMR [40]–[43] and vacuum ultraviolet spectroscopy [44]–[46]. In particular, the signals of protons involved in the formation of hydrogen bonds are usually shifted to a rather weak field. The difficulty of studying such systems like NMR spectroscopy lies in the rapid molecular and proton exchange, as a result of which chemical shifts are averaged over a set of all complexes and monomers coexisting in solution, as well as over an ensemble of possible hydrogen bonding geometries.

It should be noted that the choice of double aqueous-organic mixtures of water + dimethylformamide and water + tetrahydrofuran as the subject of research is due to their wide practical use in chemical synthesis [48]–[50], optical spectroscopy [51]–[54], EPR spectroscopy [55], [56], and high-performance liquid chromatography as mobile phases [57]–[60].

The refractometric parameters and their excess values make it possible to understand structural changes in binary and ternary solutions and provide valuable information about intermolecular interactions [61]–[63]. Thus, a review of the literature shows that there are no reports studying the combination of infrared spectroscopy and refractometry for aqueous solutions of dimethylformamide (DMF) and tetrahydrofuran (THF).

So far, in most studies, the information extracted from IR spectra has been obtained from the position of absorption bands, thus determining the main vibrational modes characteristic of individual molecules of mixtures. It was difficult to

interpret the absorption bands due to the overlap of nearby bands and the insufficient resolution of individual bands, associated with the need to increase the resolution in the IR spectra, which led to the impossibility of obtaining information on the formation of clusters, analysis of hydrogen bonds. Therefore, such information was obtained using other methods: dielectric permittivity [63]–[65], total isotropic Rayleigh scattering of coherent light [66]–[68], viscosity [69], [70], and excess molar mixing volume [71]–[74]. With the intensive development of modern interferometer devices, the time scale of spectrum recording has reduced dramatically from several minutes to seconds and the sensitivity of the method has increased significantly, allowing for obtaining information on intensities, half-widths, isotopic shifts, and other finer spectral parameters.

This work focuses on the investigation of structure formation through hydrogen bonding. For this purpose, the study of refractive indices, excess refractive indices, and IR spectra of aqueous solutions of DMF and THF was carried out at room temperature and atmosphere pressure over a wide range of concentrations.

2 EXPERIMENTAL

2.1 Materials

Standard grade tetrahydrofuran (C_4H_8O) (minimum assay 99.9 wt.%) and N,N-dimethylformamide (C_3H_7NO) (purity ~99.9 wt.%) obtained from Reagent Plus, as well as distilled water with pH=7.02 were used in the experiments. For preparation of aqueous solutions of THF and DMF, high-precision analytical scales EP 214C (Ohaus Explorer Pro, Switzerland) with an accuracy of ≤0.0002 g was used. Each aqueous-organic solution of a given composition was prepared separately and was not used in the preparation of solutions with different concentration of compositions.

2.2 Measurement

Refractive indices were measured using a high-sensitivity PAL-RI digital refractometer (ATAGO, Japan). The instrument measures refractive indices in the range of 1.3306–1.5284; the measurement error n is <0.0001.

Fourier transform infrared spectra were recorded on a Perkin Elmer Spectrum Two spectrophotometer with a signal-to-noise ratio of 9300:1 and a resolution of 0.5 cm^{-1} on a $LiTaO_3$ detector. The spectra of pure water, DMF, THF, and their mixtures were recorded in the wavelength range of 4000-400 cm^{-1}.

3 RESULTS AND DISCUSSION

3.1 Refractometric Properties

Precision measurements of the refractive indices (n^E) of a number of pure single-component liquids (water, DMF and THF), as well as aqueous solutions of DMF and

THF in a wide range of component concentrations were carried out at the wavelength of the D_2-line of the sodium atom (λ=589 nm) using a high-sensitivity refractometer. In order to avoid the possible influence of even minor temperature fluctuations both on the density of water and on the density of organic solvent, and therefore on the density of the aqueous organic solutions studied by us, all the experiments below were carried out in a closed thermostatically-controlled laminar flow box at a fixed temperature t=25±0.2 °C and atmospheric pressure.

The stability of the temperature in the measurement compartment was controlled by a built-in thermostat on a Peltier element. The duration of measuring the refractive index of each sample of the solution was no more than 5 seconds. 0.3 ml solution of each sample by three times was measured to ensure measurement accuracy and to avoid equipment error.

The excess refractive indices in terms of the refractive index of pure liquids and their binary solutions of molar composition x were calculated using the equation:

$$n^E = n_{mix} - (x_1 n_1 + x_2 n_2),$$

where x_1, x_2, n_1 and n_2, are the mole fractions and refractive indices of the first and second solvents in their solutions, respectively, and n_{mix} is the refractive index of the solution.

An important optical parameter that can exhibit ionic or molecular behaviour in a mixture is the refractive index, which is primarily determined by the structure of the molecule, wavelength, and temperature.

Table 1. Experimental Mole Fraction, Refractive Index, Excess Refractive Index and Excess Refractive Index for DMF-Water and THF-Water

x, DMF	*n*	n^E	*x,* THF	*n*	n^E
1.000	1.4272	0.0000	1.0000	1.4098	0.0000
0.897	1.4251	0.0077	0.9003	1.4088	0.0067
0.797	1.4239	0.0160	0.8025	1.4075	0.0130
0.702	1.4224	0.0235	0.6970	1.4051	0.0188
0.601	1.4200	0.0307	0.5977	1.4024	0.0237
0.498	1.4167	0.0371	0.4961	1.3990	0.0282
0.398	1.4113	0.0411	0.3972	1.3949	0.0320
0.302	1.4045	0.0435	0.2974	1.3860	0.0296
0.201	1.3904	0.0389	0.2002	1.3707	0.0228
0.099	1.3677	0.0259	0.1043	1.3574	0.0169
0.000	1.3324	0.0000	0.0000	1.3324	0.0000

The refractive index of the mixture depends on chemical rearrangements during mixing of solutions associated with electron polarizability, and the peak of the excess refractive index occurs when the physical properties of solvent-solvent processes change [64]. This can be shown from the calculated values of the excess refractive indices, where the n^E of the aprotic-protic solvent mixtures are higher than that of the protic-protic ones. In the THF-water and DMF-water systems, the refractive index values change monotonically with increasing molarity of aprotic liquids [64]. The refractive indices and calculated excess refractive indices of the THF-water and DMF-water mixtures are shown in Table 1. The refractive indices of the THF-water and DMF-water systems show a positive value along the x-axis (Fig. 1). We obtained deviations from the theoretical line, which indicates specific molecular interactions between various components.

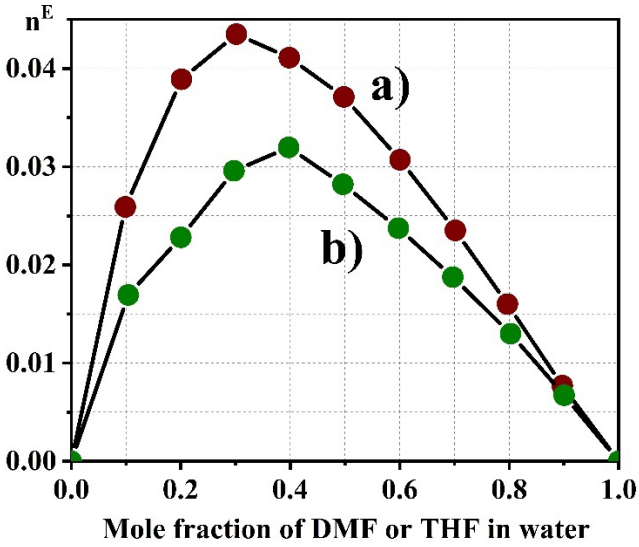

Fig. 1. Excess refractive index for binary solutions of DMF-water (a) and THF-water (b).

Figure 1 shows the excess refractive indices of DMF (a) and THF (b) in water, respectively, with different concentrations. The maximum of excess refractive indices corresponds to 0.3÷0.4 mole fraction of DMF and THF in the water. This is a good agreement with other literature data [63], [66], [68]. These maximum points represent the maximum number of interactions (intermolecular bonds) between DMF and water, as well as THF and water. These intermolecular bonds can be of different types, such as Van der Waals bonds, but they are more likely to be hydrogen bonds [13]. In comparing intermolecular interactions of water solutions, it is shown that the maximum value of the excess refractive indices of DMF-water is higher than that of THF-water. This result indicates that the solvent-solvent interaction of DMF-water is stronger in the same molar ratio of DMF and THF with water. Unlike the THF, the existence of nitrogen in the DMF makes both donor and acceptor bonds in the solution and strengthens bonds between DMF molecules and water [14], [15].

3.2 Infrared Spectra

Vibrational spectroscopy provides detailed and rare information about the intermolecular and intramolecular bonding interactions in liquids. Investigating vibrational frequency, changes in intensity and bandwidth offers valuable insight into the specific type of intermolecular interactions taking place in the liquid state. The infrared spectra of binary solutions of DMF-water and THF-water with a concentration range of 0–1 mole fraction were recorded. Figure 2 shows IR spectra of DMF-water (Fig. 2a) and THF-water (Fig. 2b) in the 3700–3000 cm^{-1} region.

The peak of maximum intensity in the spectra of DMF-water and THF-water is located at around 3400 cm^{-1}. Extremely wide spectra of OH stretching of both DMF-water and THF-water solutions undergo changes in integral intensity, as well as in

the contour shape and the ratio of intensities taken at low frequency to high-frequency field. The absorption band 3352 cm^{-1} of DMF-water shifts to 3500 cm^{-1}, absorption band of THF-water at 3352 cm^{-1} shifts to 3450 cm^{-1} as shown in Fig. 2b. These shifts in the OH stretching region indicate strong hydrogen bonding interactions between DMF and THF, respectively, with water molecules (Fig. 2a). At $X_{DMF} < 0.4$, hydrogen bonds between DMF and water molecules occur rapidly as a result of the disruption of the tetrahedral structure of water or the breaking of hydrogen bonds between water molecules. A similar phenomenon was observed in the DMF-water system by Raman spectroscopy [74]. Results of the exothermic enthalpies of DMF-water solution show at $x \approx 0.33$ mole fraction of DMF, the repulsive interaction between the hydrophobic groups (CH_3) and water drives the formation of larger, longer-lived molecular clusters. This repulsive interaction leads to energy being released, and the hydrogen bonds between DMF and water are stronger than hydrogen bonds between water molecules [74].

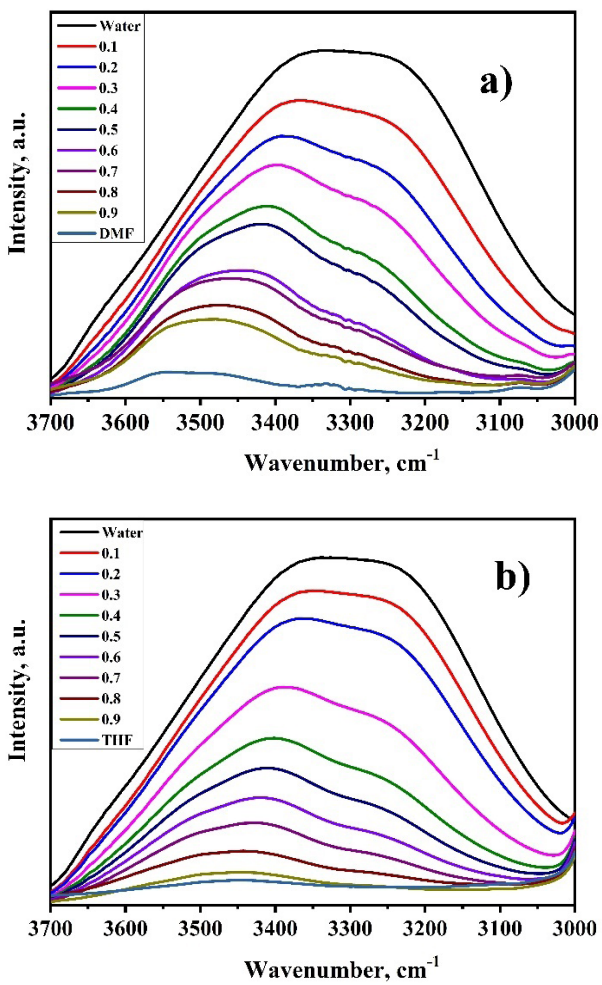

Fig. 2. Absorption bands 3000–3700cm^{-1} of OH-groups in the infrared spectra of DMF-water (a), and THF-water (b) solutions.

According to the measured IR spectra, it was shown that the mixture of water+THF forms complexes of 1:2 composition in the concentration range 0.1<x<0.4. It was shown that the hydration of THF occurred with the participation of weak hydrogen bonds $H_2O\cdots$H-C. It was also demonstrated that, in a narrow concentration range of 0.25–0.4 mole fraction of THF, the excess molar volume has a maximum characterising the formation of a dense structural packing of mixtures accompanied by strong interactions between molecules of both components [67], [69]. Excess molar volumes for the tetrahydrofuran + water system were calculated from experimentally measured densities and correlated using the Redlich-Kister equation [70]. The negative excess molar volume maxima also provide information about the presence of the following factors, such as strong specific interactions between hetero molecules via hydrogen bonds. The highest negative value of the molar volume is observed at a mole fraction of THF ~0.37 [67]. This indicates that the size of self-associated clusters formed by water molecules decreases with an increase in the molar fraction of THF in the concentration range and $0<X_{THF}<0.4$ [69]. The NMR data showed that the rotational motion of water molecules was most restricted at a concentration of $x \approx 0.3$ mole fraction of tetrahydrofuran, suggesting that the hydrogen bonds between water molecules were most immobile at this concentration.

The previous work [75] showed the ratio of absorption intensities at 3240 and 3360 cm^{-1} oscillation frequencies of OH-groups bound by strong and weak H-bonds for IR spectra of water-ethanol solutions. This ratio of absorption intensities by concentration of components allows obtaining information of stronger and quantity of H-bonds in solutions. In this work, we calculated the ratio of absorption intensities at 3246 cm^{-1} and 3352 cm^{-1} which corresponded to strong and weak hydrogen bonding, respectively (Fig. 3).

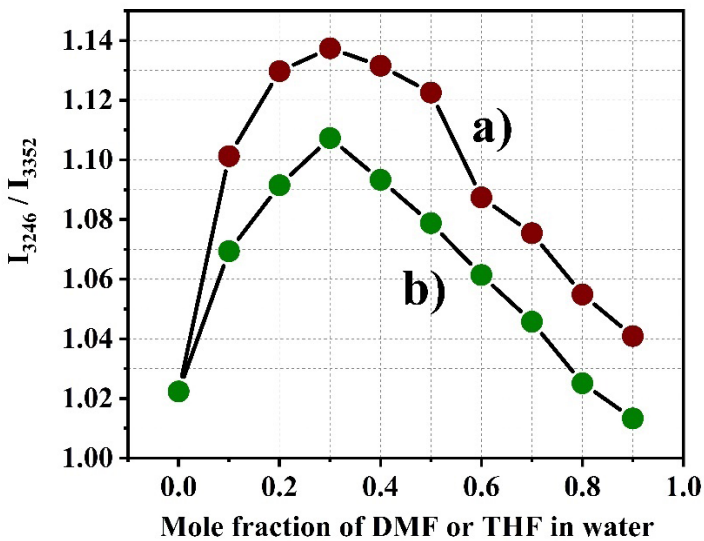

Fig. 3. Ratio of absorbance values taken at wavenumbers 3246 and 3360 cm^{-1} as a function of DMF (a) and THF (b) concentrations in solution.

DMF-water owns a wide maximum peak position, which includes 0.2–0.5 mole concentration of DMF in water, signified 0.3 mole DMF has strongest H-bonding, other concentrations like 0.2 and 0.4 closely make H-bonds in the solution. THF-water showed very sharp maximum of the peak at 0.3 mole fraction of THF in water, which formed 0.3 THF distinguishable strong H-bonds than other concentration. This result shows that hydrogen bond strengthening and significant structural rearrangement occur in the concentration range of $0.3<x<0.4$ mole fraction of DMF and THF. Both graphs show that the ratio passes through a maximum in the dissolved component concentration region of 0.3÷0.4 mole fraction. We interpret these results in terms of hydrogen bond saturation and maximum realization of the number of hydrogen bonds in mixtures within a narrow concentration range of DMF and THF. A comparative analysis of hydrogen bonding shows that water molecules are more strongly bonded to DMF than to THF. This IR analysis is in good agreement with the properties of H-bonds predicted by the refractive index excess. According to the purpose of the work, these two methods of analysis, complementing each other, are advantageous in obtaining quick and accurate information on H-bonds in the structure.

Another calculation for evaluating the characteristics of hydrogen bonds in mixtures was presented in the previous work [75]. Plotting deconvoluted the main symmetric and asymmetric OH stretching bands of Raman spectra, using Gaussian fitting characterised hydrogen bonds in DMF-water solutions [76]. As it is known, the spectral characteristics of hydrogen bonding represent three main spectral components with maxima of vibrations of strongly H-bonded OH-groups (3200 cm^{-1}), weakly H-bonded OH-groups (3400 cm^{-1}) and vibrations of free OH-groups (3650 cm^{-1}) [65]–[67], [73], [74].

To indicate changes in the infrared spectra, we calculated the ratio of optical density values which is the value of the speed of light passing through a sample. The corresponding Gaussian fitting results of pure water are shown in Fig. 2.

Detailed information of the Gaussian fitting to indicate symmetric and asymmetric H-bonding using IR spectrum of the pure water is given in Table 2. In the same way, we fitted all IR spectra DMF-water and THF-water solutions. Results of the detected peak position of symmetric and asymmetric H-bonds of pure water, as well as other mixtures are shown in Table 2.

Table 2. Peak Position of the Symmetric and Asymmetric H-Bonding of OH Group in DMF-Water and THF-Water Mixtures Detected by Gaussian Fitting of IR Spectra

Mole fraction of DMF	Asymmetric OH bonds (weak hydrogen bonds)	Symmetric OH bond (strong hydrogen bonds)
0	3183	3360
0.1	3201	3385
0.2	3241	3411
0.3	3250	3412
0.4	3257	3422
0.5	3258	3428
0.6	3279	3454
0.7	3277	3459
0.8	3282	3469
0.9	3292	3483

Mole fraction of THF	Asymmetric OH bonds (weak hydrogen bonds)	Symmetric OH bond (strong hydrogen bonds)
0	3183	3360
0.1	3227	3397
0.2	3229	3405
0.3	3225	3405
0.4	3246	3409
0.5	3258	3419
0.6	3241	3430
0.7	3268	3431
0.8	3272	3459
0.9	3270	3463

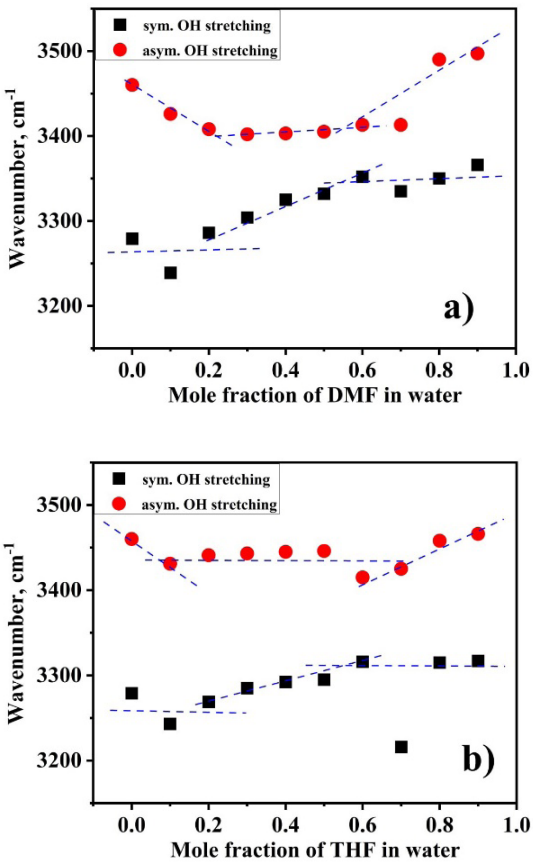

Fig. 4. Infrared intensity peaks of water with different mole fractions of DMF (a) and THF (b).

Figure 4 illustrates the infrared peak intensities of water at different X_{DMF} and X_{THF} in OH stretching vibration mode. Complexes are formed rapidly between water molecules and DMF and water molecules and THF molecules through the hydrogen bonds (Figs. 4a and 4b). At low concentration of DMF, the red shift of the

OH stretching vibration mode may be due to the fact that DMF barely weakens the tetrahedral structure of water [76]. However, very interestingly, at medium concentrations of DMF (0.3–0.5) a linear horizontal position is maintained, which we may consider as DMF replacing water molecules and DMF-water molecules creating a maximal number of hydrogen bonds and balancing with heterostructures of DMF-water and structures of water-water. Nevertheless, the OH stretching vibration mode quickly moves up at $X_{DMF} > 0.5$, which may be due to the fact that as the concentration of DMF increases in DMF-water mixtures, the tetrahedral structure of water is destroyed, resulting in the breaking of hydrogen bonds between water and water.

In the case of THF-water, we observed a clear boundary of changes at 0.3 mole of THF. Unlike the medium concentration effect of DMF on water molecules, THF enters into the water molecule network, which is formed due to hydrogen bonds, and linearly affects the structure of water by increasing its concentration. It can be seen that the critical point of the concentration of THF is 0.3, where the maximum H-bonds occur between molecules of THF and water. By increasing concentration of THF, hydrogen bonds weaken and decrease due to destroying water-water H-bonds, increasing THF-THF structures in the solutions.

4. CONCLUSIONS

By analysing the refractometry data in detail, it was found that structural changes occurred for DMF-water at ~0.3 mole fraction of DMF and THF-water at ~0.4 mole fraction of DMF. The studied two-component mixtures of THF-water and DMF-water belong to the category of solutions, in which not only intramolecular but also intermolecular complexes with H-bonding are formed, leading to compaction of solutions. The latter is confirmed by positive values of the excess refractive indices of all three binary mixtures in the entire range of component concentrations ($0<X<1$).

The established patterns of structural self-organization of binary solutions can be useful both for planning chromatographic experiments using two-component aqueous organic solvents as a mobile phase and for analysing the results obtained.

Thus, a novel approach based on the combined use of refractometry and IR spectroscopy is proposed to study structural changes in DMF-water and THF-water solutions over a concentration range from 0.0 to 1.0 mole fraction of components at room temperature and atmospheric pressure. It is shown that refractometry and IR spectroscopy are not only simple and accessible for studying aqueous solutions of aprotic solvents, but also extremely sensitive for detecting the formation of heteromolecular structures due to hydrogen bonds.

ACKNOWLEDGEMENTS

This study has been financially supported by the Foundation for Basic Research of the Academy of Sciences of Uzbekistan, the Ministry of Innovative Development of the Republic of Uzbekistan (grant No. FZ-202009029314) and Mirai Foundation.

REFERENCES

1. Esmonde-White, K., Lewis, M., & Lewis, I. R. (2022). Direct Measurement of Chocolate Components Using Dispersive Raman Spectroscopy at 1000 nm Excitation. *Applied Spectroscopy, 77* (3), 320–326.
2. Escoriza, M. F., Vanbriesen, J. M., Stewart, S., & Maier, J. (2006). Studying Bacterial Metabolic States Using Raman Spectroscopy. *Applied Spectroscopy, 60* (9), 971–976.
3. Xu, Y., Zhu, D., Song, Y., Zheng, X., & You, X. (2006). Hydrothermal Synthesis and Crystal Structure of the Novel Mixed Mo/V Meta-l-Oxygen Cluster Compound [Co(C2N2H8)(3)](4)[(Mo2Mo14V16O80)-Mo-V-V-VI-O-IV (PO4)(2)]Center Dot 10H(2)O Containing the Two Types of Typical Heteropoly Anions. The Journal of Molecular Structure, *782* (2), 165–170.
4. Sharma, A., Kaur, S., Mahajan C. G., Tripathi, S. K., & Saini, S. S. G. (2007). Fourier Transform Infrared Spectral Study of N, N′-Dimethylformamide-Water-Rhodamine 6G Mixture. Molecular Physics, 105 (1), 117–123.
5. Kanan, P. P., Arivazhagan, G., Sangeetha, T., Karthick, N. K., & Kumbharkhane A. C. (2021). FTIR Studies, DFT Calculations, and Time Domain Reflectometry Studies on TGF-Methanol Binary Solutions. Spectrochimica Acta, *Part A:* Molecular and Biomolecular Spectroscopy, 248, 119289.
6. Dwivedi, A., Baboo, V., & Bajpai. A. (2015). Fukui Function Analysis and Optical, Electronic, and Vibrational Properties of Tetrahydrofuran and Its Derivatives: A Complete Quantum Chemical Study. Journal of Theoretical Chemistry, 345234.
7. Ohashi, K., & Takeshita, H., (2021). Infrared Spectroscopic and Computational Studies of Co (ClO4)2 Dissolved in N, N-Dimethylformamide. Spectrochimica Acta, Part A: Molecular and Biomolecular Spectroscopy, 248, 119289.
8. Chalapathi, V. V., & Ramiah. K. V. (1966). Normal Vibrations of N, N-Dimethylformamide and N, N-Dimethylacetamide. *Proc. lnd. Acad. Sci, 64*, 148.
9. Tomar, D., Rana, B., & Jena. K. C. (2020). The Structure of Water–DMF Binary Mixtures Probed by Linear and Nonlinear Vibrational Spectroscopy. Journal of Chemical Physics, 152 (11), 114707.
10. Xu, Z., Li, H., Wang, C., Pan, H., & Han. S. (2006). The Methyl C–H Blueshift in N, N-Dimethylformamide-Water Mixtures Probed by Two-Dimensional Fourier-Transform Infrared Spectroscopy. Journal of Chemical Physics, 124 (24), 244502.
11. Biliškov, N., & Baranović, G. (2009). Infrared Spectroscopy of Liquid Water–N, N-Dimethylformamide Mixtures. The Journal of Molecular Liquids, 144 (3), 155–162.
12. Martínez-Reina, M., Amado-González, E., & Goméz-Jaramillo, W. (2015). Experimental Study and Modeling of the Refractive Indices in Binary and Ternary Mixtures of Water with Methanol, Ethanol and Propan-1-ol at 293.15 K. *Journal of* Solution Chemistry, *44* (2), 206–222.
13. Gofurov, Sh., Makhmanov, U., Kokhkharov, A., & Ismailova, O. B. (2019). Structural and Optical Characteristics of Aqueous Solutions of Acetic Acid. Applied Spectroscopy, 73 (5), 503–510.
14. Tomikawa, K., Kanno, H., & Kimoto, H. (2004). A Raman Study of Aqueous DMF and DMA Solutions at Low Temperatures. Canadian Journal of Chemistry, 82 (10), 1468–1473.
15. Pansare, K., Singh, S. R., Chakravarthy, V., Gupta, N., Hole, A., Gera, P., … & Krishna. C. M. (2020). EXPRESS: Raman Spectroscopy: An Exploratory Study to Identify Post-Radiation Cell Survival. *Applied Spectroscopy, 74* (5), 000370282090835.
16. Bozorova, D. T., Gofurov, Sh. P., Kokhkharov. A. M., & Ismailova O. B. (2021). Terahertz Spectroscopy of Aqueous Solutions of Acetic Acid. Journal of Applied Spectroscopy, 88 (4), 719–722.

17. Globus, T. R., Woolard, D. L., Khromova, T., Crowe, T. W., Bykhovskaia, M., Gelmont, B. L., … & Samuels, A.C. (2003). *THz-Spectroscopy of Biological Molecules.* Journal of Biological Physics, *29*, 89–100.
18. Ye, P., Meng, Q., Wang, G., Huang, H., Yang, Y., Su, B., & Zhang, C. (2022). Terahertz Spectroscopic Detection of Amino Acid Molecules under Magnetic Field. *Heliyon., 8* (11), 11414.
19. Wei, L., Yu, L., Jiaoqi, H., Guorong, H., Yang, Zh., & Weiling. F. (2018). Application of Terahertz Spectroscopy in Biomolecule Detection. *Frontiers in Laboratory Medicine, 2* (1), 127–133.
20. Lee. Y. S. (2009).*Terahertz Spectroscopy of Atoms and Molecules*. Principles of Terahertz Science and Technology. Springer, Boston, MA.
21. Mathlouthi, M. (1981). X-ray Diffraction Study of the Molecular Association in Aqueous Solutions of d-Fructose, d-Glucose, and Sucrose. *Carbohydrate Research, 91* (2), 113–123.
22. Kruh, R. F., & Standley, C. L. (1962). An X-Ray Diffraction Study of Aqueous Zinc Chloride Solutions. *Inorganic Chemisty, 1* (4), 941–943.
23. Adams, R., Balyuzi, H. H. M., & Burge, R. E. (1977). X-Ray Diffraction Studies of Aqueous Solutions of Urea. *J. Appl. Cryst., 10*, 256–261.
24. Gioacchino, M. Di., Bruni, F., & Ricci, M. A. (2019). N-Methylacetamide Aqueous Solutions: A Neutron Diffraction Study. *J. Phys. Chem. B. 123* (8), 1808–1814.
25. Kameda, Y., & Uemura, O. (1993). Neutron Diffraction Study on the Structure of Highly Concentrated Aqueous LiBr Solutions. *Bulletin of the Chemical Society of Japan, 66* (2), 384–389.
26. Ender, J. E. (1980). Neutron Diffraction, Isotopic Substitution and the Structure of Aqueous Solutions. Phil. Trans R. Soc. London. *B, Biological Sciences, 290*, 553–566.
27. Yamaguchi, T., Yoshida, K., Machida, Sh., & Hattori, T. (2022). Neutron Scattering on an Aqueous Sodium Chloride Solution in the Gigapascal Pressure Range. The Journal of Molecular Liquids, 365 (1), 120181.
28. Soper, A. K., Neilson, G. W., Enderby, J. E., & Howe, R. A. (1977). A Neutron Diffraction Study of Hydration Effects in Aqueous Solutions. Journal of Physics C: Solid State Physics, *10*, 1793.
29. Takahashi, H., Oue, T., & Sakai, M. (2020). Resonance IR Spectroscopy in Aqueous Solution by Combining IR Super-Resolution with TFD-IR Method. *Chemical Physics Letters, 758*, 137942.
30. Rabenstein, D. L., & Fan, S. (1986). Proton Nuclear Magnetic Resonance Spectroscopy of Aqueous Solutions: Complete Elimination of the Water Resonance by Spin-Spin Relaxation. *Analytical Chemistry, 58* (14), 3178–3184.
31. Martin, A., Nicholas, P., & Wasylishen, R. E. (1987). A Nuclear Magnetic Resonance Study of Aqueous Solutions of Several Nitrate Salts. *The Canadian Journal of Chemistry, 65* (5), 951–956.
32. Kokhkharov, A. M., Zakhidov, E. A., Gofurov, Sh. P., Bakhramov, S. A., & Makhmanov, U. K. (2013). Clusterization of Fullerene C70 Molecules in Solutions and Its Influence to Optical and Nonlinear Optical Properties of Solutions. *International Journal of Nanoscience, 12* (4), 1350027.
33. Patel, R. B., Stepanov, V., & Qiu, H. (2016). Dependence of Raman Spectral Intensity on Crystal Size in Organic Nano Energetics. *Applied Spectroscopy, 70* (8), 1339–1345.
34. Plastinin, I. V., Burikov, S. A., Gofurov, Sh. P., Ismailova, O. B., Mirgorod, Y., & Dolenko, T. A. (2020). Features of Self-Organization of Sodium Dodecyl-Sulfate in Water-Ethanol solutions: Theory and Vibrational Spectroscopy. *Journal of Molecular Liquids, 298*, 112053.
35. Cholli, A. L., & Lau, M. L. (1989). Simultaneous Detection of Optical Isomers and the Separation of Overlapping Resonances in a 1H NMR Spectrum of (+/-)-2,2-Dimethyl-1-Phenyl-1-Propanol Using an NMR Shift Reagent. *Applied Spectroscopy, 43* (7), 1168–1172.

36. Ismailova, O. B., Akhmedov, T. Kh., Igamberdiev, Kh. T., Mamatkulov, S. I., Saidov, A. A., Tursunov, S. O., & Khabibullaev, P.K. (2005). Heat-Capacity Anomaly in a Wide Vicinity of the Critical Point of the Triethylamine-Water Phase Transition. *Journal of Engineering Physics and Thermophysics, 78* (5), 1040–1045.
37. Larive, C. K., Jayawickrama, D., & Orfi, L. (1997). Quantitative Analysis of Peptides with NMR Spectroscopy. *Applied Spectroscopy, 51* (10), 1531–1536.
38. Flores-Castañeda, M., & Camacho-Lopez, S. (2023). Si Nanoparticle Decorated Bi2O2CO3 2D Nanocomposite Synthesized by Femtosecond Laser Ablation of Solids in Liquids and Aging. *Optics and Laser Technology, 158,* 108891.
39. Xu, Y., Zhu, D., Song, Y., Zheng, X., & You, X. (2006). Hydrothermal Synthesis and Crystal Structure of the Novel Mixed Mo/V Meta-l-Oxygen Cluster Compound [Co(C2N2H8)(3)](4)[(Mo2Mo14V16O80)-Mo-V-V-VI-O-IV (PO4)(2)]Center Dot 10H(2)O Containing the Two Types of Typical Heteropoly Anions. *The Journal of Molecular Structure, 782* (2), 165–170.
40. Mizuno, K. (2009). Roles of the Ether Oxygen in Hydration of TGF studied by IR, NMR and DFT Calculation Methods. *Journal of Physical Chemistry B, 113* (4), 906–915.
41. Weisenberger, L. A., & Koenig, J. L. (1989). NMR Imaging of Solvent Diffusion in Polymers. *Applied Spectroscopy, 43* (7), 1117–1126.
42. Davies, A. N., & Lampen, P. (1993). JCAMP-DX for NMR. *Applied Spectroscopy, 47* (8), 1093–1099.
43. Fischer, J. W., Merwin, L. H., & Nissan, R. A. (1995). NMR Investigation of the Thermolysis of Citric Acid. *Applied Spectroscopy, 49* (1), 120–126.
44. Larive, C. K., Jayawickrama, D., & Orfi, L. (1997) Quantitative Analysis of Peptides with NMR Spectroscopy. *Applied Spectroscopy, 51* (10), 1531–1536.
45. Shastri, A., Das, A. K., Krishnakumar, S., Singh, P. J., & Raja Sekhar, B. N. (2017). Spectroscopy of N, N-dimethylformamide in the VUV and IR Regions: Experimental and Computational Studies. *Journal of Chemical Physics, 147* (22), 224305.
46. Mao, J. X., Walsh, P., Kroll, P., & Schug, K. A. (2019). Simulation of Vacuum Ultraviolet Absorption Spectra: Paraffin, Isoparaffin, Olefin, Naphthene, and Aromatic Hydrocarbon Class Compounds. *Applied Spectroscopy, 74* (2), 72–80.
47. Cruse, C., Pu, J., & Goodpaster, J. V. (2020). EXPRESS: Identifying Thermal Decomposition Products of Nitrate Ester Explosives Using Gas Chromatography–Vacuum Ultraviolet Spectroscopy: An Experimental and Computational Study. *Applied Spectroscopy, 74* (12), 1486–1495.
48. Heravi, M. M., Ghavidel, M., & Mohammadkhan, L. (2018). Beyond a Solvent: Triple Roles of Dimethylformamide in Organic Chemistry. *RSC Adv., 8* (49), 27832–27862.
49. Muzart, J. (2009). N, N-Dimethylformamide: Much More than a Solvent. *Tetrahedron, 65* (40), 8313–8323.
50. Zhu, Y., Yang, J., Mei, F., Li, X., & Zhao, Ch. 2022). Bio-Based 1,4-Butanediol and Tetrahydrofuran Synthesis: Perspective. *Green Chemistry, 24*, 6450–6466.
51. Angle, S. R., & El-Said, N. A. (2002). Stereoselective Synthesis of Tetrahydrofurans via Formal [3+2]-Cycloaddition of Aldehydes and Allylsilanes. Formal Total Synthesis of the Muscarine Alkaloids (−)-Allomuscarine and (+)-Epimuscarin. *Journal of the American Chemical Society, 124* (14), 3608–3613.
52. Sałdyka, M., Mielke, Z., & Haupa, K. (2018). Structural and Spectroscopic Characterization of DMF Complexes with Nitrogen, Carbon Dioxide, Ammonia and Water. Infrared Matrix Isolation and Theoretical Studies. *Spectrochimica Acta - Part A: Molecular and Biomolecular Spectroscopy, 190*, 423–432.
53. Shastri, A., Das, A. K., Krishnakum, S., Singh, P. J., & Sekhar, B. N. R. (2017). Spectroscopy of N, N-Dimethylformamide in the VUV and IR Regions: Experimental and Computational Studies. The Journal of Chemical Physics, 147, 224305.

54. Liu, B., & Bazan, G. C. (2007). Tetrahydrofuran Activates Fluorescence Resonant Energy Transfer from a Cationic Conjugated Polyelectrolyte to Fluorescein-Labeled DNA in Aqueous Media. *Chemistry: An Asian Journal, 2* (4), 499–504.
55. Nawrocki, P. R., & Sørensen, T. J. (2023). Optical Spectroscopy as a Tool for Studying the Solution Chemistry of Neodymium (iii). *Physical Chemistry Chemical Physics, 25*, 19300–19336.
56. Reszka, K., Kolodziejczyk, P., & Lown, J. W. (1988). Photosensitization by Antitumor Agents. 5. Daunorubicin-Photosensitized Oxidation of NAD (P)H in Aqueous and N, N-Dimethylformamide/Aqueous Solutions – An Electron Paramagnetic Resonance Study. *Free Radical Biology and Medicine, 5* (2), 63–70.
57. Hunold, J., Eisermann, J., Brehm, M., & Hinderberger, D. (2020). Characterization of Aqueous Lower-Polarity Solvation Shells Around Amphiphilic 2,2,6,6-Tetramethylpiperidine-1-oxyl Radicals in Water. *Journal of Physical Chemistry B, 124* (39), 8601–8609.
58. Dembek, M., & Bocian, S. (2020). Pure Water as a Mobile Phase in Liquid Chromatography Techniques. *Trends in Analytical Chemistry, 123*, 115793.
59. Clifford, M. J., & Eastwood, D. (2004). Design of a Novel Passive Solar Tracker. *Solar Energy, 77* (3), 269–280.
60. Sanganal, S. K., Kulkarni, G. B., & Karegoudar, T. B. (2013). Development and Validation of High Perfomance Liquid Chromatographic Analysis of Residual N, N-Dimethylformamide in Spent Medium after Biodegradation by Paracoccus denitrificans SD1. *ISRN Chromatography 2013*, 1–6.
61. Góra, R., Hutta, M., & Rohárik, P. (2012). Characterization and Analysis of Soil Humic Acids by Off-Line Combination of Wide-Pore Octadecylsilica Column Reverse Phase High Performance Liquid Chromatography with Narrow Bore Column Size-Exclusion Chromatography and Fluorescence Detection. *Journal of Chromatography A, 1220*, 44–49.
62. Aliaj, F., Bytyqi-Damoni, A., & Syla, N. (2016). Density and Refractive Index Study of the Ternary System Benzene-Ethanol-Hexane. *AIP Conference Proceedings, 1722*, 290015.
63. Moosavi, M., & Rostami, A. A. (2016). Densities, Viscosities, Refractive Indices, and Excess Properties of Aqueous 1,2-Etanediol, 1,3-Propanediol, 1,4-Butanediol, and 1,5-Pentanediol Binary Mixtures. *Journal of Chemical & Engineering Data, 62* (1), 156–168.
64. El-Dossoki, F. I. (2007). Refractive Index and Density Measurements for Selected Binary Protic-Protic, Aprotic-Aprotic, and Aprotic-Protic Systems at Temperatures from 298.15 K to 308.15 K. *JCCS, 54* (5), 1129–1137.
65. Mohammadi, L., & Omrani, A. (2017). Density, Refractive Index, and Excess Properties of Sulfolane and Alkanediols Binary Mixtures at Different Temperatures. *Journal of Thermal Analysis and Calorimetry, 131* (3).
66. Komudzińska, M., Tyczyńska, M., Jóźwiak, M., Burakowski, A., & Gliński, J. (2020). Volumetric, Acoustic and Thermal Properties of Aqueous N, N-Dimethylformamide System. Effect of Temperature and Composition. *Journal of Molecular Liquids, 300*, 112321.
67. Nayak, J. N., Aralaguppi, M. I., Kumar Naidu, B. V., & Aminabhavi, T. M. (2004). Thermodynamic Properties of Water + Tetrahydrofuran and Water + 1,4-Dioxane Mixtures at (303.15, 313.15, and 323.15) K. *Journal of Chemical & Engineering Data, 49* (3), 468–474.
68. Razzokov, D., Ismailova, O. B., Mamatkulov, Sh. I., Trunilina, O. V., & Kokhkharov, A. M. (2014). Heteromolecular Structures in Aqueous Solutions of Dimethylformamide and Tetrahydrofuran, According to Molecular Dynamics Data. *Russian Journal of Physical Chemistry A, 88*, 1500–1506.
69. Katayama, M., & Ozutsumi, K. (2008). The Number of Water-Water Hydrogen Bonds in Water-Tetrahydrofuran and Water-Acetone Binary Mixtures Determined by Means of X-Ray Scattering. *Journal of Solution Chemistry, 37* (6), 841–856.

70. Jones, G., & Talley, S. K. (1933). The Viscosity of Aqueous Solutions as a Function of the Concentration. *Journal of the American Chemical Society, 55* (2), 624–642.
71. Sharma, A., Kaur, S., Mahajan, C. G., Tripathi, S. K., & Saini, S. S. G. (2007). Fourier Transform Infrared Spectral Study of N, N′-Dimethylformamide-Water-Rhodamine 6G Mixture. *Molecular Physics, 105* (1), 117–123.
72. Tomikawa, K., Kanno, H., & Kimoto, H. (2004). A Raman Study of Aqueous DMF and DMA Solutions at Low Temperatures. *Canadian Journal of Chemistry, 82* (10), 1468–1473.
73. Gogolinskaya, T. A., Patsaeva, S. V., & Fadeev, V. V. (1986). On the Regularities of Change of the 3100–3700 $см^{-1}$ Band of Water Raman Scattering in Salt Aqueous Solutions. *Doklady Akademii Nauk, 290* (5), 1099–1103.
74. Cilense, M., Benedetti, A. V., & Vollet, D. R. (1983). Thermodynamic Properties of Liquid Mixtures. II. Dimethylformamide-Water. *Thermochima Acta, 63* (2), 151–156.
75. Burikov, S., Dolenko, T., Patsaeva, S., Starokurov, Y., & Yuzhakov, V. (2010). Raman and IR Spectroscopy Research on Hydrogen Bonding in Water-Ethanol Systems. *Molecular Physics, 108* (18), 2427–2436.
76. Yang, B., Lang, H., Liu, Z., Wang, S., Men, Z., & Sun, C. (2021). Three Stages of Hydrogen Bonding Network in DMF-Water Binary Solution. *Journal of Molecular Liquids, 324*, 114996.

sciendo

LATVIAN JOURNAL OF PHYSICS
AND TECHNICAL SCIENCES
2025, N 4

DOI: 10.2478/lpts-2025-0027

TRANSPORT POVERTY: AN URGENT ISSUE IN THE FUTURE OF THE EU CLIMATE AND ENERGY POLICY

G. Valdmanis[1], L. Zemite[1]*, D. Kronkalns[1], L. Jansons[2]

[1]Riga Technical University,
Faculty of Computer Science,
Information Technology and Energy,
12-1 Azenes Str., Riga, LV-1048, LATVIA
[2]Riga Technical University,
Faculty of Engineering Economics and Management,
6 Kalnciema Str., Riga, LV-1048, LATVIA
*e-mail: laila.zemite@rtu.lv

Transport poverty, defined as limited access to affordable, safe, and efficient mobility, is an emerging policy concern with growing relevance to energy, climate, and social equity agendas. While energy poverty is already recognised as a critical challenge in sustainable development, the interlinkages between energy and transport poverty remain insufficiently explored. This paper examines the structural relationship between both forms of poverty, particularly focusing on the role of energy costs in limiting mobility options for vulnerable populations. We argue that transport poverty should be considered a dimension of energy poverty, especially taking into account rising fuel prices, declining access to public transport, and uneven infrastructure development. Using a qualitative policy review combined with a statistical analysis of long-term mobility trends and household expenditure data in Latvia, we identify key patterns of transport exclusion and their overlap with energy vulnerability. The results show a strong correlation between energy cost inflation and reduced mobility, particularly among low-income and rural households, with declining use of public transport further reinforcing structural inequalities. The study also explores future risks and opportunities, including the growing role of electrification, synthetic fuels, and renewable energy in reshaping the transport landscape. Policy implications are discussed, focusing on decentralised, locally adapted solutions aimed at mitigating transport poverty and enhancing inclusive mobility in the context of broader decarbonisation goals.

Keywords: *Energy poverty, mobility inequality, public transport access, sustainable mobility, transport poverty.*

1. INTRODUCTION

Transport poverty, according to policy planners and researchers, manifests itself in limited access to accessible, affordable, safe, and efficient transport, which affects people's ability to participate in public life, access education, healthcare, work, and other basic needs [1]. Transport poverty is often fundamentally linked to social and economic inequalities, as access to transport is an essential prerequisite for ensuring an individual's mobility in the labour market, providing access to critical services that affect quality of life, preventing threats to an individual's quality of life in cases where the need to use transport services is linked to an individual's state of health, and reducing the risks of social exclusion for such groups in society as families with minor children, persons with disabilities, as well as elderly persons. As outlined by policymakers and researchers [2], transport poverty is not merely a logistical or infrastructural challenge, but a socio-economic phenomenon closely tied to systemic inequalities. Individuals experiencing transport poverty often face a compounding disadvantage, as the lack of mobility can reinforce or exacerbate existing vulnerabilities, such as unemployment, poor health, and educational underachievement. Transport is not only a means of movement but also a key enabler of inclusion and opportunity within modern society. The negative consequences of transport poverty disproportionately affect specific social groups, including low-income households, families with young children, people with disabilities, and elderly individuals. These populations are often less mobile, more dependent on public transport, and more vulnerable to increases in fuel prices, service cuts, or the absence of suitable transport options. In many rural and peri-urban regions, spatial isolation further compounds transport exclusion, creating "mobility deserts" where access to even basic services is severely constrained [3].

In such contexts, mobility becomes a determinant of social inclusion or exclusion. The inability to travel can lead to missed employment opportunities, delayed medical treatment, interrupted education, and deteriorating social networks. As a result, transport poverty contributes directly to broader patterns of deprivation, economic immobility, and geographic inequality. Furthermore, there is growing recognition of the intersection between transport poverty and energy poverty, particularly in regions where private vehicles are the predominant mode of mobility. The rising costs of automotive fuels and vehicle maintenance disproportionately impact economically disadvantaged households, forcing them either to allocate a significant share of income to transport or to reduce travel altogether, thus falling deeper into a cycle of exclusion and constrained opportunity [4], [5]. Addressing transport poverty, therefore, requires a multi-sectoral approach that includes not only transport infrastructure planning and social policy but also energy pricing strategies, spatial planning, and environmental sustainability. Without such integrated action, the structural barriers limiting mobility will continue reinforcing existing inequalities and hindering progress toward equitable and resilient societies.

Recent studies highlight the growing need to examine transport poverty in conjunction with energy poverty, acknowledging that both phenomena often affect the

same vulnerable social groups and exhibit overlapping structural drivers. Conceptually, this intersection is underpinned by three main factors: the mutual influence of energy prices and transport costs; shared socio-economic determinants in affected populations; and the feedback effects of energy poverty mitigation strategies on mobility and transport affordability. A critical link arises through the cost structure of mobility, which is strongly dependent on global energy markets. An analysis of the transport services sector reveals that fuel price volatility, particularly crude oil and refined automotive fuel, remains a dominant factor influencing transport affordability. Buljan and Badovinac (2023) demonstrated that the 2021–2022 energy shock led to significant increases in transport service prices across EU countries, with the highest impacts observed in states with weak modal diversification and high fossil fuel dependence [6]. Latvia, as a net energy importer and with limited low-carbon public transport coverage in rural areas, is particularly exposed to such shocks. Although the correlation between crude oil and other energy prices, such as natural gas and electricity, has declined in the past decade, it remains statistically significant and policy-relevant. Luo and Ye (2024) confirm that electricity prices, while decoupling from oil in many markets, still exhibit time-varying and asymmetric responsiveness to oil price fluctuations, particularly during crisis periods [7].

This coupling implies that rising household energy burdens often translate into increased transport poverty risks, especially for car-dependent and off-grid communities. The inflationary pressures on transport fuel prices directly affect low-income groups' mobility, particularly in Latvia's peripheral municipalities, where alternative transport modes are limited. Furthermore, Savickis et al. (2020) highlight the importance of linking natural gas and biomethane strategies in transport with energy affordability and accessibility goals [5]. Looking ahead, structural changes in both the energy and transport sectors are likely to intensify this interconnection. On the one hand, the electrification of mobility is accelerating across the European Union, supported by policy incentives and falling battery prices. On the other hand, synthetic fuels, including hydrogen and its derivatives, are gaining technological maturity and are expected to complement electric mobility, particularly in heavy-duty, long-haul, and aviation sectors [8]. However, these transitions carry risks of new exclusion mechanisms. If the deployment of electric mobility and hydrogen infrastructure prioritises urban, high-income, or early-adopter populations, the affordability gap may widen for others. In this context, the cost of electricity as a transport energy vector becomes increasingly relevant. As Luo and Ye (2024) [7] point out, electricity price fluctuations – driven by geopolitical, regulatory, and environmental factors – can now have more direct implications for transport poverty than in previous decades. Transport and energy poverty should be treated not as isolated policy concerns, but as interlinked components of a broader socio-technical transition. Understanding their synergies and feedback loops is essential for designing just and effective decarbonisation strategies.

Transport poverty is a growing concern across the European Union, particularly as decarbonisation policies, rising energy prices, and spatial inequalities continue to affect mobility access for vulnerable groups. Although the concept has not yet been uniformly defined across all EU Member States, a growing body of litera-

ture and policy studies acknowledges its multidimensional nature – encompassing affordability, accessibility, and availability of transport services – and its intersection with social exclusion and regional disparity. According to a 2022 European Parliamentary Research Service report, transport poverty affects between 10 % and 25 % of the EU population, depending on how it is measured and defined [9]. Vulnerable populations – including low-income households, people with disabilities, older people, and residents of rural or peri-urban areas – are particularly exposed due to their limited access to affordable and efficient transport services. In France, transport poverty became a central issue during the 2018–2019 "Gilets Jaunes" (Yellow Vests) protests, which were initially triggered by a proposed fuel tax increase. Many low- and middle-income households living in peri-urban and rural areas argued that rising fuel costs disproportionately burdened them due to their dependence on private vehicles and the lack of viable public transport alternatives. The protests exposed the gap between national climate policies and local transport realities, leading to new discussions on mobility justice and equitable green transitions [10]. Although no longer part of the EU, the UK remains an important reference for transport poverty research.

The Joseph Rowntree Foundation found that around 1.5 million people in the UK were at high risk of transport poverty in 2020, with rural and suburban areas disproportionately affected [2]. In response, UK policymakers have explored targeted fare subsidies and mobility-as-a-service models, though challenges in coverage and affordability persist. In Central and Eastern Europe, countries like Hungary and Bulgaria exhibit high levels of transport poverty, particularly in rural regions where public transport systems have deteriorated post-transition. A 2023 review by the European Commission highlighted that in Bulgaria, nearly 40 % of rural residents reported difficulty accessing basic services due to transport constraints. In Hungary, the consolidation of regional bus routes has led to service gaps that significantly hinder access to employment and education for low-income and elderly populations [11]. Italy faces transport poverty challenges primarily in southern regions such as Calabria and Sicily, where low public transport density and high vehicle ownership costs create barriers to mobility. According to the Italian National Institute of Statistics, households in the lowest income quintile spend up to 15 % of their income on transport, well above the 10 % threshold often used to define affordability limits [12]. Germany has made significant efforts to address transport affordability through its 9-Euro Ticket pilot scheme in 2022, which allowed unlimited travel using local and regional transport for EUR 9/month. The programme was widely praised for increasing mobility among low-income users and reducing car usage, though long-term funding and structural integration remain unresolved. Early evaluations suggest that affordability-focused measures can directly reduce transport poverty risks [13]. Across the EU, transport poverty is shaped by a combination of rising fuel prices, inadequate public transport infrastructure, and spatial inequalities in housing and services. While high-income countries face affordability challenges and modal mismatches in urban-suburban transitions, lower-income Member States are disproportionately affected by structural underinvestment and accessibility deficits. These dynamics underline the need

for context-sensitive, place-based policies that combine transport, energy, and social objectives.

Transport poverty in Latvia is an emerging but under-explored issue that has become increasingly relevant considering recent socio-economic developments and energy market shocks. Despite its growing importance, it remains largely absent from national strategic planning documents and public discourse. Nonetheless, structural evidence suggests that transport poverty poses a significant barrier to inclusive mobility, particularly for rural, low-income, and carless households. Latvia's demographic and territorial structure, characterised by dispersed rural settlements, population ageing, and regional depopulation, exacerbates the vulnerability of specific groups to transport exclusion.

Many inhabitants of smaller towns and peripheral regions lack reliable and affordable access to public transport and are thus heavily reliant on private vehicles. However, Eurostat data show that nearly half of Latvian households do not own a car, one of the highest rates in the European Union, especially among low-income households [14]. The long-term decline of Latvia's public transport sector has further deepened the accessibility gap. Between 1990 and 2024, passenger turnover in railway transport decreased more than sevenfold – from 144.5 million to 19.7 million passengers annually – while bus transport usage fell from approximately 500 million to 100 million passengers per year, reflecting a fivefold reduction [15]. This erosion of service availability and frequency, especially in rural areas, has not been matched by improvements in alternative modes such as shared mobility, cycling infrastructure, or integrated multimodal systems. For residents without private transport, especially in low-density and ageing municipalities, this decline has resulted in tangible reductions in mobility. The consequences are wide-ranging, including reduced access to employment, education, healthcare, and public services. Such constraints intensify social exclusion and reinforce territorial disparities, as observed in other Eastern European contexts facing similar transport-related challenges [16]. Further compounding the problem are high and volatile fuel costs.

According to the Latvian Energy Agency, household transport expenditures have risen disproportionately compared to income levels over the last decade, especially during the 2021–2022 energy crisis. This aligns with EU-wide analyses showing that energy price shocks directly increase transport poverty risks in countries with high dependence on fossil fuels and limited modal alternatives [6]. Moreover, studies have shown that low-income Latvian households often lack the financial means to maintain or replace older vehicles with newer, more fuel-efficient models, resulting in higher ongoing operating costs and reduced reliability [17]. This creates a mobility trap, wherein economically vulnerable individuals are forced to use outdated, inefficient, and ultimately more expensive means of transport. Given these conditions, Latvia faces a growing risk of institutionalising transport poverty as a structural form of exclusion. Without targeted policy interventions that combine public transport revitalisation, spatial planning reform, and affordability measures, vulnerable populations may become increasingly disconnected from opportunities necessary for social and economic resilience.

The goal of this study is to examine the structural interlinkages between transport poverty and energy poverty in the European context, with a specific focus

on Latvia, to assess how climate, energy, and mobility policy reforms affect socio-economically vulnerable populations. To achieve this goal, the study pursues the following specific objectives:

- to define and contextualise transport poverty within broader frameworks of energy poverty, mobility inequality, and social exclusion in EU policy and academic literature;
- to assess the long-term decline of public transport use in Latvia, using historical data to illustrate structural accessibility deficits and regional disparities;
- to analyse the impact of rising energy and transport costs on household expenditure patterns, with a focus on vulnerable groups (low-income, rural, elderly, carless);
- to identify and evaluate policy instruments and localised solutions that can mitigate transport poverty in the context of energy transition and decarbonisation, particularly for under-served areas;
- to propose a conceptual framework linking transport and energy poverty as mutually reinforcing socio-economic constraints, supporting the case for integrated, multi-sectoral policy interventions.

2. METHODOLOGY

This study applies a mixed-methods approach combining policy analysis and secondary quantitative data evaluation to investigate the interrelationship between transport poverty and energy poverty, with a primary focus on Latvia and comparative insights across the selected EU Member States.

A structured qualitative review of key policy documents has been conducted to assess the treatment of transport poverty within national and EU-level policy frameworks. The analysis has covered:

- Latvian strategic documents, including the *National Energy and Climate Plan 2021–2030*, *Sustainable Development Strategy 2030*, and *Transport Development Guidelines*;
- European Commission strategies on decarbonisation and mobility, including *Fit for 55*, *Sustainable and Smart Mobility Strategy*, and related legislative instruments;
- reports by the European Parliamentary Research Service (2022) and other policy think tanks;
- academic studies on the socio-political dimensions of mobility exclusion [2], [10].

This review has focused on identifying policy instruments directly or indirectly affecting vulnerable transport users, including tax regimes, fare subsidies, fuel pricing, infrastructure planning, and social support integration. To support empirical insights, the study has utilised secondary data from authoritative sources:

- Eurostat: for passenger transport by mode, car ownership, fuel price indices, and regional statistics;
- the Central Statistical Bureau of Latvia (CSB): including historical rail and bus passenger turnover (1990–2024), household transport spending, and mobility indicators;
- the Latvian Energy Agency: data on transport energy consumption trends and energy price impacts;

- the OECD and European Commission reports: covering mobility disparities, income quintiles, and affordability metrics.

Data have been analysed to observe trends in:
- declining public transport use in Latvia;
- changes in private vehicle reliance by income group;
- household exposure to transport and energy expenditure burdens;
- car ownership disparities as a proxy for mobility inequality.

A comparative indicator table has been developed to benchmark Latvia against five other EU countries (France, Germany, Italy, Bulgaria, and Hungary). The figure includes:
- car ownership rates per 1000 persons;
- urban household access to public transport;
- estimated percentage of households in transport poverty;
- fuel expenditure as a share of household budgets.

The indicators have been selected based on availability, relevance, and their application in prior EU-wide assessments [6], [9].

A conceptual framework has been constructed to illustrate the dynamic interplay between transport poverty and energy poverty, emphasising shared cost traps and the role of spatial inequality. This model integrates statistical patterns with policy findings to highlight systemic feedback loops and exclusion risks. The framework supports the discussion on transport justice and policy intervention strategies presented in the current article.

3. COMPARATIVE ASSESSMENT OF TRANSPORT POVERTY AND ITS INTERSECTIONS WITH ENERGY POVERTY

Understanding the dynamics of transport poverty in the European Union requires not only a definition rooted in socio-economic exclusion and accessibility constraints, but also a comparative examination of how this phenomenon manifests across different Member States. As highlighted by the European Parliament [1], transport poverty is a multi-dimensional issue that arises when individuals or households are unable to access necessary transport services due to financial, infrastructural, or spatial constraints. Importantly, transport poverty shares numerous characteristics with energy poverty, most notably, the disproportionate burden on low-income and rural populations, and the link to structural underinvestment in critical public services [9], [18], [19]. To illustrate the national differences in the manifestation of transport poverty, Fig. 1 presents a comparison across six EU countries: Latvia, France, Germany, Italy, Hungary, and Bulgaria, using three key indicators: car ownership per 1000 inhabitants, public transport access for urban households, and the estimated share of households at risk of transport poverty.

As shown in Fig. 1, significant disparities exist between Western and Eastern EU Member States. France and Germany exhibit high car ownership (above 600 vehicles per 1,000 inhabitants) and near-universal public transport access among urban households. These factors correlate with comparatively lower estimated transport poverty rates (below 10 %) [9], [20].

In contrast, Latvia, Hungary, and Bulgaria present a much more precarious situation. Latvia, for instance, shows a car ownership rate of approximately 360 cars per 1000 inhabitants and public transport accessibility for around 65 % of urban households. In contrast, approximately 22 % of households are at risk of transport poverty. This aligns with Eurostat data on income quintiles and regional accessibility, further confirming a pattern of compounded socio-spatial disadvantage [8].

The disparities in Fig. 1 underscore the contextual nature of transport poverty. In wealthier Western European nations, transport poverty mitigation may revolve around enhancing affordability, reducing emissions, and promoting modal shift through multimodal integration and smart infrastructure. Conversely, for Eastern European Member States, including Latvia, the core challenges relate to deteriorating infrastructure, sparse public transport coverage, ageing vehicle fleets, and institutional undercapacity for long-term investment planning [17], [21]. However, transport poverty cannot be viewed in isolation. There is growing recognition within the academic literature that it is structurally and economically entangled with energy poverty. Figure 2 illustrates this interconnectedness by outlining key drivers of each poverty form, while also identifying overlapping vulnerabilities.

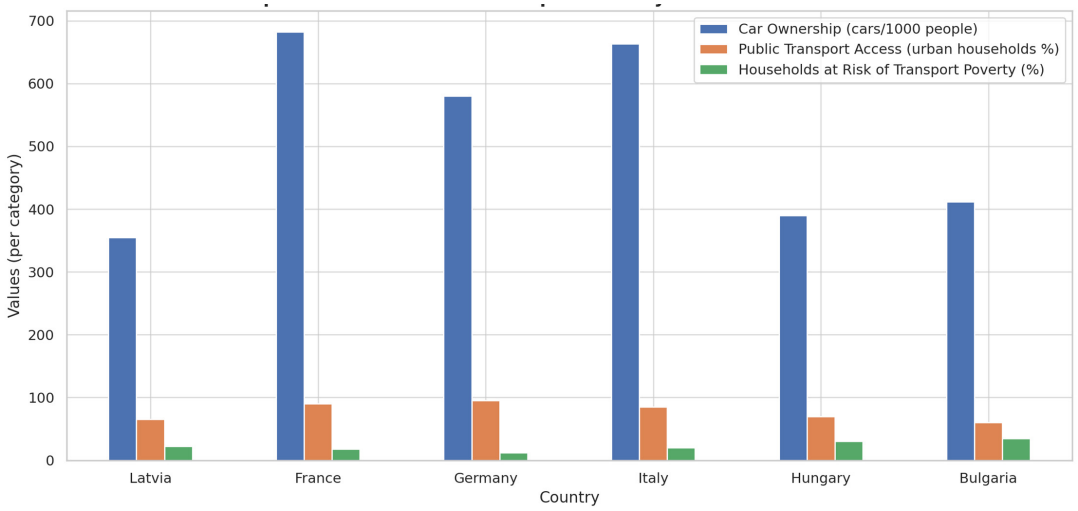

Fig. 1. Comparative indicators of transport poverty in the selected EU countries.

Figure 2 demonstrates that while energy poverty typically stems from high fuel prices, low incomes, and poor household energy efficiency, transport poverty arises due to limited transport infrastructure, high car dependency, as well as vehicle ownership and maintenance costs. Critically, shared vulnerabilities include rural isolation, income inequality, and policy neglect. These overlapping constraints form a reinforcing cycle that entraps households in multidimensional deprivation, as discussed by Kroics et al. [21] and Jasevics et al. [18].

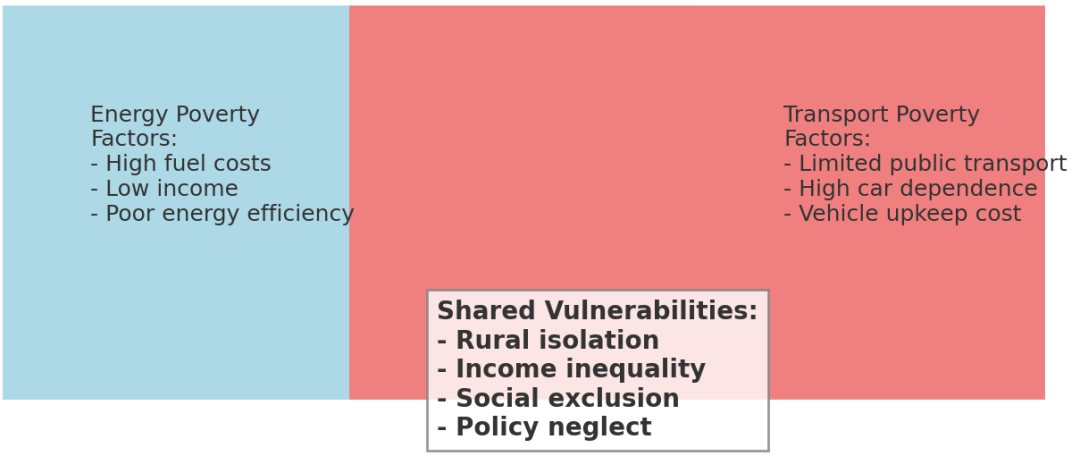

Fig. 2. Shared vulnerabilities between energy and transport poverty.

In Latvia, these interconnections are particularly evident. Recent studies have highlighted that nearly 30 % of rural households have trouble affording transportation to essential services such as healthcare and employment, exacerbated by the country's low-density settlement structure and declining public transport provision [5], [22]. The Central Statistical Bureau of Latvia (2024) reports a dramatic decline in public transport usage over the past three decades – rail passenger turnover dropped from 144.5 million in 1990 to 19.7 million in 2024, while bus passenger numbers fell from 500 million to 100 million in the same period. These declines suggest not only changing travel behaviour but also the erosion of viable mobility options for large segments of the population. This trend reflects a broader structural shift in the EU cohesion policy, where market-oriented transport liberalisation and reduced investment in rural infrastructure have failed to align with decarbonization objectives and the social inclusion goals of the European Green Deal [1], [19], [23]. In effect, households caught in the intersection of energy and transport poverty are increasingly excluded from both the benefits of the energy transition and the mobility required to participate in economic and social life.

To address this issue, research increasingly calls for integrated policy approaches that bridge energy and mobility planning. For example, the deployment of shared transport systems and electrified last-mile services, particularly in rural and peri-urban areas, has been identified as a promising mitigation pathway [8], [24]. Furthermore, hydrogen mobility solutions and improved access to electric vehicle charging infrastructure can provide long-term synergies, as explored by Backurs et al. [24] and Gorobetz et al. [22].

Comparative evidence reveals significant intra-EU disparities in transport poverty, which are strongly influenced by infrastructural legacy, regional economic structures, and governance capacity. The Latvian case illustrates how transport poverty can persist despite moderate car ownership levels, especially when public transport systems are under-resourced and energy costs are volatile. Addressing this challenge requires not only financial instruments but also planning paradigms that recognise the intertwined nature of energy and transport exclusion.

4. ENERGY COST TRAP IN THE TRANSPORT SECTOR

One of the most widely used indicators of transport poverty is the share of transport and mobility-related expenditures in a household's overall budget. This approach mirrors how energy poverty is typically measured, where households spending more than a set threshold – commonly 10 % – on energy costs are considered at risk. In the transport context, excessive expenditure burdens are particularly acute among low-income and rural households that lack access to efficient public transport or rely on outdated, fuel-inefficient vehicles. However, as with energy poverty, this cost-based metric has limitations. Households burdened by high mobility costs may respond not by spending more, but by reducing or forgoing travel altogether, making transport poverty a latent and underreported phenomenon. This coping strategy, while economically necessary, can lead to substantial negative impacts on well-being, including diminished access to employment, healthcare, education, and social participation [2], [3], [24]. In this way, transport poverty operates as a hidden driver of social exclusion and reinforces existing patterns of socioeconomic disadvantage. The interlinkage with energy poverty further compounds the problem. In both cases, households may face systemic cost traps. For example, energy-poor households often lack the financial means to invest in home insulation or renewable energy technologies – expenditures that could reduce long-term costs. Similarly, transport-poor households may be unable to afford timely vehicle maintenance or replacement, leaving them reliant on older vehicles with higher fuel consumption, greater repair needs, and more frequent breakdowns [2], [17]. These conditions create a feedback loop wherein the inability to reduce costs through efficiency-enhancing investments perpetuates poverty and deepens vulnerability. Moreover, transport poverty is increasingly influenced by energy market dynamics.

A study by Buljan and Badovinac (2023) [6] found that the 2021–2022 energy price shock led to measurable increases in consumer transport costs across all EU countries, with disproportionate impacts in Central and Eastern Europe. Households in these regions already allocate a higher share of their income to transport and energy, magnifying their exposure to volatility. Additionally, Luo and Ye (2024) demonstrated that electricity prices remain partially coupled with global oil markets, especially during periods of crisis, and may affect future transport affordability as electric vehicle (EV) adoption grows. As electricity becomes a more prominent energy carrier in the transport sector, through EVs and synthetic fuels like hydrogen, the affordability and predictability of electricity pricing will increasingly shape transport poverty dynamics [7].

This energy cost trap also imposes opportunity costs. Households forced to reduce mobility due to fuel unaffordability may face reduced income potential (due to job inaccessibility), missed medical appointments, and educational disruptions – all of which have long-term implications for social mobility and public health [16], [23]. Taken together, these findings suggest that addressing transport poverty requires integrated policy solutions. These should consider not only the direct costs of transport, but also the broader structural barriers that prevent households from adopting more efficient, lower-cost mobil-

ity solutions, such as targeted investment in public transport, support for cleaner and more affordable vehicle technologies, and mechanisms to shield vulnerable groups from fuel and electricity price shocks.

5. CRUCIAL ROLE FOR PUBLIC TRANSPORT

Policymakers now recognise that the rise in transport and mobility costs disproportionately burdens lower-income and socially vulnerable households, primarily because these groups are often limited to affordable housing located on the periphery, far from public transport networks and lacking safe pedestrian or cycling routes. This spatial segregation forces reliance on costly private transport or severely constrained mobility, creating a socio-economic "infrastructure trap" closely tied to housing location, accessibility, and affordability [1], [9]. The absence of nearby public transport not only restricts daily mobility but also undermines access to essential services, employment, education, healthcare, and social networks, deepening economic and social exclusion [2], [16]. Moreover, transport-poor households may find it difficult to sell or relocate their property, as a lack of connectivity lowers real estate values and liquidity, reinforcing the poverty cycle. When public transport is scarce or inefficient, users often abandon it in favour of more expensive individual solutions or reduce travel altogether. This behaviour reduces system ridership, increases unit operating costs, and often results in higher fares, further alienating vulnerable users [3]. Such feedback loops, where reduced demand raises costs, which further depresses demand, can institutionalise transport poverty over time.

In the context of energy transition, the implications are twofold. Initiatives such as low-emission zones, electrification, and carbon pricing can inadvertently penalise transport-poor households who own older, less efficient vehicles or lack access to electric alternatives [4], [6], [22]. To avoid deepening inequalities, these policies must be paired with equitable public transport improvements and subsidy adjustments that prioritise underserved regions. Latvia exemplifies these challenges and possible responses. Rail passenger turnover declined from 144.5 million in 1990 to just 19.7 million in 2024, while bus usage decreased from 500 million to 100 million passengers annually during the same period [15]. Addressing this issue requires redesigning transport systems to become more compact and demand responsive.

Pilot schemes involving smaller vehicles on-demand, e-bike and car-sharing integration, and re-evaluation of redundant or overlapping routes have shown promise in improving access and cost-efficiency [17], [24]. Effective solutions necessitate close coordination between transport and social policy domains at the local level. Municipalities need granular data on household mobility needs and socio-economic profiles to design fare subsidies, multimodal services, and spatial plans that integrate housing with accessible transport infrastructures. This tailored approach echoes findings from Latvian research on hydrogen and rural mobility innovations, which stress the importance of local engagement and technology-driven solutions [4], [23]. Public transport must be viewed not just as a service, but as a social equity enabler. Without inclusive design and proactive support, mobility systems

risk reinforcing spatial inequality and deepening poverty. Properly planned and subsidised public transport, responsive to local conditions and vulnerable groups, is essential for equitable mobility and sustainable development.

6. LOCALISED SOLUTIONS AS A KEY TO EQUITABLE TRANSPORT POLICY

Through major reforms in the areas of climate and energy – particularly those aiming to reduce emissions and fossil fuel dependency – European governments have introduced policy instruments that, although environmentally motivated, can inadvertently exacerbate transport poverty among vulnerable populations. Fiscal measures such as fuel taxation, vehicle levies, and carbon pricing mechanisms disproportionately affect low-income and peripheral-area households that often rely on older, less efficient vehicles and have limited access to public transit alternatives [1].

In the Latvian context, statistical evidence reflects a severe long-term decline in public transport usage. According to the Central Statistical Bureau, rail passenger turnover decreased from 144.5 million passengers in 1990 to just 19.7 million in 2024, while bus and coach services declined from approximately 500 million to 100 million passengers annually during the same period. This five-to-sevenfold reduction indicates a profound structural shift in travel habits, likely driven by urban sprawl, car-centric development, and public transport disinvestment. These data confirm that restoring public transport networks to pre-1990 service levels – especially at comparable costs – is no longer feasible, necessitating a paradigmatic shift in mobility planning. As illustrated in Fig. 3, there is growing consensus that the future of public transport must be reoriented toward "compact" systems tailored to the needs of specific groups, particularly those most affected by transport poverty. These include low-income families, older adults, persons with disabilities, and rural residents. In this context, the effectiveness of national-level, one-size-fits-all solutions is increasingly questioned. The complexity and local specificity of transport poverty demand an adaptive approach that reflects diverse regional contexts. National policies, especially those in taxation, energy transition, or emission control, often overlook the lived realities of peripheral and low-income populations. As a result, traditional policy instruments have begun to show diminishing returns, and public transport use has declined significantly in countries like Latvia. These challenges call for a shift toward localised, evidence-based solutions, guided by citizen needs and enabled by innovative mobility strategies.

The above framework (Fig. 3) illustrates how systemic pressures – ranging from climate policy to funding inefficiencies – cascade down to influence households directly. In turn, these pressures necessitate highly adaptable local policies. Whether through flexible routing services, equity-conscious fare systems, or expanding shared vehicle access, such models offer a resilient and socially equitable response to mobility challenges. Importantly, successful implementation will rely on real-time data, participatory governance, and integrated transport-social policy frameworks. To address this evolving reality, a set of adaptive and locally deployable strategies has been identified:

- Microtransit and On-Demand Transport: Maintaining large public transport fleets on underutilised rural or peri-urban routes is increasingly uneconomical. A shift to flexible, smaller-capacity vehicles, operating on demand, can offer cost-efficient service while meeting real user needs [25];
- Shared Mobility Options: Car-sharing, bike-sharing, and e-bike rentals are rapidly emerging as viable solutions for those in settlements with limited fixed-route public transport. Such systems also reduce the need for car ownership, which is often unattainable for households in persistent poverty ([5], [24]);
- Smart Public Subsidies: Evaluation of public expenditure must go beyond cost-per-passenger metrics and include equity, accessibility, and social impact. Resources should be directed toward routes and modes that benefit those with the highest transport need [2];
- Fare System Reform: While fare discounts for seniors or students are common, they may inadvertently increase base fares for others. Targeted support must be economically sustainable and designed to avoid burden-shifting [4], [5];
- Cross-sector Policy Integration: Long-term success depends on deeper collaboration between transport, energy, housing, and social policy actors. For example, mobility needs assessments at the municipal or even neighbourhood level can help tailor solutions that respond to real usage patterns and energy constraints [1], [19].

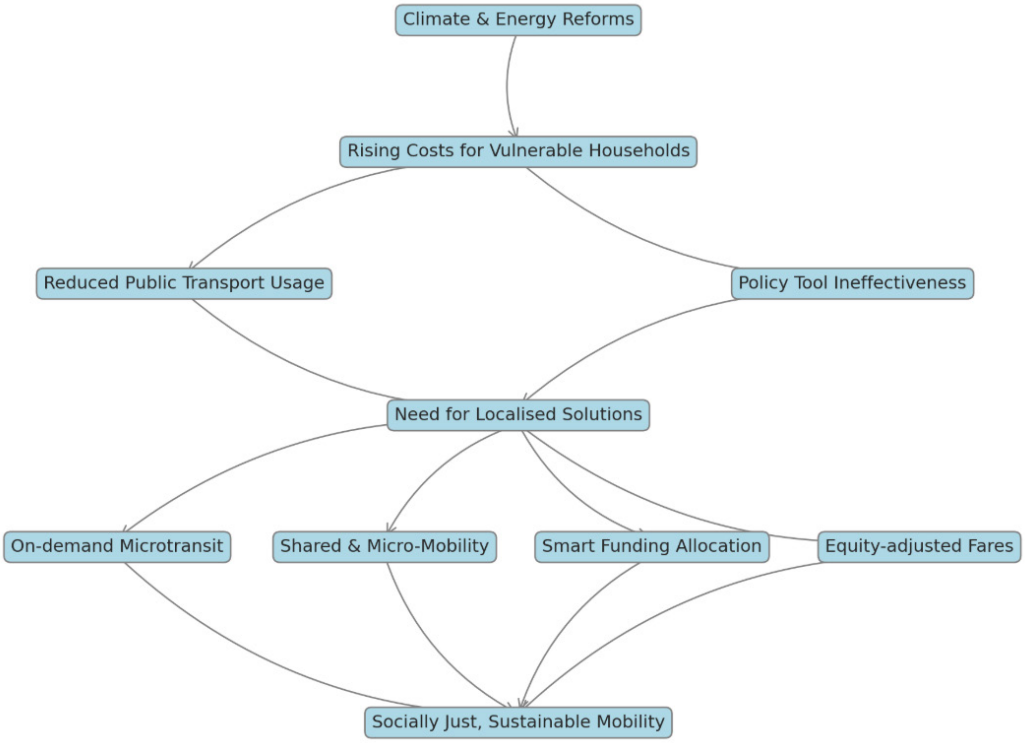

Fig. 3. Pathway to localised transport solutions.

Transport poverty, thus, is not merely a question of vehicle access or fuel price. It is a multidimensional phenomenon requiring locally grounded, socially responsive policy frameworks. The complexity of this challenge is further exacerbated by the energy transition, which, if poorly managed, could widen existing inequalities by shifting costs onto those least able to adapt [22], [24]. At the same time, it is important to be aware that each of these solutions requires ever closer cooperation of transport policy planners with social policy makers, including often looking for possible solutions locally – at the level of a local government or even a limited territory thereof, including in some cases also by accurately identifying potential users of services, studying their needs and mobility habits, as well as finding a solution that meets their needs.

7. CONCLUSIONS

This study has highlighted the emergence and intensification of transport poverty in Latvia and its broader relevance across the European Union, particularly under the current climate and energy transition frameworks. Using historical data from the Central Statistical Bureau of Latvia, we have identified a dramatic decline in public transport usage between 1990 and 2024: a sevenfold decrease in railway passenger turnover (from 144.5 million to 19.7 million passengers) and a fivefold decline in bus and coach transport (from ~500 million to ~100 million passengers annually). These trends underscore a structural deterioration in transport accessibility, especially in rural and low-density areas, coinciding with increased spatial inequality.

Eurostat data further reveal that nearly 48 % of Latvian households lack access to a private vehicle, which is among the highest rates in the EU. This figure rises sharply among low-income and elderly households, making them disproportionately vulnerable to transport exclusion. Additionally, data from the Latvian Energy Agency and recent EU-wide reports show that fuel and mobility costs now exceed 12–15 % of disposable household income for the lowest income quintile, surpassing the widely accepted 10 % affordability threshold.

The study identifies strong correlations between energy price shocks, such as those during the 2021–2022 crisis, and rising transport costs, particularly in countries with low public transport modal share and high dependence on fossil fuels. For instance, average fuel price increases of 35–40 % in Latvia during this period led to corresponding increases in household expenditure on mobility.

These conditions have created a “cost trap” where affected households cannot invest in energy-efficient housing or cleaner, more economical vehicles, reinforcing both energy and transport poverty. The research has also shown that low public transport density, especially in regions outside Riga, significantly reduces access to employment, healthcare, and education, thereby intensifying patterns of social exclusion.

To address these multi-layered challenges, the study proposes a conceptual

framework that treats transport and energy poverty as interlinked phenomena. Key localised solutions include microtransit services, shared mobility schemes, targeted fare subsidies, and integrated transport-social policy coordination. International examples such as Germany's EUR 9 transport ticket and France's rural mobility schemes illustrate the feasibility and effectiveness of such interventions when properly funded and adapted.

Transport poverty is not merely a logistical or infrastructural issue but a critical barrier to inclusive development, social resilience, and fair climate transitions. For Latvia and other EU Member States, integrating transport poverty into energy, climate, and social policy frameworks is an urgent necessity. Without decisive action, the dual burdens of energy and transport costs will continue to marginalise vulnerable populations and undermine the equity of the green transition.

ACKNOWLEDGEMENTS

The research has been funded by the Latvian Council of Science, project "Mitigating Energy Poverty through Innovative Solutions", project No. lzp-2023/1-0214.

REFERENCES

1. Kiss, M. (2022). *Understanding Transport Poverty.* European Parliamentary Research Centre. Available at: https://www.europarl.europa.eu/RegData/etudes/ATAG/2022/738181/EPRS_ATA(2022)738181_EN.pdf
2. Lucas, K., Mattioli, G., Verlinghieri, E., & Guzman, A. (2016). Transport Poverty and Its Adverse Social Consequences. *Proceedings of the Institution of Civil Engineers – Transport*, *169* (6), 353–365. Available at: https://www.icevirtuallibrary.com/doi/full/10.1680/jtran.15.00073
3. Ng, C. P., Law, T. H., Wong, S. V., & Kulanthayan, S. (2017). Relative Improvements in Road Mobility as Compared to Improvements in Road Accessibility and Economic Growth: A Cross-Country Analysis. *Transport Policy*, *60*, 24–33. https://doi.org/10.1016/j.tranpol.2017.08.004
4. Zemite, L., Jansons, L., Zeltins, N., Lappuke, S., & Bode, I. (2023). Blending Hydrogen with Natural Gas/Biomethane and Transportation in Existing Gas Networks. *Latvian Journal of Physics and Technical Sciences*, *60* (5), 43–55. doi: https://doi.org/10.2478/lpts-2023-0030
5. Savickis, J., Zemite, L., Zeltins, N., Bode, I., ansons, L. (2020). Natural Gas and Biomethane in the European Road Transport: The Latvian Perspective. *Latvian Journal of Physics and Technical Sciences*, *57* (3), 57–72. https://doi.org/10.2478/lpts-2020-0016
6. Buljan, A., & Badovinac, F. (2023). How did the 2021-2022 Energy Shock Impact the Prices of Transport Services for Consumers across EU Countries? *Transportation Research Procedia*, *73*, 133–142. https://doi.org/10.1016/j.trpro.2023.11.901
7. Luo, K., & Ye, Y. (2024). How Responsive are Retail Electricity Prices to Crude Oil Fluctuations in the US? Time-Varying and Asymmetric Perspectives. *Research in International Business and Finance*, *69*, 102234–102234. https://doi.org/10.1016/j.ribaf.2024.102234

8. Zemite, L., Backurs, A., Starikovs, A., Laizans, A., Jansons, L., Vempere, L., … Broks, A. (2023). A Comprehensive Overview of the Europen and Baltic Landscape for Hydrogen Applications and Innovations *Latvian Journal of Physics and Technical Sciences*, *60* (3), 33–53. https://doi.org/10.2478/lpts-2023-0016
9. Benassi, F., De Falco, A. (2025). Residential Segregation and Accessibility: Exploring Inequalities in Urban Resources Access Among Social Groups. Land, 14(2), 429. https://doi.org/10.3390/land14020429
10. Jensen, C. L., Andersen, L. M., Hansen, L. G., & Henningsen, G. (2020). Is Social Nudging too Emotionally Taxing? A Field Experiment of Public Utilities and Electricity Consumers in Denmark. *Energy Research & Social Science*, *67*, 101515. https://doi.org/10.1016/j.erss.2020.101515
11. European Commission. (Jun. 27, 2025). *Mobility and Transport.* Available at: https://transport.ec.europa.eu/index_en?prefLang=lv
12. Istituto Nazionale di Statistica. (2024). *Istat.it English*. Available at: https://www.istat.it/en/
13. BMVD. (2021). *BMDV – Startseite*. Available at: https://bmdv.bund.de
14. Eurostat. (2022). *Eurostat*. Available at: https://ec.europa.eu/eurostat
15. Central Statistical Bureau. (2023). *Services. Official Statistics*. Available at: https://www.csb.gov.lv/en
16. Kovács, G., & Spens, K. M. (2006). Transport Infrastructure in the Baltic States Post-EU Succession. *Journal of Transport Geography*, 14 (6), 426–436. https://doi.org/10.1016/j.jtrangeo.2006.01.003
17. Bogdanovs, A., Kucajevs, J., Steiks, I., Vitols, K., Zemite, L., & Krievs, O. (2021). Opportunity analysis of battery electric vehicle fast charging infrastructure development in Latvia. In *2021 IEEE 62nd International Scientific Conference on Power and Electrical Engineering of Riga Technical University (RTUCON*), (pp. 1–8), Riga, Latvia, 2021. https://doi.org/10.1109/rtucon53541.2021.9711718
18. Jasevics, A., Zemite, L., & Kunickis, M. (2017). Demand load control with smart meters. In *2017 IEEE 58th International Scientific Conference on Power and Electrical Engineering of Riga Technical University (RTUCON),* (pp. 1–6), Riga, Latvia, 2017. https://doi.org/10.1109/rtucon.2017.8124757
19. Bogdanova, O., Viskuba, K., & Zemīte, L. (2023). A Review of Barriers and Enables in Demand Response Performance Chain. *Energies*, *16* (18), 6699. https://doi.org/10.3390/en16186699
20. Mezulis, A., Kleperis, J., Lesnicenoks, P., & Zemite, L. (2022). Prospects of Decarbonising Industrial Areas in the Baltic States by Means of Alternative Fuels. *Journal of Ecological Engineering*, *23* (8), 151–160. https://doi.org/10.12911/22998993/150748
21. Kroics, K., Zemite, L., & Gaigals, G. (2017). Analysis of Advanced Inverter Topology for Renewable Energy Generation and Energy Storage Integration into AC grid. *Engineering for Rural Development,* 941 – 950. https://doi.org/10.22616/erdev2017.16.n192
22. Gorobetz, M., Korneyev, A., & Zemite, L. (2022). Long-term energy and fuel consumption forecast in private and commercial transport using artificial life approach. In *2022 IEEE 7th International Energy Conference (ENERGYCON)*, (pp. 1–7), Riga, Latvia, May 2022. https://doi.org/10.1109/energycon53164.2022.9830189
23. Kleperis, J., Dimanta, I., Sloka, B., & Zemite, L. (2022). What Hydrogen Can Bring to Rural Development: Review and Results of Entrepreneurs Survey in Latvia. *Research for Rural Development, 37*, 273–279. https://doi.org/10.22616/rrd.28.2022.039
24. Backurs, A., Zemite, L., Laizans, A., Bode, I., Starikovs, A., & Vempere, L. (2023). Towards sustainable transport: Evaluating potential of hydrogen fuel cell buses and trucks in Latvia. In *2023 IEEE 64th International Scientific Conference on Power and Electrical Engineering of Riga*

Technical University (RTUCON), (pp. 1–6), Riga, Latvia, 2023. https://doi.org/10.1109/rtucon60080.2023.10412884

25. U.S. Department of Transportation, & Federal Highway Administration. (2016). *Shared Mobility. Current Practices and Guiding Principles.* Available at: https://ops.fhwa.dot.gov/publications/fhwahop16022/fhwahop16022.pdf

sciendo

LATVIAN JOURNAL OF PHYSICS
AND TECHNICAL SCIENCES
2025, N 4

DOI: 10.2478/lpts-2025-0028

INVESTIGATION OF PERTAMAX (GASOLINE) POOL FIRE IN CONFINED COMPARTMENT

T. Rohman[1]*, S. F. Junjunan[1], M. A. Moelyadi[2]

[1]National Research and Innovation Agency (BRIN),
Jalan Jendral Gatot Subroto 10, Jakarta, 12710, INDONESIA
[2]Bandung Institute of Technology (ITB),
Jl Tamansari no 64, Bandung, 40116, INDONESIA
*e-mail: tauf019@brin.go.id

An understanding of fire is needed as a basis for fire suppression, especially in a compartment. Large fires can cause material losses and loss of life, as well as the release of toxic substances into the environment. These fires can be triggered by fuel leaks that form pool fires. Therefore, the characteristics and behaviour of the fire in the compartment were investigated. Experiments were conducted inside a cube-shaped compartment measuring 1.2 m3 in volume with three square pool pans: 14, 21, and 28 cm. The fuel used was Pertamax, an engine fuel produced by Pertamina and commonly used in Indonesia. The experimental results showed that the size of the fire indicated by the Heat Release Rate (HRR) value was influenced by the cross-sectional area of the pool fire, which would affect the maximum temperature and duration of the flame in the closed compartment. This is related to the heat flux and oxygen consumption rate. Numerical simulations were also carried out using the Fire Dynamics Simulator (FDS version 6.7.9), yielding results that closely matched the experimental results, with differences of less than 20 % for the HRR value. It is expected that by knowing the characteristics and behaviour of the fire, research can be continued on the fire extinguishing system in the compartment.

Keywords: *Confined compartment, fire dynamics, heat release rate (HRR), Pertamax, pool fire, simulator (FDS).*

1. INTRODUCTION

Research on the characteristics of both indoor and outdoor fires has been conducted both analytically and experimentally for a long time. In general, however, analytical models [1] do not capture the complexity of this phenomenon because they often make one or more simplifying assumptions, such as ignoring some forms of displacement or holding flame temperatures and chemical species concentrations constant. One of the analytical approaches is the study by Palazzi et al. on pool fires in hydrocarbons inside semi-enclosed compartments [2], [3].

Many experimental studies have been conducted in the past to achieve realistic solutions. Experimental results show that pool fire is affected by a number of coupled parameters, such as pool geometry, fuel type, ambient conditions, etc. [4]. Some examples of experimental studies were conducted by Soleh et al. using heptane as a fuel source [5]. Then some use methanol, ethanol, and various other fuels as pool fire sources both inside the compartment and outdoors [6]–[8]. Additionally, experimental studies have been conducted to examine the fire characteristics within aircraft cargo compartments [9], [10].

Recent research shows that the use of numerical simulation is becoming a trend in analysing fire characteristics, as Tuovinen simulated hydrocarbon combustion in a ventilated room using CFD [11]. Hyde and Moss modelled CO production in a compartment fire based on a laminar flamelet relation [12]. Currently, many numerical simulation studies are being conducted in conjunction with experiments to obtain valid results [13]–[15].

2. EXPERIMENTAL

The compartment used is cube-shaped with a size of 100 cm x 100 cm x 120 cm and made of stainless steel. There are side and front glass windows for visual recording. On the inside, there is a load cell holder to measure the mass of the reduced fuel. Four type-K thermocouples are mounted vertically with a distance between thermocouples ±10 cm parallel to the pool pan. These thermocouples have a maximum temperature capacity of 1200 °C. Oxygen sensors are mounted on the top side of the compartment. This sensor is used to measure the oxygen concentration in the compartment during the experiment. All sensors are connected to a data logger to store the data. Three square pool pans measuring 14 cm (Pan 14), 21 cm (Pan 21), and 28 cm (Pan 28) were used as fuel containers made of 1 mm-thick stainless steel. The setup of the test equipment is shown in Fig. 1.

The fuel used is Pertamax, which is an engine fuel issued by Pertamina and has an octane level of 92. Pertamax is made from HOMC, RCC gasoline, and polygasoline, utilising a product blending process in a blending pool processing unit. This fuel has a density of 715–770 kg/m^3 (at 15 °C), a vapour pressure of 45–60 kPa, and a boiling point of 215 °C [16].

Fig. 1. Schematic and position of sensors inside confined compartment.

3. NUMERICAL SIMULATION

CFD modelling is commonly used in several engineering disciplines to analyse fire dynamics. CFD is used in weather forecasting, aerodynamics, and turbomachinery technology, as well as in closed fire modelling [17]. CFD models are based on time-dependent three-dimensional conservation laws. The simulated domain is divided into many sub-volumes where the laws of momentum, mass and energy conservation are applied to each sub-volume [18].

3.1. Grid Dimension

In the fire scenario, the relationship between the fire characteristic diameter, D*, and the grid cell size, δx, will indicate the accuracy of LES modelling of fluid motion on the sub-grid. The cell dimensions are chosen based on the rule of thumb that the plume resolution, RI, should be greater than or equal to 10, which means that the fire characteristic diameter, D*, should span 10 or more cells [19].

$$RI = \frac{D^*}{\delta x}. \tag{1}$$

$$D^* = \left(\frac{\dot{Q}}{\rho_\infty T_\infty Cp\sqrt{g}}\right)^{2/5}, \tag{2}$$

where $\dot{Q}$ is the total HRR (W) and δx is the grid cell width (m).

3.2. Gas Phase Equations

FDS solves the Navier-Stokes equations at low Mach numbers using Large Eddy Simulation (LES) as the turbulence model. The low Mach number approach

defines the pressure as a combination of background pressure $\bar{P}$ and disturbance $\tilde{P}$. The background pressure is given using the ideal gas law:

$$\bar{P} = \frac{\rho R_g T}{W}, \tag{3}$$

where ρ is density (kg·m^{-3}), R_g is the universal gas constant (J·mol^{-1}·K^{-1}), T is temperature (K), and W is molecular weight (kg·mol^{-1}). The momentum equation is expressed as follows:

$$\frac{\partial \boldsymbol{u}}{\partial t} - \underbrace{\boldsymbol{u} \times \omega - \frac{1}{\rho}[(\rho - \rho_\infty)g + \nabla.\tau]}_{\text{Advective}} + \nabla H_p - \underbrace{\tilde{P}\nabla\frac{1}{\rho}}_{\text{Baroclinic}} = 0. \tag{4}$$

$$H_p = \frac{|\boldsymbol{u}^2|}{2} + \frac{\tilde{P}}{\rho}. \tag{5}$$

Default turbulence model in FDS to approximate the viscous stress tensor is the Deardorff turbulence model [20] is used, along with other turbulence models such as the constant coefficient Smagorinsky model [21] and the dynamic Smagorinsky model [22]. The conservation equations for mass, species, and energy are as follows:

$$\frac{\partial \rho}{\partial t} + \nabla.(\rho \boldsymbol{u}) = 0; \tag{6}$$

$$\frac{\partial(\rho y_i)}{\partial t} + \nabla.\rho y_i \boldsymbol{u} = \nabla.(\rho D_g)_i \nabla y_i + \dot{m}'''; \tag{7}$$

$$\frac{\partial(\rho h_s)}{\partial t} + \nabla.(\rho h_s \boldsymbol{u}) = \frac{\partial \bar{P}}{\partial t} + \boldsymbol{u}.\nabla\bar{P} + \dot{Q}''' - \nabla\dot{\boldsymbol{Q}}''; \tag{8}$$

$$\dot{\boldsymbol{Q}}'' = -k\nabla T - \sum_i h_{s,i}\rho D_i \nabla Z_i + \dot{Q}_r''. \tag{9}$$

The conservation equations are solved simultaneously for velocity, temperature, pressure, and mixing fraction at a given time step using an explicit second-order predictor/corrector scheme. The pressure and momentum equations are coupled during the iteration procedure. First the advective and baroclinic parts of the momentum equation are calculated, then the pressure equation is solved several times until the normal components of velocity and background pressure converge to a certain tolerance. The velocity is then recalculated for the next time step. The procedure is iterated until the velocity and pressure converge to a certain tolerance.

4. COMBUSTION MODELLING

The technique used is the mixing fraction of combustion. This technique is based on the assumption that conduction and radiation transfer phenomena occur on a large scale in addition to physical processes that occur on a small scale over time. The chemical model in FDS is the following simple chemical model, which will then be used to calculate the stoichiometric coefficients:

$$C_x H_y O_z N_v + \nu_{O_2} O_2 \rightarrow \nu_{CO_2} CO_2 + \nu_{H_2O} \;\; H_2O + \nu_{CO} CO + \nu_s Soot + \nu_{N_2} N_2.$$

The stoichiometric equations used to solve fuel and oxidizer consumption rates are:

$$\frac{\dot{m}_F^{"}}{\nu_F M_F} = \frac{\dot{m}_O^{"}}{\nu_O M_O}. \quad (10)$$

While the mixing fraction equation after including the element of the basic conservation law is:

$$\rho \frac{DZ}{Dt} = \nabla . \rho D \nabla Z. \quad (11)$$

From the above equation, the rate of oxygen consumption per unit mass can be derived again to obtain the rate of oxygen consumption per unit mass at any time, as shown in the equation below.

$$-\dot{m}_O^{"} = \frac{dY_O}{dZ}|_{Z<Zf}\, \rho D \nabla Z . \boldsymbol{n}. \quad (12)$$

5. THERMOCOUPLE MODELLING

The FDS thermocouple model is used to compare the temperature field calculated in FDS with the temperature uncorrected experimental data. This allows the simulation to account for the thermocouple's thermal mass and radiant heat loss. The thermocouple temperature (T_{TC}) is found by solving the energy balance around the thermocouple:

$$\rho C_p \frac{dT_{TC}}{dt} = \varepsilon \left(\frac{U}{4} - \sigma T_{TC}^4\right) + h(T_g - T_{TC}), \quad (13)$$

where ε is the thermocouple emissivity, h is the convection heat transfer coefficient (W·m-2K-1), and T_g is the actual gas temperature (K). Since all thermocouples are type K, the density, heat capacity, and emissivity are set at nickel material with ρ = 8909 kg·m^{-3} and Cp = 0.44 kJ·kg^{-1}·K^{-1}, and ε = 0.9.

6. GEOMETRY DOMAIN

The geometry domain corresponds to the interior of the compartment, with the position and size of the pan determined by the test scenario. Thermocouples and oxygen sensors are installed at the test positions to view temperature values and oxygen levels. The simulated fuel mass is 100 g for all pan sizes. The simulation parameter data is presented with the simulation domain shown in Fig. 2. The Pertamax property data in Table 1 are the values from the literature case that uses gasoline as the fuel.

Table 1. Properties of Pertamax

CO Yield	0.016 kg/kg
Soot Yield	0.051 kg/kg
Heat of combustion	44700 kJ/kg
Density	723 kg/m^3
Specific heat	2.22 kJ/(kg·K)
Conductivity	0.124 W/(m·K)

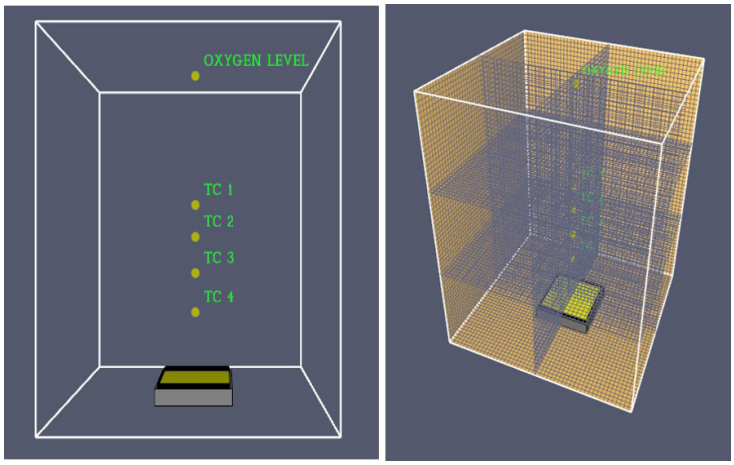

Fig. 2. Simulation domain and setup.

7. RESULTS AND DISCUSSION

Pan 14 has the smallest cross-sectional area, resulting in a small flame size and thus a long flame duration. This is evident in Figure 3, which shows the oxygen level decreasing gradually until it is extinguished at the 9 % concentration level. The long duration of the flame causes the temperature inside the compartment to be the highest compared to the other pan sizes, as seen in Fig. 3. The numerical simulation also shows the same trend as the experimental results.

Pan 21 and Pan 28 have similar characteristics because the combustion mode is optically thin and radiative in contrast to Pan 14, which forms turbulence and is convective. This is in accordance with the definition by Baubraska [1983], which describes the burning mode in pool fire based on the diameter of the pan (in this experiment, approximated by a square diagonal line). The definition is shown in Table 2 [23].

Table 2. Pool Diameter and Burning Mode

Pool diameter (cm)	Burning mode
< 5	Laminar, convective
5–20	Turbulent, convective
20–100	Optically thin, radiative
> 100	Optically thick, radiative

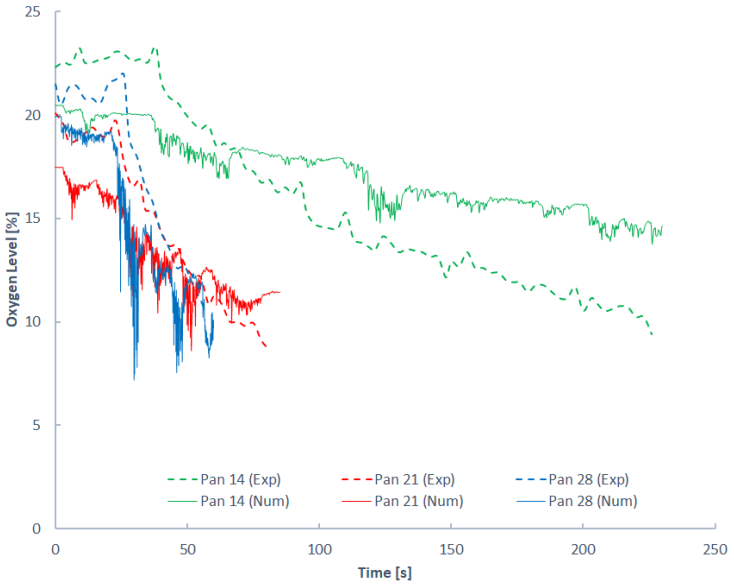

Fig. 3. Concentration of oxygen during fire burning until flames out.

The maximum temperature measured on the thermocouple has a graphical trend that is close between the experiment and the simulation as seen in Fig. 4. There is something different in Pan 14 compared to the other pan, namely, the value of the simulation is lower than that of the experiment. This is related to the longer duration of the flame in the compartment so that the sensitivity of the thermocouple sensor increases. The difference in maximum temperature values in all pans is due to incomplete fuel property values (Pertamax), so it is combined with fuel data from the literature.

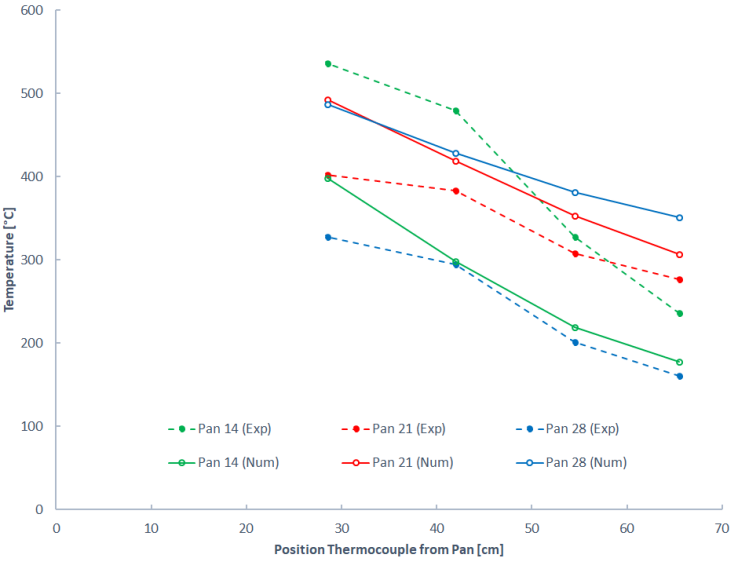

Fig. 4. Maximum temperature at each thermocouple.

A large HRR results in a faster fuel consumption rate so that the oxygen levels in the compartment are quickly depleted and the fire goes out. This is inversely proportional to the maximum temperature value. Due to the short flame duration, the heat flux is also short as shown in Fig. 5.

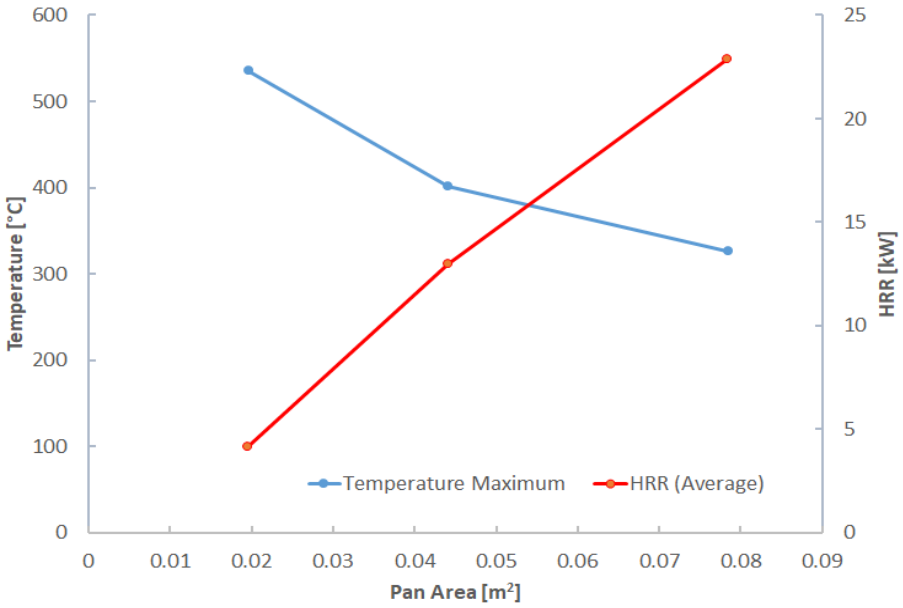

Fig. 5. Effect of pan area to temperature maximum and HRR.

The comparison of experimental results with simulation is presented in Table 3 and Fig. 6. The relatively small percentage difference in HRR indicates that the numerical modelling performed is close to the experimental results. As for the maximum temperature value, the difference is still quite large due to the fuel properties that are not in accordance with those used in experiments.

Table 3. Comparison of Experiment and Simulation

	T_{max} (°C)		HRR Average (kW)		$\%\Delta T_{max}$	%Δ HRR
	Exp	Num	Exp	Num		
Pan 14	536	398	4.16	4.05	-25.7	-2.6
Pan 21	402	493	12.97	10.64	22.7	-18.0
Pan 28	327	487	22.85	23.34	48.8	2.1

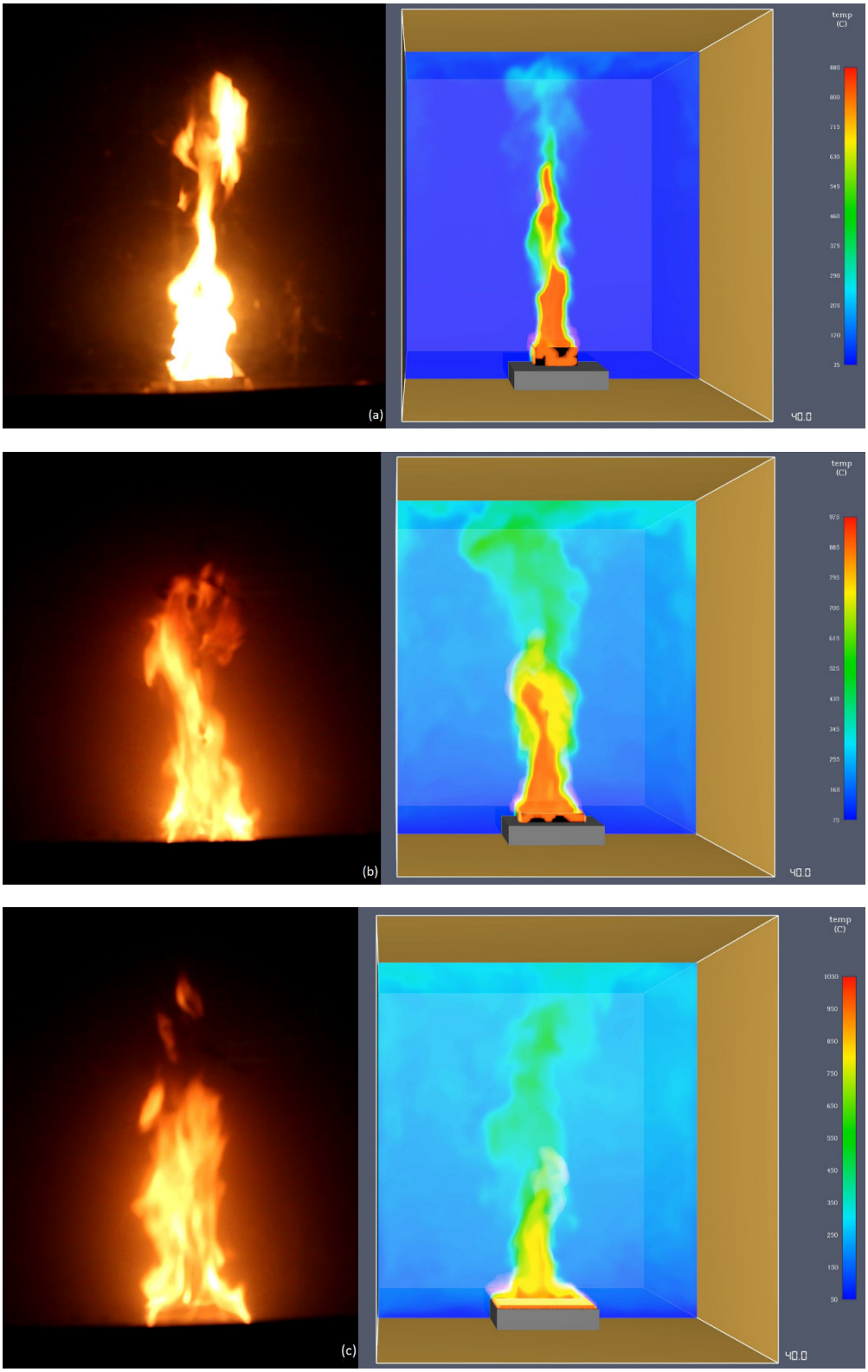

Fig. 6. Comparison simulation and experiment at t=40s (a) Pan 14, (b) Pan 21, and (c) Pan 28.

8. CONCLUSION

The aim of this research has been to obtain data on the behaviour and characteristics of a fire in an enclosed compartment using a computational simulation study and then validate by experimental testing. From the work performed, it has been concluded that the characteristics of a fire in a closed compartment are affected by the cross-sectional area of the pan. The trend is that the HRR value increases as the cross-sectional area of the pan increases. An increase in HRR requires more oxygen, so the oxygen content in the closed compartment decreases rapidly. Therefore, the heat flux lasts for a short time as the flame extinguishes.

Flame size affects the flame shape and the combustion mode. A larger flame indicates a more turbulent flame. Flame size increases the total heat flux and the average temperature in the compartment, even though this occurs at the maximum temperature in the compartment. The increased heat flux and average temperature in the compartment and the depletion of the oxygen concentration lead to more production of unburned gas and vaporized fuel, which causes flashover in the compartment. At the same time, however, the low oxygen level causes the fire in the compartment to self-extinguish. These combustion phenomena can occur simultaneously and interact with each other.

Numerical simulations using FDS are strongly influenced by input parameters, including fuel properties. Differences in values will lead to differences with experimental results. More in-depth studies are needed to improve the accuracy and validation of numerical simulation results so that they can be used as a reference in the design of fire suppression systems in buildings or compartments.

REFERENCES

1. Armendáriz, J., & Matalon, M. (2001). Evaporation and Combustion of Thin Films of Liquid Fuels. *Journal of Fluid Mechanics, 435*, 351–376. https://doi.org/10.1017/S002211200100413X
2. Palazzi, E., & Fabiano, B. (2012). Analytical Modelling of Hydrocarbon Pool Fires: Conservative Evaluation of Flame Temperature and Thermal Power. *Process Safety and Environmental Protection, 90* (2), 121–128. https://doi.org/10.1016/j.psep.2011.06.009
3. Palazzi, E., Caviglione, C., Reverberi, A. P., & Fabiano, B. (2017). A Short-Cut Analytical Model of Hydrocarbon Pool Fire of Different Geometries, with Enhanced View Factor Evaluation. *Process Safety and Environmental Protection, 110*, 89–101. https://doi.org/10.1016/j.psep.2017.08.021
4. Joulain, P. (1998). The Behavior of Pool Fires: State of the Art and New Insights. *Symposium (International) on Combustion, 27* (2), 2691–2706. https://doi.org/10.1016/S0082-0784(98)80125-2
5. Junjunan, S. F., Chetehouna, K., Cablé, A., Abdlgwad, A., Oger, A., & Bura, R. O. (2022). Study of heptane pool fire in well-confined military vehicle engine compartment. In *Proceedings of CONV-22: Int. Symp. on Convective Heat and Mass Transfer.* 5–10 June 2022, Turkey, Begel House Inc. https://doi.org/10.1615/ICHMT.2022.CONV22.200
6. Chan Kim, S., Lee, K. Y., & Hamins, A. (2019). Energy Balance in Medium-Scale Methanol, Ethanol, and Acetone Pool Fires. *Fire Safety Journal, 107,* 44–53. https://doi.org/10.1016/j.firesaf.2019.01.004

7. Sahu, D., Jain, S., Gupta, A., & Kumar, S. (2019). Experimental Studies on Different Liquid Pool Fires inside the Compartment. *Fire Safety Journal, 109,* 102858. https://doi.org/10.1016/j.firesaf.2019.102858
8. Tian, X., Liu, C., Zhong, M., & Shi, C. (2020). Experimental Study and Theoretical Analysis on Influencing Factors of Burning Rate of Methanol Pool Fire. *Fuel, 269,* 117467. https://doi.org/10.1016/j.fuel.2020.117467
9. Pathak, A., Norrefeldt, V., & Pschirer, M. (2021). Validation of a Simulation Tool for an Environmentally Friendly Aircraft Cargo Fire Protection System. *Aerospace, 8* (2), 35. https://doi.org/10.3390/aerospace8020035
10. Tao, Z., Yang, W., Sun, Z., Chen, M., Wang, J., Yang, R., & Zhang, H. (2022). Experimental Study of Oil Pool Shape and Environment Pressure on the Wall Fire Behavior in an Airplane Cargo Compartment. *International Journal of Thermal Sciences, 174,* 107440. https://doi.org/10.1016/j.ijthermalsci.2021.107440
11. Tuovinen, H., & McNamee, M. (2000). *Incorporation of Detailed Chemistry in CFD Modelling of Compartment Fires.* ISFEH, Lake Windermere.
12. Hyde, S. M., & Moss, J. B. (2003). Modelling CO Production in Vitiated Compartment Fires. *Fire Safety Science, 7*, 395–406.
13. Brohez, S., Saladino, D., & Perelli, M. (2022). Experimental and Numerical Study of Heptane Pool Fire. *Chemical Engineering Transactions, 91,* 223–228. https://doi.org/10.3303/CET2291038
14. Kumar, A., Kumar, R., & Ansari, A.A. (2022). Experimental and Numerical Simulation Studies of Liquefied Petroleum Gas Fire in a Full–Scale Compartment. *Process Safety Progress, 41* (1), 195–206. https://doi.org/10.1002/prs.12292
15. Li, J., Beji, T., Brohez, S., & Merci, B. (2021). Experimental and Numerical Study of Pool Fire Dynamics in an Air-Tight Compartment Focusing on Pressure Variation. *Fire Safety Journal, 120*, 103128. https://doi.org/10.1016/j.firesaf.2020.103128
16. Pertamina. (2021). *Product-IFM: Pertamax, Pertamina.* Available at: https://onesolution.pertamina.com/Product/Download?filename=20210806090201atc_Pertamax%20Spesifikasi.pdf
17. Yeoh, G. H., & Yuen, K. K. (2009). *Computational Fluid Dynamics in Fire Engineering: Theory, Modelling and Practice*. Butterworth-Heinemann, 545.
18. Karlsson, B., & Quintiere, J. G. (2022). *Enclosure Fire Dynamics.* (2nd ed.). CRC Press.
19. McGrattan, K. B., McDermott, R. J., Weinschenk, C. G., & Forney, G. (2013). *Fire Dynamics Simulator, Technical Reference Guide.* (6th ed.). NIST.
20. Deardorff, J. W. (1980). Stratocumulus-Capped Mixed Layers Derived from a Three-Dimensional Model. *Boundary-Layer Meteorology, 18* (4), 495–527. https://doi.org/10.1007/BF00119502
21. Smagorinsky, J. (1963). General Circulation Experiments with the Primitive Equations: I. The Basic Experiment. *Monthly Weather Review, 91* (3), 99–164. https://doi.org/10.1175/1520-0493(1963)091<0099:GCEWTP>2.3.CO;2
22. Germano, M., Piomelli, U., Moin, P., & Cabot, W. H. (1991). A Dynamic Subgrid-Scale Eddy Viscosity Model. *Physics of Fluids A: Fluid Dynamics, 3* (7), 1760–1765. https://doi.org/10.1063/1.857955
23. Babrauskas, V. (1983). Estimating Large Pool Fire Burning Rates. *Fire Technology, 19* (4), 251–261. https://doi.org/10.1007/BF02380810

sciendo

LATVIAN JOURNAL OF PHYSICS
AND TECHNICAL SCIENCES
2025, N 4

DOI: 10.2478/lpts-2025-0029

ANALYSIS OF STRUCTURAL RELIABILITY OF MAIN GAS PIPELINES

G. G. Ismayilov[1], F. B. Ismayilova[1]*, A. R. Nagizadeh[2]

[1]Azerbaijan State Oil and Industry University,
16/21 Azadlig Ave., Baku, AZ1010, AZERBAIJAN
[2]Oil and Gas Scientific Research Project Institute,
SOCAR, 88A H.Zardabi, Baku, AZ1122, AZERBAIJAN
*e-mail: fidan.ismayilova.2014@mail.ru

The possibility of future operation of pipelines that are under exploitation is one of the most important issues of the oil and gas industry. Therefore, it is necessary to periodically check (diagnose) the technical condition of pipelines. Taking into account the operating conditions, the thickness losses may occur during the operation period.

The paper investigates the residual operating resources of various elements of the pipeline as a result of diagnostic work, as well as the calculation of the wall thickness of the main gas pipeline with methods based on modern technologies. Both analytical methods and modern software were used during the calculations. A three-dimensional spatial model of the pipeline was created via the software, and the strength and stability of the pipeline under the influence of various forces were calculated. Subsequently, following technical diagnostics of the pipeline, the possibility of further operation of the pipe element was determined.

Keywords*: Allowable stress, design resistance, main gas pipeline, reliability coefficient, strength, yield strength.*

1. INTRODUCTION

Main gas pipelines are complex structures, usually of large diameter, transporting natural gas at high pressures, and are considered hazardous production facilities. Main gas pipelines pass through various geological and climatic zones and fulfil a major function – reliable gas supply to the consumer.

As an integral part of gas production facilities, main gas pipelines have been exposed to several external and internal factors from the moment they are put into oper-

ation. Loads and impacts on gas pipelines have a wide range and include gas pressure and temperature, vibration loads on pipelines from compressor stations, wind loads on aboveground pipelines, hydrodynamic loads on underwater passages, etc. These effects cause losses in various elements of the pipeline, especially in the wall thickness of the pipeline. Defects in the welding elements that connect the various components of the pipe (linear section, elbow, transition, etc.) can lead to a reduction in the pipeline's service life or even shutdown the pipeline. In order to keep all these effects under control and to avoid negative consequences, it is important to carry out periodic inspections of pipelines.

Currently, a number of periodic inspection and monitoring methods are implemented in practice to address the stated problems and to increase the structural reliability of the pipelines. Conducted diagnostic measures play an important role in detecting potential hazards that may occur in the pipeline due to the influence of a number of static and dynamic loads. The purpose of carrying out the inspection is to determine the possibility of future operation of oil and gas pipelines [1]–[3].

2. RESEARCH METHODOLOGY

Taking into account the above-mentioned, the aim of the study is to determine the residual operating resources of various elements of the pipeline as a result of diagnostic work. In the studies, the process was modelled using the STAAD.Pro 3D Structural Analysis and Design Software, and the wall thickness of the gas pipeline was determined as a result of mathematical calculations.

The analysis of the state of operation of the studied main pipeline was carried out in the following order.

2.1. Determination of Pipeline Resistance to Tension (Compression)

To determine the structural reliability of the main pipelines in operation, as the first step, the minimum value of the pipe resistance to tension R_1^n and compression R_2^n (tensile strength and yield strength) must be determined [4]–[6]:

$$R_1 = \frac{{R_1}^n \times m}{k_1 \times k_e};\ R_2 = \frac{{R_2}^n \times m}{k_2 \times k_e},$$
$$R = min\{R_1;\ R_2\}, \quad (1)$$

where
${R_1}^n$ – normative resistance, MPa;
${R_2}^n$ – yield strength, MPa;
m – pipeline operating condition coefficient;
k_1, k_2 – reliability factors for material;
k_e – the reliability factor for the purpose of the pipeline.

The values of the coefficient of operating conditions that are used in calculating the strength, stability, and deformation of the pipeline and depend on the category of the pipeline are given in Table 1 [7].

The reliability coefficients for the material depending on the purpose of the pipeline are selected according to Tables 2–4, respectively [8]–[10]:

Table 1. Coefficient of Operating Conditions

Category of the pipeline and its area	Pipeline strength, stability and the coefficient of working conditions when calculating deformation, m
In more important areas, such as inside buildings, compressor stations, underground gas storages, and water passages of oil pipes with a diameter of Ø1200 mm. B	0.60
Water crossings of main pipelines, railway crossings, highways, difficult-to-cross swamps, intersections with compressor stations, pigging launcher and receiver points I və II	0.75
III	0.90
IV	0.90

Table 2. Reliability Factor According to the Material

Pipe specifications	Reliability factor according to the material, k_1
100 % controlled rolling steel and thermally strengthened welded pipelines with the whole process seam safe method	1.34
Double-sided arc welding, rolled and forged seamless pipes with the whole process seam safe method	1.40
Pipes welded from low alloy or carbon steel, 100 % controlled, safe or non-destructive, made by double-sided electric arc welding	1.47
Welded pipes and other seamless pipes of low alloy or carbon steel, double arc welded	1.55

Table 3. Reliability Factor According to the Material

Pipe specifications	Reliability factor according to the material, k_2
Low carbon, seamless	1.10
According to $R_2^n/R_1^n \leq 0.8$ low-carbon and low-alloy straight seam and spiral seam, welded	1.15
Made of high – strength steel $R_2^n/R_1^n > 0.8$	1.20

Table 4. Reliability Factor for the Purpose of the Pipeline

Nominal pipe diameter, mm	Reliability factor for the purpose of the pipeline, k_r			
	For gas pipeline			For oil and oil products
	P≤5.4 MPa	5.4<P≤7.4MPa	7.4<P≤9.8MPa	
Up to 500	1.00	1.00	1.00	1.00
600–1000	1.00	1.00	1.05	1.00
1200	1.05	1.05	1.10	1.05
1400	1.05	1.10	1.15	-

2.2. Determination of the Pipeline Wall Thickness

The calculated thickness δ (mm) of the pipeline, which provides the necessary strength at a given working (standard) pressure P, is calculated using the following formula [4], [5]:

$$\delta = \frac{n \cdot P \cdot D}{2(R + n \cdot P)}, \quad (2)$$

where
P – operating pressure, MPa;
n – reliability factor due to load;
D – external diameter of the pipe, mm;
R – allowable stress for steel, MPa.

2.3. Conducting Technical Inspection Studies of the Underground Main Gas Pipeline – "Astara-Gazimammad" (Azerbaijan)

The main purpose of technical inspection is to identify potentially dangerous sections of the pipeline, assess the degree of danger of defects, determine the priority of dangerous sections and carry out preventive repairs [11], [12].

According to the current technical task:

- Length of the pipeline – L=210 km;
- External diameter of the pipeline – D=1220 mm;
- Design pressure of the pipeline – P_{design}=5.5 MPa;
- Maximum allowable operating pressure – $P_{operating}$ = 1.8 MPa;
- Type of steel – 17Г1С-У [10].

During the technical diagnostics, gauge measurements were performed by using an OLYMPUS 27 MG Ultrasonic Thickness Gauge. Based on the actual data obtained in the studies, the minimum allowable thicknesses corresponding to the existing internal pressure in the pipeline were calculated and compared with the actual minimum thicknesses. Thus, the possibility of safe operation of the gas pipeline was studied on the basis of gauge measurements, minimum thicknesses, and operational loads.

3. RESULTS AND DISCUSSION

The assessment of the safe operating reserves of the studied pipeline was determined, taking into account the surface defects observed as a result of direct measurements. The actual minimum cross-sectional thicknesses were based on the results of the stress calculation under internal pressure.

As a result of the measurement carried out at pressure of P=1.8 MPa at L=187.74th km of the "Astara-Gazimammad" underground main gas pipeline, the wall thickness of the pipeline was determined in different places:

- on the top – 12.18; 12.24; 12.36; 12.45; 12.40; 12.58; 12.65 mm (δ_{min} = 12.18 mm),
- on the side – 11.96; 11.95; 11.80; 11.91; 11.96; 11.93; 11.98 mm (δ_{min} = 11.80 mm),
- on the bottom – 9.85; 9.64; 9.49; 9.19; 9.25; 9.30; 9.38; 9.48 mm (δ_{min} = 9.19 mm).

Also, corrosion pits with a depth of 5÷6 mm and layered corrosion products were found on the side and bottom surface of the pipe.

The calculated value of the required minimum thickness of the pipe cross-section at given conditions is determined:

$$\delta = \frac{n \cdot P \cdot D}{2(R + n \cdot P)} = \frac{1.1 \cdot 1.8 \cdot 1220}{2(260.87 + 1.1 \cdot 1.8)} = 4.6 \text{ mm}$$

As a result of the comparison of the result obtained in the measurement performed on the bottom surface of the pipe (taking into account the corrosion pits) with the calculated value, it was determined that this section of the pipeline was no longer suitable for operation.

3.1. Creating a Constructive Model

The strength and durability analysis of the pipe was performed using the standard STAAD.Pro Connect Edition software (OMAE 2008-57836). STAAD is a popular structural analysis application known for analysis, diverse applications of use, interoperability and time-saving capabilities. STAAD helps structural engineers perform 3D structural analysis and design for both steel and concrete structures. A physical model created in the structural design software can be transformed into an analytical model for structural analysis. Many design code standards are incorporated into STAAD to make sure that the structural design complies with local regulations.

A simple diagram of a simulated main gas pipeline with a diameter of 1220 mm is shown in Fig. 1.

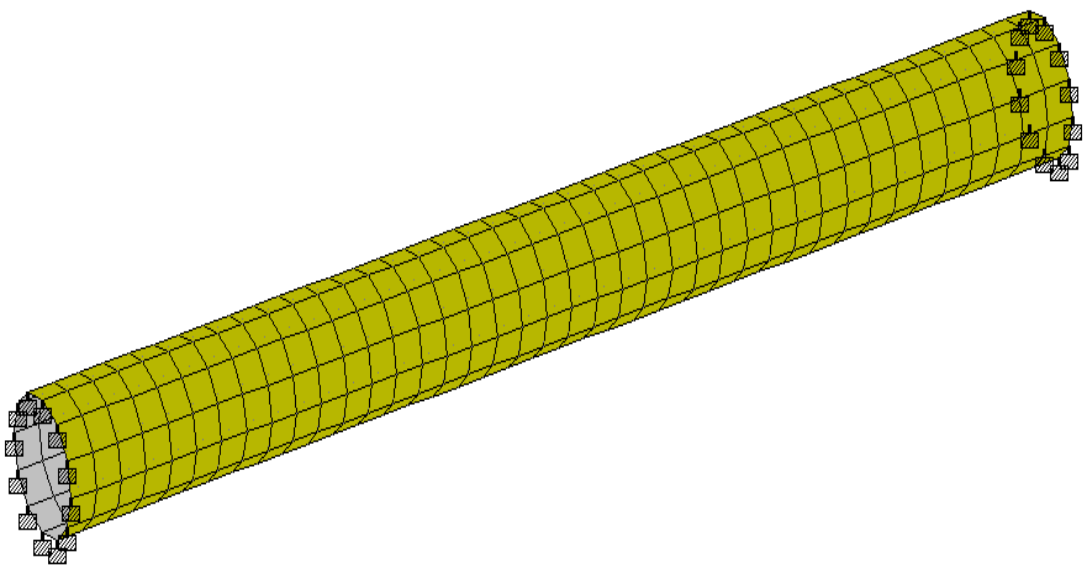

Fig. 1. Simplified model of the gas pipeline.

The characteristics of the steel used at the 187.74th km section of the Astara-Gazimamed underground gas pipeline are given in Table 5.

Table 5. The Properties of the Steel

Indicators	Actual Dimensions
Density, kg/ m^3	7849
Modulus Elasticity, E , MPa	200000
Shear modulus, G , MPa	77220
Poisson's ratio	0.3
Yield stress, MPa	245

3.2. Distribution of Applied Loads

The applied mathematical modelling took into account the operating pressure generated in the pipeline, including the mass of the metal. The load distribution scheme is shown in Fig. 2.

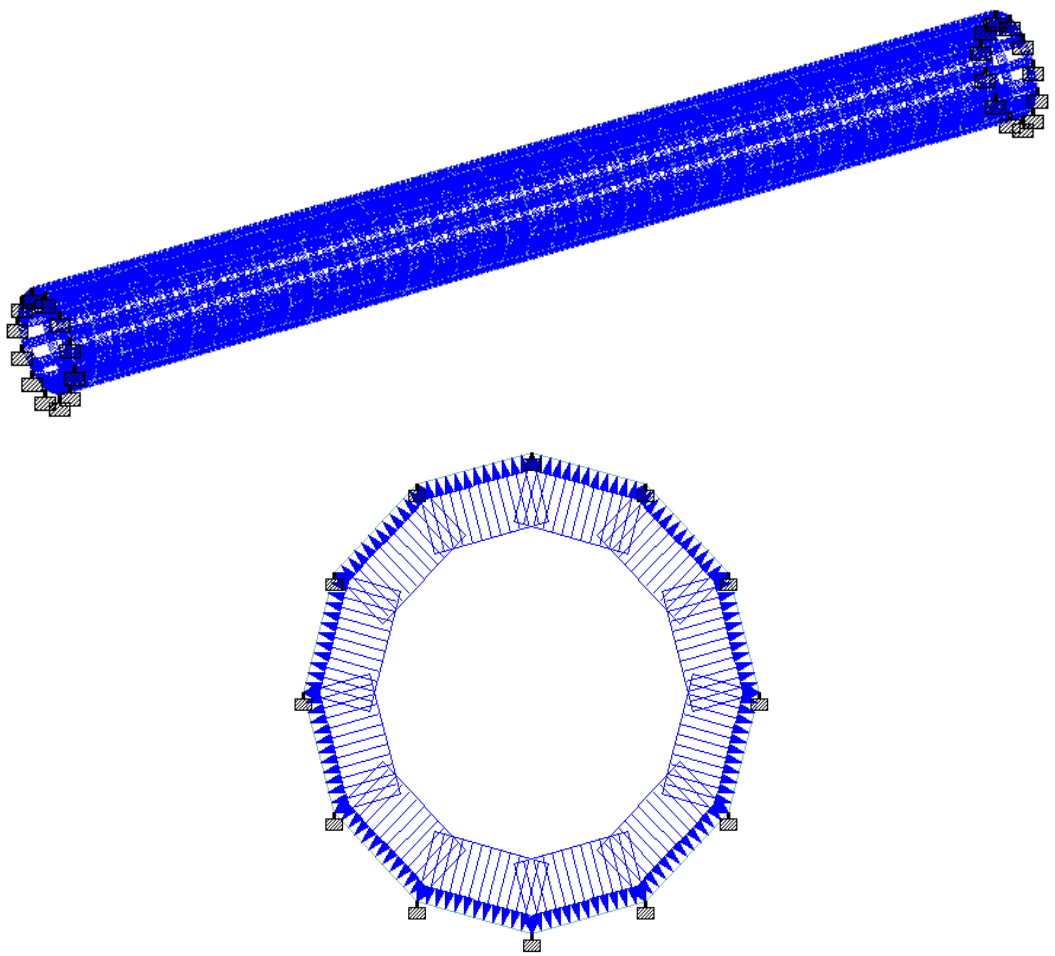

Fig. 2. Distribution of applied loads along the surface of the pipe.

3.3. Determination of the Stress Concentration Zone

It was determined that the maximum value of the yield stress in the pipeline, due to the effect of the applied load combination, was 379 MPa (Fig. 3).

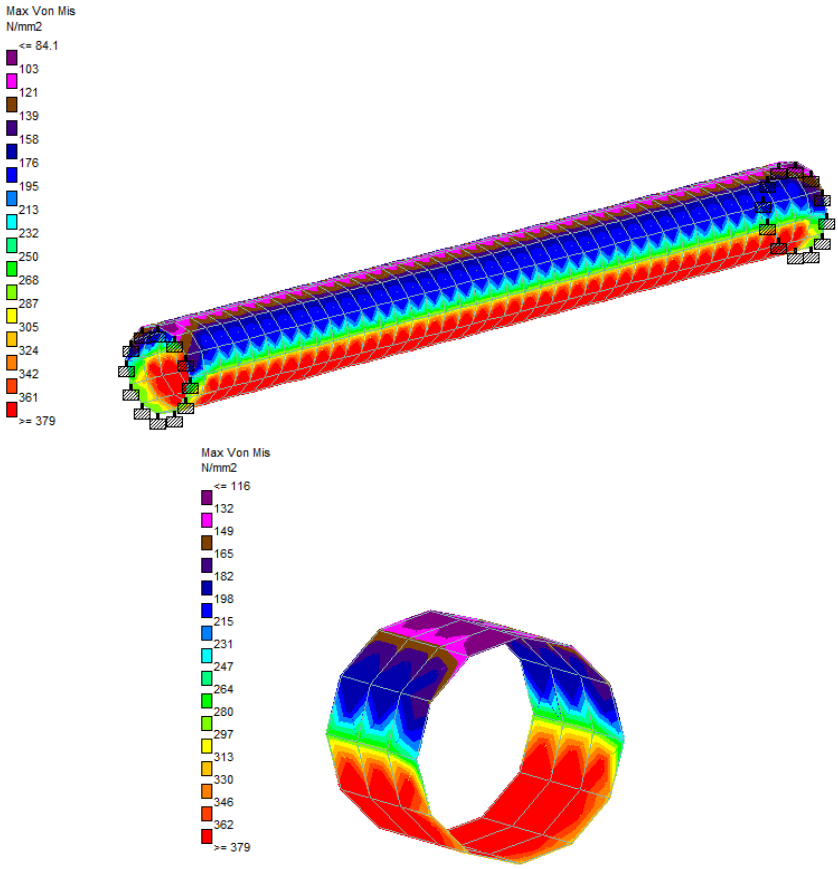

Fig. 3. Evaluation of stress limit generated in pipeline elements.

According to the selected load combination, the colour diagram shows the increase of the yield stress from top to bottom according to the model.

The structural model of the pipe was modelled in the STAAD.Pro software, and analysed taking into account the metal weight and the working pressure generated in the pipe. Since the yield strength on the bottom of the pipeline (379 MPa) is greater than the yield strength (350 MPa) corresponding to the physical properties of the metal, the resulting stress in the pipe is greater than the allowable stress.

4. CONCLUSION

- Defectoscopy was carried out with an OLYMPUS 27 MG ultrasonic thickness gauge on the 187.74th km section of the underground main gas pipeline "Astara-Gazimammad" of the "Gas Export" Department (SOCAR, Azerbaijan).

During the monitoring process, measurements were taken on the surface of the pipeline in the annular direction, and it was determined that the actual wall thicknesses were 12.18 mm on the top surface of the pipe, 11.80 mm on the side surface, and 9.19 mm on the bottom surface. Since corrosion pits sized 5÷6 mm were found on the bottom surface of the pipe, the actual value of the thickness in this part turned out to be 3.19 mm.

- By comparing the estimated thickness of the pipeline by mathematical calculation with the actual thickness (3.19 < 4.60), it was concluded that the pipeline was unsuitable for operation.
- The structural model of the pipeline was modelled in STAAD.Pro software and analysed taking into account the metal weight and the operating pressure generated in the pipeline. Since the yield stress (379 MPa) is greater than the stress corresponding to the physical properties of the metal (350 MPa), the resulting stress in the pipe is determined to be in excess of the allowable stress limit.

REFERENCES

1. Sachedina, K., & Mohany, A. (2018). A Review of Pipeline Monitoring and Periodic Inspection Methods. *Pipeline Science and Technology, 2* (3), 187–203. DOI: 10.28999/2514-541X-2018-2-3-187-203
2. Witek, M., Batura, A., Orynyak, I., & Borodii, M. (2018). An Integrated Risk Assessment of Onshore Gas Transmission Pipelines Based on Defect Population. *Eng. Struct., 173*, 150–165. DOI: 10.1016/j.engstruct.2018.06.092
3. Witek, M. (2018). Validation of In-Line Inspection Data Quality and Impact on Steel Pipeline Diagnostic Intervals. *Journal of Natural Gas Science and Engineering, 56*, 121–133. DOI: 10.1016/j.jngse.2018.05.036
4. ASME Code for Pressure Piping, B31. (2016). *Process Piping.* The American Society of Mechanical Engineers.
5. Flare Details for Petroleum petrochemical and Natural Gas Industries. (2020). American Petroleum Institute.
6. Pinheiro, B. C., & Pasqualino, I. P. (2008). Stress Concentration Factors of Longitudinal and Transverse Plain Dents on Steel Pipelines. In *Proceedings of the ASME 2008 27th International Conference on Offshore Mechanics and Arctic Engineering*. *Volume 3: Pipeline and Riser Technology; Ocean Space Utilization* (pp. 623–632). 15–20 June 2008, Estoril, Portugal. https://doi.org/10.1115/OMAE2008-57836
7. State Construction Norms of the Republic of Azerbaijan. (2009). *Design Norms of Main Pipelines (AzDTN 2.9-2).* Baku.
8. GOST 8731-74 Seamless hot-rolled steel pipes. (01/01/1976). *Technical Requirements*. Moscow.
9. SNiP 2.05.06-85 Main pipelines. (2011). Moscow.
10. TU 14-3-1573-96: Longitudinal electric-welded steel pipes with a diameter of 530-1020 mm with a wall thickness of up to 32 mm for main gas pipelines, oil pipelines and oil product pipelines. (1997). Moscow.
11. Amine, M., Seghier, B., Mourad, B., Elahmoune, B., & Gaceb, M. (2017). Probabilistic Approach Evaluates Reliability of Pipelines with Corrosion Defects. *Oil Gas J. 115,* 64–68.
12. Pesinis, K., & *Tee, K. F. (2017).* Statistical model and structural reliability analysis for onshore gas transmission pipelines. *Engineering Failure Analysis, 82*, 1–15. DOI: 10.1016/j.engfailanal.2017.08.008

sciendo

LATVIAN JOURNAL OF PHYSICS
AND TECHNICAL SCIENCES
2025, N 4

DOI: 10.2478/lpts-2025-0030

STRATEGIC DEVELOPMENT AREAS OF THE LATVIAN ROAD BUILDING INDUSTRY

K. Belovs[1], N. Kocanovs[2]*, R. Kocanova[2], I. Geipele[2], J. Naimaviciene[3]

[1] LLC "VIA",
5 Starta Str., Riga, LV-1026, LATVIA
[2] Riga Technical University,
Institute of Civil Engineering and Real Estate Economics,
6-210 Kalnciema Str., Riga, LV-1048, LATVIA
[3] Vilnius Gediminas Technical University
11 Saulėtekio al., Vilnius, LT-10223, LITHUANIA
*e-mail: nikita.kacanovs@rtu.lv

The article aims at evaluating the future development areas of the road building industry, analysing the road building development in Latvia, performing financial analysis of road building companies, and comparing the Latvian road building industry with other Baltic States.

National motor roads in Latvia are divided into three groups: state main roads, state regional roads, and state local roads. The article provides a theoretical review of the road building industry in Latvia, including the classification of national roads. The authors analyse the Latvian road building industry, its largest companies, and compare the Latvian road building industry with other Baltic States.

Areas of the road building industry in Latvia encompass different aspects, facilitating to improve the road infrastructure and its accessibility, ensuring an efficient and safe transport system, and promoting the development of the national economy. Road building and motor roads are very important for Latvia's national economy. This has been the case for decades. To facilitate the efficient operation of motor transport, which provides the basis for other industries in the national economy, it is necessary to maintain and develop the network of motor roads properly.

The road industry is closely connected to other industries, and, in the opinion of the authors, it fulfils the social function in the most direct way, as roads are used by residents and there is both synergy and cooperation between road networks and socioeconomic factors. Networks of national roads should also be evaluated in view of public interests – whether the roads ensure the well-being of residents and, hence, the development of the region.

Keywords: *Construction, infrastructure, motor roads, road construction.*

1. INTRODUCTION

The topicality of the selected theme of research is substantiated by the fact that road building is one of the most important infrastructure industries in any country. Roads ensure convenient and safe relocation for people and freight, promote economic growth and social development. The Latvian road building industry is currently in a difficult situation. The road infrastructure in Latvia has become obsolete, and significant investments are required for its renovation and development. However, the state budget capacity is not sufficient for such investments to ensure the road infrastructure development in accordance with modern requirements. Therefore, it is required to develop a strategy for ensuring the development of the road building industry and its competitiveness in the long-term perspective. The road building industry faces several challenges, including a lack of labour force, high costs, and big competition, as well as an unclear model of financing that encumbers the development of road building companies. To ensure the sustainable development of the industry, it is required to find solutions to these challenges.

Latvia has an open economy, and its growth is related to international trade. Good roads help to ensure that Latvian companies have convenient and safe access to the international market. Roads are significant for the development of entrepreneurship, as they allow reducing transport expenses and increasing production efficiency. Good roads help companies transport goods and services more conveniently, thereby reducing transportation expenses. It makes companies more competitive and promotes production growth. High quality of roads helps connect regions and promotes their economic development. It is especially important for Latvia, as it is a relatively large country with small towns and considerable distances between them. Regarding the attraction of investments, the condition of infrastructure is extremely important, as inappropriate infrastructure can complicate the process of attracting investments.

When performing road construction and renovation, a big emphasis is laid on the qualitatively developed technical project documentation, to reduce to a minimum unforeseen works at the project implementation stage, which could be anticipated at the project development stage [1].

Although motor roads are significant for the entire country, their technical condition raises considerable concern, being unsatisfactory and in some places even hazardous for users. Since 1991, the road construction deficit of several billion euros has been accumulated in Latvia – to liquidate the motor road repair deficit for the works that had to be performed at the time stipulated by the regulations, EUR 2.94 billion is required according to the 2023 prices [2].

Every year, the financing volume allocated for the construction of motor roads is twice less than required. In the situation when motor roads and bridges are renovated in due time and there is no repair deficit, the required financing for the national network of motor roads is EUR 648 million per year. In the event renovation of road pavement is not performed at the required time, constructive layers of motor roads lose their technical properties and cannot ensure the needed resilience for loads caused by transport, and, as a result, the fast collapse of motor roads takes place.

The significance of construction is

determined by its considerable proportion in the gross domestic product. Construction is a relatively labour-consuming process, and, on the state level, it attracts about half of all capital investments. Construction is related to any branch of the national economy, creating a base for it in the form of buildings and structures. Therefore, it is important for every country to develop a viable construction industry [3].

The construction industry plays a significant role in the Latvian national economy – its proportion in added value reaches 5.9 %; it employs 6.4 % of the entire labour force; its contribution to the Latvian budget is 2.3 % of all tax revenues [4]. A significant share of such revenues is directly related to the road construction industry.

To achieve positive progress in improving the Latvian network of motor roads, a number of measures need to be taken. It is important to manage the existing financial resources efficiently and create new opportunities to obtain additional financing for road projects in Latvia, follow innovations in the industry, and find opportunities for attracting new specialists. Reforms are required to ensure the sustainable development of the industry.

Sustainability and sustainable development could become an attractive slogan for a long-awaited solution in the strategic development of the road industry [5].

Every year, more roads are built all around the world, and a large part of them, which are to encounter high-intensity traffic, are asphalted. Such a process can be time- and resource-consuming; thus, it is important to ensure maximal longevity of the built construction and provide methods for improved architectural type and used material quality [6].

The article aims at analysing the road building development in Latvia, performing financial analysis of road building companies and comparing the Latvian road building industry with other Baltic States, making conclusions regarding the development of the road building industry in Latvia.

The following research methods have been used during the research: monographic or theoretical method, graphical method, statistical data analysis, descriptive analysis, comparative analysis – reflecting information in figures and tables. The research materials and data for analysing theoretical and factual sources have been mostly taken from the internet resources, scientific databases, and theoretical books, as determined by the availability of information. Limitations of the research are the availability of actual statistical data and information.

2. THEORETICAL ASPECTS OF STUDYING THE ROAD BUILDING INDUSTRY

Real estate, including motor roads, is one of the property types that gives benefit to its owner and often directly affects the environment, processes, and people. Not only safety and quality of the property is important, but also its landscape and aesthetic delight rendered to passers-by, tourists or users. Additionally, it also promotes the economic development [7].

According to Section 3 (3) of the Law on Roads, roads in Latvia are divided into:

- main roads connecting the national road network with the main road network of other countries and the capital city with other cities of the Republic of Latvia or bypass roads of cities of the Republic of Latvia;

- regional roads connecting the administrative centers of districts with each other or with the cities of the Republic or with the capital, or with the main or regional roads or with each other;
- local roads connecting the administrative centers of a county with the county towns, the populated areas of the county in which parish administrations are located, villages or other public roads, or between the administrative centers of individual counties [8].

Motor roads are complex engineering structures outside city boundaries, whose purpose is to ensure transportation for vehicles, whereas 'road' is a wider term, which includes also city streets. From the perspective of the user, motor roads and streets form a united network of roads, where traffic is regulated according to uniform rules, and, therefore, identical driving conditions should be provided on them. Roads can be classified according to their:

- administrative belonging (substantiating management and usage of roads);
- cross-section form (characterising the carrying capacity of the road);
- pavement type (characterising the physical and mechanical properties of the road structure);
- surfacing type (determining the driving comfort level and the road management strategy) [9].

Administratively, according to the property rights and management responsibility, the Latvian roads are divided into the following groups:

- state motor roads (main, first- and second-class motor roads);
- municipal roads (city streets and parish roads);
- forest roads (roads for state forest management);
- private roads (internal roads of commercial facilities and households) [9].

National motor roads in the territory of Latvia are a significant transport infrastructure, as they ensure important connection between cities and countries. According to the the Law on Roads, state motor roads include all road routes connecting Latvian motor road networks with main motor road networks of other countries or with the Latvian capital – Riga and other towns or town by-pass roads. These national roads are recognised on maps and other informative materials, as they are designated by the letter "A" and have a numbered sequence for their identification. Currently, Latvia has 15 state main roads, their designation, thus, being from A1 to A15 [8]. As an example, A1 main road can be mentioned, which connects Estonia with Lithuania, crossing the Latvian territory, as well as A7 main road from Riga to Lithuania, which goes through Bauska and other regions. State motor roads form a publicly available network of roads by which all traffic participants can move without restriction, except for cases when weight restrictions are set or road repairs take place. State motor roads are the property of the Republic of Latvia, and their management is entrusted to the Ministry of Transport, which is, in turn, delegated to the State Limited Liability Company "Latvijas Valsts ceļi" to conduct maintenance and management of roads.

When developing a motor road construction project, special attention should be devoted to materials, as they form a considerable part of the total construction costs. Therefore, specifications of road construction are significant, which include certain requirements for each separate construction case. At the beginning of each work specification, binding instructions can be provided to the construction performer, for example,

in cases when the construction project has no indications regarding the usage of the exact types of products stipulated in the project, etc.

When building motor roads, it must be taken into account that road surfacing consists of two parts: pavement and base. Pavement can be made of one, two, or three layers. The base consists of two layers – a carrying layer and an additional layer. In recent years, there have been increasing discussions about both the quality of materials and their effect on the environment.

For example, one of the used materials is bitumen. As stated by scientists from India, in the surrounding environment temperature, bitumen is solid and causes no threat to the environment, and human health. However, in the course of production/construction, it is heated, stored, transported, and used, thus, causing emission of different hydrocarbons [10]. It, therefore, raises questions about the real effect of bitumen on the environment and human health.

The supply of materials is very important, especially in road construction projects, as they are required in the daily construction process. Lack of materials is the main source of losses in the construction site productivity. This happens because the used material management methods lack structured communication and clearly defined tasks [11].

To achieve positive progress in improving the Latvian network of motor roads, the State should take different measures – it is significant to efficiently manage the available financial resources and create new opportunities for obtaining additional financing for motor road projects in Latvia, follow innovations in the industry, and find opportunities for attracting new specialists. Reforms are needed to ensure the sustainable development of the industry.

According to the available statistics, as of 31 December 2023, the total length of motor roads and streets registered in Latvia was 71 157 km. The average density of the road network is 1.102 km per 1 km^2. The total length of state motor roads administered by the State Limited Liability Company "Latvijas Valsts ceļi" is 19 895 km. The average density of the state road network is 0.308 km per 1 km^2. "Latvijas Valsts ceļi" administers 955 bridges, of which 891 are made of reinforced concrete, 16 of stone, 45 of iron, and 3 of wood. The total length of all bridges is 28 100 m (see Fig. 1) [12].

Table 1. Division of Motor Roads in Latvia [12]

Classification of Roads	**Length of roads as of 31 December 2023 (km)**			
	Black top	Crushed stone or gravelled	Unpaved	Total
National roads, incl.	9803	10 092	00	19895
Main roads (A)	1676	-	-	1676
Regional roads	4756	707	-	5463
Local roads (V)	3358	9326	-	12684
By-roads	13	59	-	72
Municipal roads and streets, incl.	6604	31423	-	38027
roads	1434	28034	-	29468
streets	5170	3389	-	8559
Forest roads	29	12119	1087	13235
Total roads and streets	16436	53634	1087	71157

The authors of the article, when analysing the classification of the Latvian motor road network, conclude that the proportion of this state motor road infrastructure is comparatively big, taking into account the country area and the number of residents. The relatively big area of Latvia, compared to the number of residents, requires a wide and efficient network of motor roads to ensure communication and access in the entire country. The distribution of Latvian residents in the territory can be comparatively scattered, thus making this aspect particularly important.

Therefore, it can be concluded that a network of motor roads is a major component of a viable and developed State. To efficiently serve residents and companies scattered throughout the entire territory of the country, motor roads should ensure not only fast and safe travelling between cities and towns but also access to rural areas. The development of such a network of motor roads not only promotes economic development and growth of business activities but also improves the quality of life, providing residents with convenient access to transport and communication.

3. ANALYSIS OF THE ROAD BUILDING INDUSTRY IN LATVIA

The number of companies operating in the Latvian road building industry has increased over time. As of the end of 2023, 378 companies have been operating in Latvia under the NACE code 42.11, which is the construction of roads and main motor roads, without account of bridge and railroad construction companies, the total number of which is 21 [13]. Thus, in total, 399 companies are involved in the construction of vehicle roads in Latvia. However, most of these companies are small.

When investigating the technical condition of Latvian motor roads, it can be concluded that the road condition is improving with every year, as of the end of 2022, 78.3 % of state main roads and 57.5 % of state regional roads with asphalt concrete pavement were in a good or very good technical condition. This is the best indicator over the past 30 years. Since 2005, the volume of roads in a good or very good technical condition has not only doubled, but has increased more than twice, from 32 % to 78.3 % in the main road segment and from 22 % to 57.5 % in the regional road segment [12].

As of 15 April 2024, a total of 32 construction objects have been registered. Out of 36 Latvian regions, construction is being conducted in 19 (Table 2) [12]. Generally, regions with just one construction object dominate, whereas Cesis Region differs from all others by having construction at four objects.

To perform a more detailed analysis regarding the development of the road building industry in Latvia, the authors have selected six big road building companies in order to get a better understanding of the industry development tendencies in the country.

The authors of the article have selected the following companies:

- Road building firm “BINDERS”;
- Joint Stock Company “A.C.B.”;
- Limited Liability Company “TILTS”;
- State Joint Stock Company “Latvijas autoceļu uzturētājs”;
- Limited Liability Company “VIA”;
- Limited Liability Company “SC GRUPA”.

Table 2. The Current List of Construction Objects in Latvia as of 15 April 2024 [12]

Number of Objects	**4**	**3**	**2**	**1**
Regions	Cesis Region	Dobele Region	Gulbene Region	Marupe Region
		Aluksne Region	South Kurzeme Region	Limbazi Region
			Ogre Region	Smiltene Region
			Jekabpils Region	Kuldiga Region
			Jelgava Region	Ventspils Region
			Valka Region	Ludza Region
			Tukums Region	Rezekne Region
			Talsi Region	Preili Region

To analyse the position of the selected companies, the authors have performed their financial analysis.

During the period from 2019 to 2022, the net turnover of the road building firm LLC "BINDERS" decreased from EUR 107 million to EUR 86 million. During the reporting year, profits or losses were fluctuating. In 2022 and 2021, losses were observed of EUR 2.8 million and EUR 345 thousand, correspondingly. Loss and profit fluctuated in a cyclical manner, which might be related to the specific features of the industry or the company.

During the period from 2018 to 2022, net turnover of JSC "A.C.B." increased from EUR 93 million to EUR 105 million. The increase is observed every year, except for 2021, indicating the company's growth. When comparing 2021 with 2022, its net turnover increased considerably – by EUR 31 million. The net turnover increase indicates the company's successful growth and potential on the market. During the reporting year, profits or losses were fluctuating, but, in general, a positive tendency was observed.

The net turnover of JSC "Latvijas autoceļu uzturētājs" was fluctuating, but, in general, remained comparatively stable. In 2022, the company's net turnover slightly decreased, comparing with the previous year, by EUR 6.6 million. During the reporting year, its profit decreased considerably from EUR 3.9 million in 2021 to EUR 1 361 in 2022, indicating challenges or changes in the company's operation.

The net turnover of LLC "VIA" remained stable during the period from 2018 to 2021, when it increased from EUR 17.5 million to EUR 21.6 million. Comparing 2021 with 2022, the company's net turnover increased by about EUR 2 million. It remained on a stable level, which indicated that the company maintained a balanced business volume. During the reporting year, its profit was fluctuating; however, a positive change took place from 2021 to 2022. Profit of the reporting year increased considerably in 2022, which could be the result of a more efficient operation or other factors of success. In 2020, the company had a loss of EUR 506 thousand. In the previous years, there were fluctuations of profit and loss, which could be influenced by different factors or change of the company's strategy.

LLC "SC GRUPA" experienced losses in 2022 and 2021, which was a noticeable contrast to the profit growth in previous years – from 2018 to 2020. LLC "SC GRUPA" explained the caused losses in its management report with fast growing costs. On 24 February of the reporting year, Russia started its brutal invasion into Ukraine, which caused a fast and uncontrolled growth of costs for practically all

resources required for road building: bitumen, fuel, and gas. The growth of prices for these resources, in its turn, caused a fast growth of costs for transport and construction equipment services, mineral materials, etc. [13].

In the opinion of the authors, turnover and profit are two important indicators that allow making different conclusions about the financial situation and operation of construction companies. The authors reckon that a high turnover indicates that a company sells its products or services on the market successfully. A higher turnover can be evidence of the fact that a company efficiently manages its resources and enjoys demand in the industry, as well as high turnover can indicate that a company is competitive and occupies a stable position on the market. The profit level with regards to the turnover (profitability) is an important indicator of a company's efficiency. A high profitability indicator demonstrates a company's capability to obtain profit from its investments. A stable profit can indicate financial stability and sustainability of a company. A high level of profit allows a company to make investments, develop, and continue investing in the future.

In general, high turnover and profit indicate that a construction company is successful on the market, can ensure the demand for services or products and has financially stable activities. However, it is important to consider other indicators and factors as well, for example, the structure of expenses, liabilities, and the market situation, in order to make a more complete analysis of a company.

The conclusion of the authors that big road building companies operate with a small profit may encompass several important aspects and conclusions. The road building industry has high competition, which leads to low profit indicators. To retain their market position, big companies can be forced to offer competitive prices that can limit the received profit. To increase the profit level, it might be required for companies to improve the efficiency and mechanisms of their operation, to reduce expenses. This may include a technological innovation, a more efficient project management, or optimisation of resources. Big road building companies can be sensitive to economic cycles; the authors conclude that profit can decrease during downturn periods and increase during boom periods.

Loss of profit from the operation of a road building company can be the result of different factors and conditions. A company can operate at a loss, as there is intense competition and a demand for low prices in the road building industry. If a company is forced to offer prices that do not cover its operational expenses, this can lead to a loss of profit. Losses can result from the incomplete or poor management of a project. Incorrect budget planning, inappropriate coordination of resources, or project delay can increase expenses and reduce profit. A company can also face a loss of profit in the event of an unforeseen increase in expenses for materials or labour force. Growing prices for raw materials or unforeseen labour force issues can influence the budget stability considerably. If a company manages the risks involved in certain construction projects inefficiently, it can cause additional costs and losses. Unforeseen circumstances, for example, idle standing or acts of nature, can increase project costs.

In its turn, a company that does not invest sufficient funds in new technologies and improvements can lose efficiency and competitiveness, which leads to a reduction in profit. If a company is unable to adjust to new regulatory requirements, amendments thereto, or industry innovations, it may incur additional expenses and experience a negative impact on its profits.

When studying big road building companies, the authors conclude that all of them have been engaged in road construction for over 20 years. Big road building companies usually have a sufficient and qualified labour force, which allows them to offer different road construction services. Large companies usually participate in several big road construction projects simultaneously and enter into extensive long-term agreements with state or municipal authorities. In the course of time, to increase their competitiveness, the companies continue developing their operation types and get engaged also in the production of materials, as well as follow modern technological tendencies. It has to be noted that the aforementioned road building companies are among the biggest employers in the construction industry in Latvia – SJSC "Latvijas autoceļu uzturētājs" occupies the first position, the road building firm "BINDERS" – the third, LLC "TILTS" – the fifth, JSC "A.C.B." – the sixth, LLC "SC GRUPA" – the 35th and LLC "VIA" – the 42nd [13].

It can be concluded that SJCS "Latvijas autoceļu uzturētājs" dominates in the industry, as the company occupies the first position and, most probably, plays a significant role in road maintenance and promotion of the industry development in Latvia. This indicates that this company can be the main participant in the maintenance and development of the state road infrastructure. Large road building companies, for instance, LLC "BINDERS", JSC "A.C.B.", and LLC "TILTS", might be ensuring a significant part of jobs in the construction industry. Thus, these companies not only can perform significant construction projects but also create jobs. Alongside with big companies, the list also contains smaller participants, for example, LLC "SC GRUPA" and LLC "VIA", which occupy the 35th and the 42nd positions. It demonstrates that there is competition in the construction industry and opportunities for small companies to participate in and perform construction projects. When reviewing the list of companies, it appears that the industry is active and diverse. It can indicate that there is a significant interest and demand in Latvia for road building services that stimulate competition and innovations. The road building industry in Latvia is a dynamic and important constituent of the national economy, where big companies dominate, but smaller participants are involved as well, creating jobs and promoting the development of the industry.

Road building is the national economy industry that influences every Latvian resident, as each of us uses roads to travel from one point to another, conducting important activities, for example, transportation of goods. A well-arranged infrastructure is a significant precondition for the attraction of investments and the growth of the national economy. Investment projects are conducted in places where convenient and high-quality roads are available. Although the total Latvian road network coverage is sufficient, the technical condition of the roads is not acceptable and does not meet the needs for safe and continuous transportation. In comparison with neighbouring countries, the current condition of Latvian motor roads is the worst. For example, in 2020, 15.60 % of blacktop roads were evaluated as 'very bad'. The situation has improved in recent years, but not in a sufficient volume (see Table 3). Such a situation has remained on Latvian motor roads for several years, as every year insufficient financing is invested in the road building industry. This bad situation with the roads is also related to the big construction deficit in the road building industry, which constitutes EUR 2.94 billion.

One must think about the necessity to

develop qualitative result indicators that could be used to evaluate technical parameters and sustainability of materials used in construction [14].

The main problems of the network of motor roads are related to the road pavement and carrying capacity of bridges – roads were built in the 1960s and up to the 1980s in accordance with the standards valid at that time, which set the maximum motor transport axle load of 10 t and the maximum gross vehicle weight of 36 t. Today the market needs and the European requirements set 11.5 t and 44 t, correspondingly. As a result, in some sections, there is the situation when quality of the motor roads cannot be ensured by applying simple repair methods.

Table 3. Technical Condition of Blacktop Roads Inspected by "Latvijas Valsts ceļi"

Technical Condition of Black Top Roads				
Technical Condition	2017	2018	2019	2020
Very good	14.80 %	16.60 %	21.50 %	25.60 %
Good	21.80 %	22.70 %	21.30 %	25.10 %
Satisfactory	20.60 %	21.40 %	20.20 %	18.60 %
Bad	19.20 %	17.60 %	18.30 %	15.10 %
Very bad	23.60 %	21.70 %	18.70 %	15.60 %
In total, %	**100.00 %**	**100.00 %**	**100.00 %**	**100.0 %**

These data demonstrate that the condition of roads has improved in recent years, as, comparing 2017 with 2020, the number of state roads whose technical condition is evaluated as 'very good' has increased by 10.80 %. The number of state roads whose technical condition is evaluated as 'very bad' has decreased by 8 %, when comparing 2017 with 2020.

Table 4. Technical Condition of Gravelled Roads Inspected by "Latvijas Valsts ceļi"

Technical Condition of Gravelled Roads				
Technical Condition	2017	2018	2019	2020
Good	9.20 %	6.20 %	6.20 %	6.70 %
Satisfactory	48.40 %	47.40 %	42.60 %	37.40 %
Bad	42.40 %	46.40 %	51.20 %	55.90 %
In total	**100.00 %**	**100.00 %**	**100.00 %**	**100.00 %**

More than half of the gravelled roads supervised by Latvijas Valsts ceļi are evaluated as being in a bad condition in 2020 (see Table 4). Whereas roads the condition of which is satisfactory form 37.40 % of the road network. When analysing the statistics, it can be concluded that Latvian gravelled roads are in a bad condition.

Local gravelled roads, which are mostly within the territory of the country, are least loaded. In the recent decade, minimal investments have been allocated for these roads and, as a result, the condition of gravelled roads is improving very slowly. In 2022, only 18.5 % of regional gravelled roads and 8.9 % of local gravelled roads were in a good or very good technical condition. A lot of the local state roads do not perform

the function of state motor roads anymore and about 4 000 kilometres of roads should be transferred to municipalities [15]. It is also significant to ensure continuous and qualitative road maintenance, being quite a wide spectrum of activities, which includes different road operation processes with very specific functions and tasks [16].

The load of roads in Latvia is influenced by several factors, including:

1. density of population, economic activities;
2. economic factors, which encompass activities of merchants and different companies;
3. transport flow, which differs with account of both the road classification and the usage of roads, either as local or international significance roads;
4. quality and accessibility of roads – the higher the road quality and accessibility, the bigger the traffic and, thus, also the load.
5. road infrastructure development – more attention is devoted to the road development, the higher the road load, attracting a bigger flow of transport.

When developing the road infrastructure, improvement, renovation, widening, and modernisation of the existing roads are set as the goal, providing a safe and efficient transport flow in the country.

4. COMPARISON OF THE ROAD BUILDING INDUSTRY IN THE BALTIC STATES

Latvia has been increasingly more compared with Lithuania and Estonia in different contexts, for example, with regards to differences in the road tax amount, compared with Lithuania, or introducing a beverage packaging deposit system as in Estonia. However, the condition and financing of roads are also aspects to be considered when comparing the Baltic States. Latvia's results in this connection do not provide a favourable comparison with those of other Baltic States.

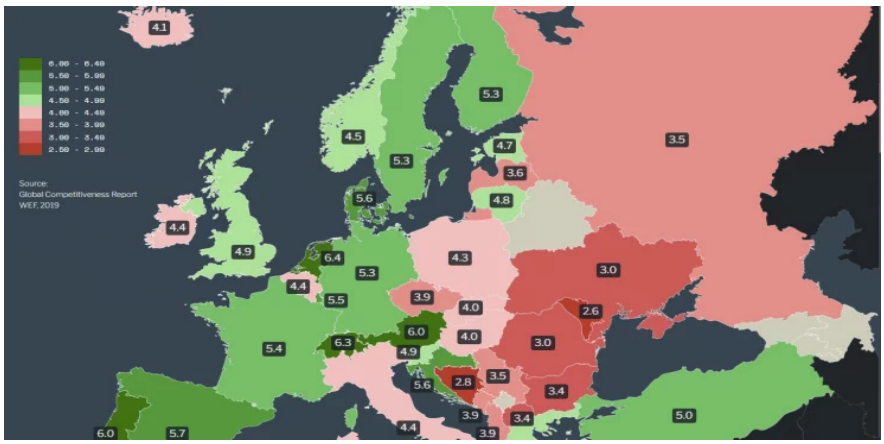

Fig. 1. Road quality in Europe: The best and the worst roads in Europe [17].

People were given the opportunity to evaluate from 1 (extremely bad – among the worst in the world) to 7 (extremely good – among the best in the world).

Although the general tendency is observable (Eastern Europe has, on average, worse indicators than Western Europe and the Nordic countries), there are some deviations. For example, Belgium has much worse roads than its neighbours. This contrast is even stronger, since the Netherlands has the best road quality in Europe (6.4 points, compared to 4.4 of Belgium). Certainly, it also provokes jokes on the part of the Dutch with regards to their neighbours, saying that the difference between the roads in the Netherlands and Belgium can be not only seen, but also felt and heard (see Fig. 1) [17].

The European average indicator is 4.8 points, calculated using the mean value from evaluations of roads across all countries. This evaluation is based on the World Economic Forum's polling, where a scale of 1 to 7 was used. One on this scale means that the road condition is extremely bad among all roads in the world, but 7 means that the road condition is extremely good and is among the best roads in the world [17]. Evaluation of the quality of Latvian roads is one of the lowest in Europe, being 3.6, which means that road quality in Latvia is considered poor, as the evaluation of Latvian roads lags the EU average by 1.2 points. In the context of the Baltic States, the situation is not much better, as also here Latvia gets the lowest evaluation from all Baltic States (see Fig. 1). Taking into account the fact that the length of state roads in Latvia is 20 020 km, in Lithuania 21 203 km and in Estonia 16 969 km (see Fig. 2), the road condition in Lithuania and Estonia is very close to the European average, in contrast to Latvia. The Estonian evaluation is 4.7, lagging behind the European average only by 0.1 points, which means that the state roads are evaluated as satisfactory. Whereas, Lithuania is evaluated with 4.8 points, which is the average indicator in Europe.

Thus, the authors conclude that it is clearly seen that the worst quality of roads in the Baltic States is exactly in Latvia.

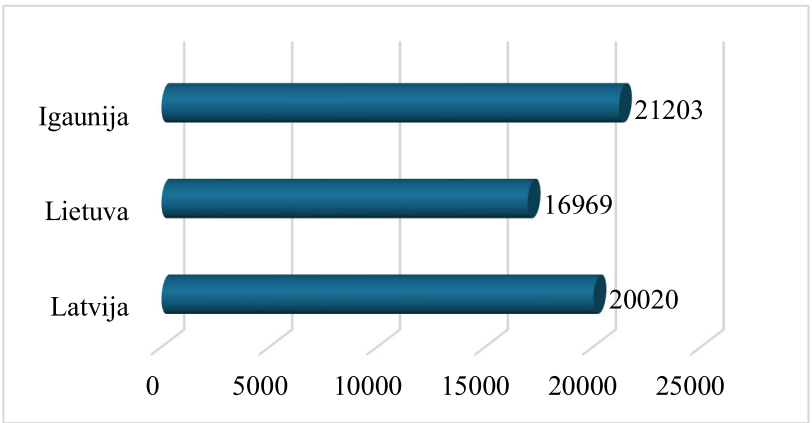

Fig. 2. Financing for state motor roads in the Baltic States in 2023 [18].

Comparing financing for state roads in the Baltic States, it can be concluded that in 2023, Estonia had the smallest financing, whereas Lithuania – the biggest. The state budget for Latvia was EUR 221 million, which was by EUR 69 million more than in Estonia, but by EUR 143 million less than in Lithuania. The EU financing (CF, ERDF, etc.) for Lithuania was the highest – EUR 91 million, which was by EUR 35 million

more than for Estonia and by EUR 76 million more than for Latvia. An important factor to be mentioned is that in 2023, Latvia did not have the European infrastructure connection tools financing, for Estonia it was EUR 15.3 million and for Lithuania – EUR 55.3 million [18]. It can be concluded that differences in financing between the Baltic States indicates different priorities and challenges in the development of state roads. Every country must consider how to optimise its financial resources in order to ensure the efficient and sustainable development of the road infrastructure.

Comparing the 2022 budgets, it can be concluded that Estonia had the smallest financing, whereas Lithuania had the biggest also in 2022. The total Latvian financing for roads was EUR 313 million, in Estonia – EUR 228 million, and in Lithuania – EUR 582 million [2].

It is stated that road construction in Latvia is one of the most expensive in the Baltic States, but such a statement lacks a precise definition with regard to what road construction costs are compared – whether these are costs per kilometre, or design costs, or maintenance costs. Construction costs are hard to be compared, as every road is a unique structure with different composition, usage of materials, applied technologies and methods. These factors, as well as costs of materials and complex technologies, can influence construction costs considerably. Costs of materials in Latvia are higher than elsewhere in the Baltic States, and it is logical with account of the limited natural resources and accessibility of construction materials in this country. As an example, dolomite rock can be mentioned, which is used for groundwork base and asphalting. This rock is less durable in Latvia, comparing to Estonia and Lithuania, which means that it is practically not used in Latvia, especially in the construction of state roads, but rather for insignificant motor road projects. Whereas dolomite rock extracted in Estonia and Lithuania can be used wider, as it has good durability. Due to this reason, when repairing state motor roads in Latvia, it is required to import such materials from other countries, increasing transport costs and total costs of materials.

A similar situation is also with granite rock, which Latvian entrepreneurs obtain from Sweden, Norway and Lithuania, as such type of rock is not available in Latvia. This increases construction costs, as, in addition to costs of materials, transport costs must also be included. Whereas, Estonians obtain this material from Finland, as they also do not have it available.

However, when speaking about bitumen, which is used in the production of bituminous concrete, it is not manufactured in Latvia and, thus, needs to be imported, which increases the total costs of materials. It is also worth indicating that Estonia and Lithuania have plants where bitumen is produced for such usage.

Thus, the authors conclude that road construction in Latvia costs more than in other Baltic States, as Estonia and Lithuania have more resources available.

5. CONCLUSIONS

The road building industry is a significant branch of the Latvian national economy, which affects every resident, as roads are used for all purposes – from travels from point A to point B to information exchange. A well-maintained infrastructure is an important precondition for attracting investments and promoting the growth of

the national economy. Investment projects are selected at places where qualitative roads are available. In general, the Latvian road network is spread sufficiently, but its current condition does not meet the requirements of safe and continuous traffic.

In Latvia, the road building industry is especially significant and growing, as, in order to promote the national economic growth, improve the life quality of residents and ensure that Latvian international motor roads comply with the standards of the European motor road network, it is required to maintain and develop the motor road infrastructure efficiently.

To achieve a positive progress in improving the Latvian road network, the State should take different measures; it is significant to manage efficiently the available financial resources and establish new opportunities for obtaining additional financing for motor road projects in Latvia, follow the industry innovations, and find opportunities for attracting new specialists to the industry. Reforms are needed to ensure the sustainable development of the industry.

When investing in the road infrastructure development, new roads are constructed, existing ones are modernised, by implementing safety measures in road design, improvement of the construction standards, road lighting, etc. The infrastructure development also includes environment protection measures by using environmentally friendly materials and promoting the usage of sustainable transport solutions.

Overall, all measures implemented in road construction and its infrastructure development form a significant element in promoting the national economy and well-being of the population by ensuring a safe and efficient transport system.

REFERENCES

1. Upītis, M., Amoliņa, I., Geipele, I., & Zeltiņš, N. (2020). Measures to Achieve the Energy Efficiency Improvement Targets in the Multiapartment Residential Sector. Latvian Journal of Physics and Technical Sciences, *57* (6), 40–52. DOI:10.2478/lpts-2020-0032
2. Latvijas Valsts ceļi. (2023). *Valsts autoceļu tīkla 2020. gada statistika*. [*National Road Network Statistics 2020*]. Available at: https://lvceli.lv/celu-tikls/buvnieciba-un-uzturesana/celu-klasifikacija/
3. Lūce, I., & Amoliņa, I. (2019). Competence of local government building board in elimination of the consequences of arbitrary construction. In: IOP Conference Series: Materials Science and Engineering (vol. 660): 4th International Conference on Innovative Materials, Structures and Technologies (IMST 2019). 25–27 September 2019, Riga, Latvia. Bristol: IOP Publishing, Article number 012044. DOI:10.1088/1757-899X/660/1/012044
4. Latvijas Būvuzņēmēju apvienība. (2023). *Būvniecības nozares rādītāji*. Available at: https://www.latvijasbuvnieki.lv/statistika/
5. Cimbale, A., Amoliņa, I., Geipele, I., & Zeltiņš, N. (2023). Analysis and Implementation of Energy Efficiency Measures in Multi-Apartment buildings in Latvia. Latvian Journal of Physics and Technical Sciences, *60* (5), 56–72. DOI:10.2478/lpts-2023-0031
6. Braunfelds, J., Seņkāns, U., Šķēls, P., Poriņš, J., Haritonovs, V., Spolītis, S., & Bobrovs, V. (2023). Development of the strain measurement calibration technique for road pavement structural health monitoring applications using optical FBG sensors. In 2023 Photonics & Electromagnetics Research Symposium (PIERS 2023): Proceedings (pp. 1060–1065). 3–6 July 2023, Prague, Czech Republic. Piscataway: IEEE. DOI:10.1109/PIERS59004.2023.10221310

7. Puķīte, I., Zīra, M., & Geipele, I. (2019). Identification and monitoring of degraded real estate in the context of urban environmental analysis and development planning in the city of Riga. In The 4th International Conference on Innovative Materials, Structures and Technologies (IMST 2019): Book of Abstracts (pp. 70–70). 25–27 September 2019, Riga, Latvia.
8. Supreme Council. (1992). *On Motor Roads*. Reporter of the Supreme Council and Government of the Republic of Latvia. Available at: https://likumi.lv/ta/id/65363-par-autoceliem
9. Jeļisejevs, B. (2006). *Ceļu būves un ceļu uzturēšanas darbu organizācija un tehnoloģija*. [*Organisation and Technology of Road Construction and Maintenance Work*]. Textbook. Rīga: RTU izdevniecība.
10. Sippy, K. C., Sangita, S., Anuradha, S., & Gangopadhyay, S. (2010.) Recent Trends of the Emission Characteristics from the Road Construction Industry. *Environ. Sci. Pollut. Res. Int., 17* (9), 1493–501.
11. Awaad, S. Mansour, D., Mahdi, I., & Abdelrasheed, I. (2024). Impact of Material Supply Chain on the Productivity Optimization for the Construction of Roads Projects. *Nature Research, 14* (1), 3294
12. Latvijas Valsts ceļi. (n.d.) *Aktuālo būvobjektu saraksts. [List of Current Construction Sites]*. Available at: https://lvceli.lv/celu-tikls/buvnieciba-un-uzturesana/aktualo-buvobjektu-saraksts/
13. Lursoft. (n.d.) Nozare pēc NACE koda [*Sector by NACE Code*]. Available at: https://nace.lursoft.lv/42.1/celu-un-dzelzcelubuvnieciba?vr=3&old=0
14. Geipele, I., Puķīte, I., & Kauškale, L. (2016). Importance of business incubators for new business and its development in Latvia. In Proceedings of the 2016 International Conference on Industrial Engineering and Operations Management (pp. 1199–1206). 8–10 March, 2016, Malaysia, Kuala Lumpur. [S.l.]: IEOM Society.
15. Latvijas Valsts ceļi. (2023). *Valsts asfaltēto ceļu stāvoklis ir labākais pēdējo 30 gadu laikā [The Country's Asphalted Roads Are in the Best Condition for 30 Years]*. Available at: https://lvceli.lv/aktuali/valsts-asfalteto-celu-stavoklis-ir-labakais-pedejo-30-gadu-laika/
16. Amoliņa, I., & Geipele, I. (2017). Different approaches to building management and maintenance meaning explanation. In: Procedia Engineering, (pp. 905–912). 26–27 May 2016, Lithuania, Vilnius. Germany: Elsevier. DOI:10.1016/j.proeng.2017.02.099
17. Cipan, V. (2022). *Road Quality in Europe: The Best and Worst Roads in Europe*. IOP Publishing Ltd. Available at: https://viborc.com/road-quality-in-europe-the-best-and-worst-roads-in-europe/
18. Autoceļu avīze. (Spring, 2023). *Kaimiņvalstīs krasas atšķirības finansējumā valsts autoceļiem*. [In Neighbouring Countries, Funding for National Roads Varies Dramatically.] Latvijas Valsts ceļi. Available at: https://lvceli.lv/wp-content/uploads/2023/03/AA-pavasaris-2023-nonprint.pdf

sciendo

LATVIAN JOURNAL OF PHYSICS
AND TECHNICAL SCIENCES
2025, N 4

DOI: 10.2478/lpts-2025-0031

USING CHALK INSTEAD OF PAINTS IN PAPER PLASTER

N. Nutt, L. Nei*, M. Olle

Tallinn University of Technology,
School of Engineering, Tartu College,
Puiestee 78, 51008 Tartu, ESTONIA
*e-mail: lembit.nei@taltech.ee

Instead of using paint, it is possible to manufacture white paper plaster by adding chalk to its ingredients. The moisture buffer values (MBVs) of paper plaster mixtures with chalk ranged from 1.8 to 2.9. The higher the chalk content was, the lower the MBV of the paper plaster was. Only the mix with the highest chalk content, where the percentage of chalk was 90, had a moisture buffering capacity below 2.0, i.e., not excellent (MBV > 2.0).

Keywords: *Chalk, moisture buffer value, Nordtest, paper plaster*, *recycling, wastepaper.*

1. INTRODUCTION

Plaster is defined as a combination of binder, aggregate, and water [1]. An intelligent use of hygroscopic plaster components may enhance the interior climate and occupant comfort by minimising indoor humidity changes. Due to these reasons, there is a strong interest in defining the moisture transmission and buffering capabilities of porous building materials [2]. Covering the surface of a plaster with paint may significantly reduce the moisture capacity of the systems [3]. In this paper, we concentrate on paper plaster modified with the addition of chalk, aiming to obtain a white colour without using white paint. It has been shown that paper plasters perform excellent moisture buffering capacities [4]. The current study is to determine the impact of different proportions of chalk on the moisture buffer values (MBVs) of paper plaster.

Recycling of different waste materials is of utmost importance [5]−[8]. In the recent period, the landfilling of organic wastes has been prohibited in several countries [5]. The demand for looking novel pathways to reuse waste materials, including wastepaper, rises rapidly, as the circular economy and recycling become more and more important [6], [9]. At the same time, it should be kept in mind that in the case of covering finishing

materials (as plasters) with less permeable coats, the moisture buffering capacity of different materials decreases remarkably and leads to the increased amplitude of daily indoor relative humidity [10].

Wastepaper is among the materials that can be recycled through the production of different building materials [11]. For example, the effect of incorporating cellulose fibers from waste paper recycling into cement mortar was studied by Stevulova et al. [12]. The results of a recent study showed that paper plaster is applicable as an interior finishing material, as it does not turn mouldy in the environment typically favourable to moulds [13].

The MBV of paper plaster is inhibited when covered with paint [14]. The aim of this study is to specify the impact of chalk on the MBV of paper plaster, and the quantity of chalk that has to be added so that the plaster becomes sufficiently white and, as a result of this, does not need additional painting.

2. MATERIALS AND METHODS

The methodology utilised in this study is described in great detail by Rode et al. [15] and follows the lines presented in [14]. The Nordtest methodology defines a test protocol for experimental determination of the moisture buffer value *via* climatic chamber tests, where a specimen is subjected to environmental changes that come as a square wave in diurnal cycles [15]. It aims providing relative humidity (RH) variations of 75 % during 8h and 33 % during 16h. A partially sealed sample is subjected to repeated fluctuations in ambient relative humidity, while the temperature remains unchanged at 23 °C. The change in relative humidity (RH) causes the variation on specimen's weight, and this change is evaluated by periodic weighing. The weight change over time may be interpreted as an expression of the test specimen's MBV.

The specimens were made in three identical by composition copies according to the recipes that contain the components and/or additives given in Table 1. The plaster samples were prepared using wastepaper (newspaper), glue (Metylan Universal Premium, manufacturer Henkel) and chalk (powder). Chalk was added in different amounts (0–90 % of the total weight).

Table 1. The Composition of Plaster Samples (Ratio of Paper and Chalk by Weight)

Plaster group	**Paper/chalk ratio**	**Density, g/cm^3**
1	100/0	0.22
2	90/10	0.24
3	80/20	0.27
4	70/30	0.31
5	60/40	0.39
6	50/50	0.42
7	40/60	0.61
8	30/70	0.74
9	20/80	1.08
10	10/90	1.15

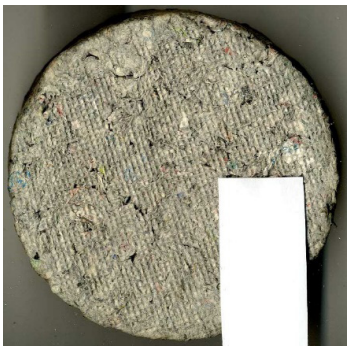

Plaster group 1

Plaster group 2

Plaster group 3

Plaster group 4

Plaster group 5

Plaster group 6

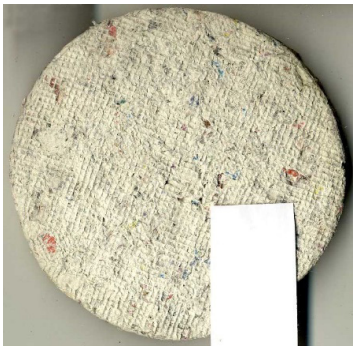

Plaster group 7

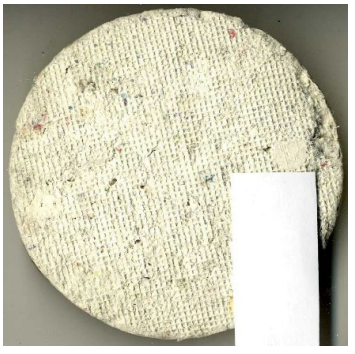

Plaster group 8

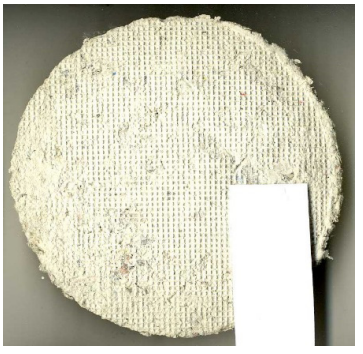

Plaster group 9

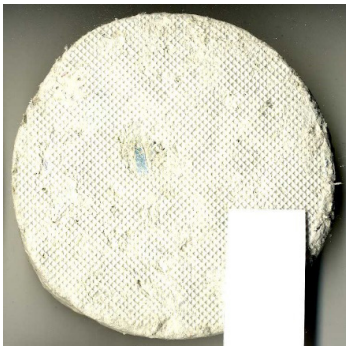

Plaster group 10

Fig. 1. Examples of specimen.

The paper was soaked in water for about 24 hours (ratio: 1 kilogram of paper and 30 L of water). The extra water (approximately 20 L) was then drained. Glue (40 g per 1 kg paper) and chalk (in 9 different amounts) were applied to the resulting paper pulps. The saturated and mushy paper was crushed by hand. Metylan Universal Premium adhesive powder, modified wallpaper glue produced from starch and including anti-fungal ingredients, was dissolved to form the glue. Paper pulp was added to the glue. A mold with a height of 2.5 cm and a diameter of 12.0 cm was used to make the test specimens. The test pieces were dried for 2 weeks at a room temperature (20−23 °C). The area needed to calculate the MBV was measured from the dried specimens. A total of 10 different mixtures were prepared (samples of them are shown in Fig. 1), three test specimens from each mixture.

3. RESULTS

The moisture buffering capacity of the mixtures tested in the experiment ranged from 1.75 to 2.89 (Table 2, Fig. 1). Only the mixture with the highest chalk content, where the ratio of chalk paper was 90/10, had a moisture buffering capacity of less than 2.0, i.e., not excellent (MBV > 2.0). The results of the tests show that the addition of chalk reduces the moisture buffering capacity of paper plaster. Figure 2 indicates that there is a linear relationship between plaster density and MBV.

Tabel 2. The MBV for Paper Plasters

Plaster sample	Paper/chalk ratio	*$MBV_{8/16h,}$ g/(m^2 %RH)	
1	Paper 100/0	2.9	excellent
2	Paper 90/10	2.8	excellent
3	Paper 80/20	2.9	excellent
4	Paper 70/30	2.7	excellent
5	Paper 60/40	2.9	excellent
6	Paper 50/50	2.7	excellent
7	Paper 40/60	2.8	excellent
8	Paper 30/70	2.4	excellent
9	Paper 20/80	2.1	excellent
10	Paper 10/90	1.8	good

*negligible (0−0.2), limited (0.2−0.5), moderate (0.5−1.0) good (1.0−2.0), excellent (2.0−…).

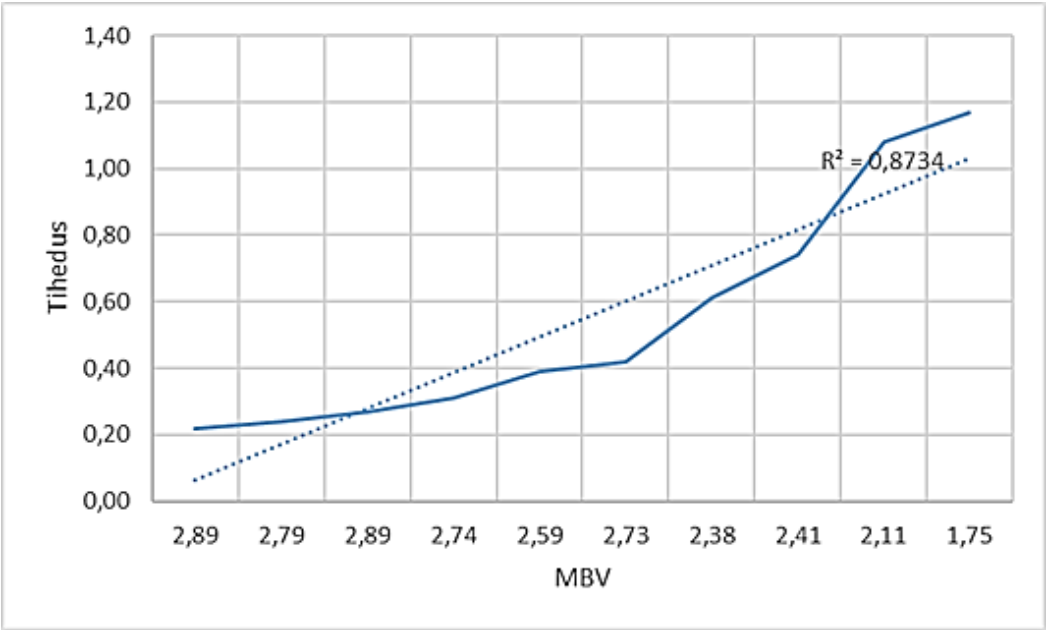

Fig. 2. The relationship between plaster density and MBV.

4. DISCUSSION

Powdered chalk has traditionally been used as a white pigment, a filler in pigments, a basis for organic pigments, and in the production of painting grounds. As an aggregate in lime plasters, powdered chalk behaves similarly to marble powder and dry lime plaster powder. Powdered chalk results in a white plaster with a yellowish tint [17].

Chalk including plasters are lime plasters. Lime plaster manufacture comprises many phases of preparation that must be meticulously completed in order to generate a high-quality product. To begin, quicklime powder is created by burning rocks (often limestone, chalk, and marble) at very high temperatures (>700 °C). After that, the lime is combined with water to create a plastic putty that can be applied and sculpted. The plaster keeps its resistant qualities and has a firm surface after drying. Technological advancements in the production of lime plaster included the inclusion of various materials to give the plaster additional features, such as greater binding capabilities or water resistance [18]. The last mentioned is a good advantage in plaster production.

The results of the experiment showed that the addition of chalk for the purpose of increasing the MBV was not practical. The more chalk added to the paper plaster, the lower the moisture-buffering capacity of the plaster. Previous experiments have shown that clay (clay plaster) added to paper plaster reduces the moisture buffering capacity of the plaster [6], [19].

In this study, we have analysed the effect of colour to the plaster. Coloured plasters are made by combining colour pigments with an uncoloured substance. An example of white pigment is chalk. Previous tests of coating paper plaster with casein paint with added chalk showed that the more layers

of paint, the lower the moisture buffering capacity [14]. When the surface of the plaster was covered with chalk-based casein paint (1, 2, 5, 10, 15, and 20 times), it was revealed that MBV steadily decreased. If the MBV was 2.70 for 1 coating, the MBV for plaster coated 10 times was 1.61, and after 15 coats, the MBV did not change but remained 1.43. If chalk is added immediately to the plaster mixture during its preparation, the MBV (paper90/chalk10) is 2.79, and a mixture consisting largely of chalk (chalk90/paper10) has an MBV of 1.75, i.e., higher than when coating the plaster with casein paint containing chalk 15 times.

5. CONCLUSIONS

The results demonstrated that MBVs of paper plaster mixtures with chalk ranged from 1.75 to 2.89. The higher the chalk content, the lower the MBV of the paper plaster. In spite of this fact, only the mix with the highest chalk content, where the ratio of chalk to paper was 90/10 by weight, had a moisture buffering capacity below 2.0, i.e., lower the level of "excellent" (MBV > 2.0).

ACKNOWLEDGEMENTS

This study has been supported by Tartu College, Tallinn University of Technology.

REFERENCES

1. Gliozzo, E., Pizzo, A., & La Russa, M.F. (2021). Mortars, Plasters and Pigments—Research Questions and Sampling Criteria. *Archaeological and Anthropological Sciences, 13*, 193. https://doi.org/10.1007/s12520-021-01393-2
2. Rode, C., Peuhkuri, R., Hanssen, K., Time, B., Svennberg, K., Arfvidsson, J. A., & Ojanen, T. (2007). Moisture buffer value of building materials. In P. Mukhopadhyaya, & M. K. Kumaran (Eds.), *Heat-Air-Moisture Transport: Measurements on Building Materials,* (pp. 33−44). American Society for Testing and Materials (ASTM).
3. Ranesi, A., Veiga, R., Rodrigues, P., & Faria. P. (2024). The Different Effect of Two Paint Systems on Moisture Buffer Capacity of Traditional and Modern Plasters. *Journal of Building Engineering 91*, 109701. https://doi.org/10.1016/j.jobe.2024.109701
4. Vares, M.−L., Ruus, A., Nutt, N., Kubjas, A., & Raamets, J. (2021). Determination of Paper Plaster Hygrothermal Performance: Influence of Different Types of Paper on Sorption and Moisture Buffering. *Journal of Building Engineering, 33,* 101830. https://doi.org/10.1016/j.jobe.2020.101830
5. Hurst, G., Ahmed, A., Taylor, S., & Tedesco, S. (2023). Anaerobic Digestion of Recycled Paper Crumb and Effects of Digestate on Concrete Performance. *Renewable Energy*, *208*, 577–582. https://doi.org/10.1016/j.renene.2023.03.061
6. Nutt, N., & Kubjas, A. (2020). Moisture Buffer Value of Composite Material Made of Clay Sand Plaster and Wastepaper. *Journal of Sustainable Architecture and Civil Engineering 27* (2), 108−115. https://doi.org/10.5755/j01.sace.27.2.25391

7. Zemite, L., Backurs, A., Vonda, K., Batjuskovs, S., Cnubbern, P., & Jansons, L. (2024). Comparative Study of Waste Management and Sampling Practices in Latvia and Estonia. *Latvian Journal of Physics and Technical Sciences*, *61* (5), 36−57. https://doi.org/10.2478/lpts-2024-0035
8. Haiba, E., Nei, L., Kutti, S., Lillenberg, M., Herodes, K., Ivask, M., ... & Laaniste, A. (2017). Degradation of Diclofenac and Triclosan Residues in Sewage Sludge Compost. *Agronomy Research*, *15* (2), 395–405.
9. Stevulova, N., Vaclavik, V., Hospodarova, V., & Dvorský, T. (2021). Recycled Cellulose Fiber Reinforced Plaster. *Materials*, *14* (11), 2986. https://doi.org/10.3390/ma14112986
10. Kaczorek, D., Basińska, M., & Koczyk H. (2023). Hygrothermal Behaviour of a Room with Different Occupancy Scenarios. *Journal of Building Engineering*, *66*, 105928. https://doi.org/10.1016/j.jobe.2023.105928
11. Aciu, C., Iluţiu – Varvara, D.A., Cobirzan, N., & Balog, A. (2014). Recycling of Paper Waste in the Composition of Plastering Mortars. *Procedia Technology*, *12*, 295-300. https://doi.org/10.1016/j.protcy.2013.12.489
12. Stevulova, N., Vaclavi, V., Hospodarova, V., & Dvorský, T. (2021). Recycled Cellulose Fiber Reinforced Plaster. *Materials*, *14* (11), 2986. https://doi.org/10.3390/ma14112986
13. Raamets, J., Nutt, N., Rudisaar, R., Nei, L., & Olle, M. (2025). Mould Resistance of Paper Plaster Made from Cellulose-Containing Waste. *Latvian Journal of Physics and Technical Sciences, 62* (1), 32−38. https://doi.org/10.2478/lpts-2025-0003
14. Nutt, N., Kubjas, A., Nei, L., & Ruus, A. (2020). The Effects of Natural Paints on the Moisture Buffering Ability of Paper Plaster. *Latvian Journal of Physics and Technical Sciences*, *57* (5), 51−60. https://doi.org/10.2478/lpts-2020-0027
15. Rode, C., Peuhkuri, R.H., Hansen, K.K., Time, B., Svennberg, K., Arfvidsson, J., & Ojanen, T. (2005). NORDTEST project on moisture buffer value of materials. In *AIVC Conference "Energy Performance Regulation: Ventilation in Relation to the Energy Performance of Buildings"* (pp. 47–52). INIVE eeig.
16. Nutt, N., Nei, L., Muoni, H., Kubjas, A., & Raamets, J. (2024). Novel Approach to Making Environmentally Friendly Plaster − Moisture Buffer Value of Plaster Made of Wastepaper and Different Glues. *Latvian Journal of Physics and Technical Sciences*, *61* (6), 59−68. https://doi.org/10.2478/lpts-2024-0043
17. Vlavogilakis, A. (2021). Fresco Mixtures with Dried Lime Plaster: Cameron's Experiments Revisited. *EXARC Journal*, *2021* (2). https://exarc.net/ark:/88735/10581
18. Friesem, D.E., Abadi, I., Shaham, D., & Grosman, L. (2019). Lime Plaster Cover of the Dead 12,000 Years Ago–New Evidence for the Origins of Lime Plaster Technology. *Evolutionary Human Sciences*, *1*, e9. http://dx.doi.org/10.1017/ehs.2019.9
19. Nutt, N., Kubjas, A., & Nei, L. (2020). Adding Waste Paper to Clay Plaster to Raise Its Ability to Buffer Moisture. *Proceedings of the Estonian Academy of Sciences*, *69* (3), 179−185. https://doi.org/10.3176/proc.2020.3.01

sciendo

LATVIAN JOURNAL OF PHYSICS
AND TECHNICAL SCIENCES
2025, N 4

DOI: 10.2478/lpts-2025-0032

A REPORT ON THE SOURCES USED FOR LEO PLASMA EXPERIMENTAL SIMULATION

A. M. Abd El-Hameed[1*], A. S. Farahat[2], L. H. Basmsm[2]

[1]Solar and Space Research Department,
National Research Institute of Astronomy and Geophysics (NRIAG),
1 EL Marsad Str., Helwan, Cairo, 4037101, EGYPT
[2]Faculty of Navigation Science and Space Technology,
Beni Suef University,
Bayad Al Arab, Beni Suef, EGYPT
*e-mail: mostafaafaf2000@yahoo.com

The simulation of the Low Earth Orbit (LEO) plasma environment is essential for understanding the effects of space plasma interactions on space systems and subsystems. Spacecraft charging and arcs are among the most significant problems related to plasma impact. These can cause variations in the physical characteristics of materials and spacecraft systems. Ground-based experimental studies are proposed to investigate the effects of a simulated LEO plasma environment. The experiments have shown that plasma effect variations depend on the applied conditions and plasma properties. One of the key factors determining the estimated plasma properties is the source used to produce plasma. Various plasma sources have been developed to simulate the conditions and properties of LEO plasma. This study presents various sources applied to generate a simulated LEO plasma environment. Different techniques used for measuring plasma characteristics are presented in the paper. Examples of the operating conditions and plasma properties are also addressed.

Keywords: *Conditions and plasma properties, LEO plasma simulation, measuring techniques, plasma sources and gas used.*

1. INTRODUCTION

Spacecraft navigates dynamic environments featuring neutral particles, plasma, radiation, and debris, necessitating designs robust against potential interactions and degradation. In (LEO) orbit, the dominant environment is the ionosphere, a relatively dense (ne ≈ 10^ (10) − 10^ (12) m^{-3}) but cool (Te ≈ 0.1−0.3 eV) plasma. Spacecraft interactions in LEO are strongly influenced by their high orbital velocity (vsc ≈ 7−8 km/s) relative to the plasma. This mesothermal flow imparts significant RAM energy (typically 5–10 eV for O^+ ions) onto impacting ions [1]. This directed energy, combined with plasma density, governs sheath structures, wake formation, and other critical interaction physics. Electrostatic effects, including surface charging, discharges, and arcing, are common results of spacecraft-plasma interactions in LEO [1]–[4]. Both charged and neutral species contribute to arc plasma evolution, potentially causing surface damage, power disruptions, contamination, and electromagnetic interference [5]–[7]. Moreover, high-voltage systems, like solar arrays, are particularly susceptible to plasma-induced degradation via discharging and arcs. This depends on the conditions and plasma properties close to the array surfaces [8]–[10]. Due to the challenges of in situ studies, laboratory simulations are vital for assessing the performance of spacecraft components and failure modes under LEO plasma conditions. Ground-based LEO simulations replicate the characteristic plasma densities and directed ion energies. These simulations employ vacuum facilities equipped with plasma sources applied to generate environments representative of LEO.

The fidelity of the ground tests critically depends on the appropriate selection and operation of the plasma source [6]. This work presents a variety of sources used for LEO plasma environmental simulation. The classification and operating principles of these sources are discussed further in the paper. Different techniques applied for measuring the plasma parameters are also outlined. The characteristics of the resulting plasma, focusing on the ability to achieve the specific density and ion energy ranges relevant to replicating LEO spacecraft interactions, are addressed in further sections.

2. PLASMA SOURCES FOR EXPERIMENTAL SIMULATIONS

Plasma sources are essential tools for simulating various space environments in ground-based facilities, allowing researchers to examine the behaviour of space instruments and materials under controlled conditions. To investigate how space instruments behave under different conditions and plasma properties, simulations using ground-based vacuum facilities have been conducted through numerous laboratory experiments. These studies consider the variation of components and plasma parameters, particularly, the density of plasma particles, electron temperature, and ion energy [1]. These parameters vary based on the operating condition of the facility, such as the discharge/ beam voltage, discharge current, gas flow rate, and facility background/ base pressure [3]. Two crucial factors for simulating LEO plasma are electrons and their thermal energy, as well as the ionized gases (e.g., Argon (Ar) or Xenon (Xe)). The

ion flux to the spacecraft surface is determined by its orbital speed, while the ion flux in the vacuum chamber depends on the operating conditions of the plasma source [5]. Therefore, various types of plasma sources are used to generate plasma. These sources are installed inside the vacuum chamber to create a plasma environment like the intended orbits. Examples of the sources considered are discussed below.

2.1. Hollow Cathode Discharge (HC)

A hollow cathode plasma source is a metal plasma source, comparable in some respects to a parallel plate capacitively coupled plasma (CCP) source. The hollow cathode (HC) discharge is a low-pressure glow discharge occurring within a cylindrical cathode cavity. The physics behind its operation involves electron emission from the cathode surface, often initiated by ion bombardment [11]. These electrons are accelerated across the cathode dark space, gaining energy to excite and ionize a sustaining gas (e.g., He, Ar). The unique cylindrical geometry enhances electron oscillation and collision probability, increasing excitation and ionization efficiency – a phenomenon known as the hollow cathode effect. Sputtering of the cathode material, caused by ion bombardment, introduces sample atoms into the plasma, leading to characteristic light emission used in spectroscopy [3]. In LEO ground-based simulations, hollow cathode discharges are employed to generate low-energy plasma for studying spacecraft material interactions with the ionosphere. For instance, studies have used hollow cathodes to simulate the plasma environment encountered by satellites, focusing on parameters like plasma density and electron temperature. The plasma properties from this source can be varied by adjusting the discharge current and gas flow rate, which affect the stability and generation of energetic ions. Increasing the discharge current or decreasing the gas flow rate can lead to higher plasma densities and electron temperatures. Gas pressure and the geometry of the hollow cathode also play crucial roles in determining plasma characteristics [3]. Resources include inert gases (He, Ar), DC power supplies (up to 1000 V), and vacuum systems (1–20 Torr) [3]. Cathode materials like Tantalum, Thoriated Tungsten, or Barium-impregnated materials are common [4]. For this particular source, efficient hollow cathode behaviour is typically satisfied at a current of approximately 30 mA and higher. This source can produce low-temperature plasma (~1 eV) [12]. Figure 1 shows the components of the HC structure [4].

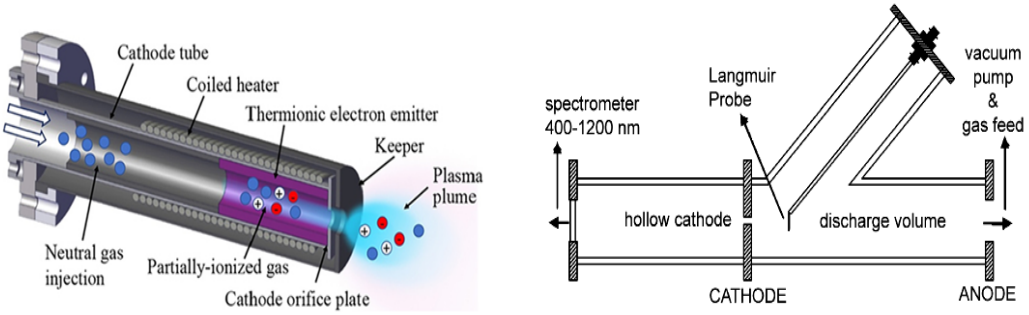

Fig. 1. Cathode schematic showing the electrode components.

2.2. Kaufman/Ion Source

The Kaufman ion source is a broad-beam, multi-aperture electron bombardment source featuring an independent discharge chamber and a double-grid ion extraction system. Its principle of operation involves introducing a working gas – commonly Argon, Xenon, or Oxygen – into the discharge chamber, where it is ionized by electrons emitted from a thermionic cathode, such as a filament or hollow cathode. A magnetic field, often generated using multipole arrangements of permanent magnets, enhances ionization by confining electrons and increasing their path length and probability of collisions with neutral atoms. Once ionization occurs, positive ions are extracted from the plasma sheath using a set of grids. The potential difference across the grids forms a controlled electric field that accelerates and collimates the ions into a well-defined beam [2]. This ion beam makes the Kaufman source suitable for simulating LEO-like plasma conditions in laboratory environments. Ground-based investigations have utilised Kaufman ion sources to replicate the low-energy, high-density ion flux typically experienced in Low Earth Orbit (LEO) [2]. For example, the scientists at NASA Marshall Space Flight Centre employed a compact Kaufman source to generate Xenon plasma for spacecraft material interaction studies under LEO-relevant ion energies and densities. These experiments generally simulate plasma environments characterised by ion densities in the range of 10^5–10^6 cm^{-3} and energies from a few to tens of electron volts (eV), allowing detailed investigation of erosion, surface charging, and material degradation [1].

This source is formed as a broad-beam, multi-aperture electron bombardment source featuring an independent discharge chamber and a double-grid ion extraction system. Its principle of operation involves introducing a working gas (e.g., Ar, Xe) into the discharge chamber, where it is ionized by electrons emitted from a cathode (filament or hollow cathode). A magnetic field, often in a multipole configuration using permanent magnets, enhances ionization efficiency by trapping electrons and increasing their collision probability with neutral gas atoms. Positive ions are then extracted from the plasma sheath into the double-grid acceleration zone. Applied potentials on these grids create an electric field that accelerates and focuses the ions into a directed beam [2]. Figure 2 (a) shows a schematic top view of the ion beam system featuring a Kaufman-type ion source. The setup includes a sample holder centrally positioned relative to the ion beam and Faraday cups for beam characterisation. The entire arrangement operates within a vacuum chamber, and an ESMS spectrometer is attached for ion analysis. The internal structure of the Kaufman-type ion source is shown in Fig. 2 (b). The gas inlet, discharge chamber, and magnetic confinement are displayed in the figure. The ions generated between the cathode and anode are extracted and accelerated through a set of grids (screen and accelerator grids) under controlled voltages [6]. Relevant ground-based LEO investigations have utilised Kaufman ion sources to simulate the ionospheric plasma environment [1]. Resources include gases such as Ar, Xe, with DC or RF power supplies, and high vacuum system [2]. Due to their stability and tunability, Kaufman sources are not only utilised in space environment simulations but also extensively applied in ion beam processing technologies such

as ion beam etching, surface modification, thin-film deposition, and electric propulsion systems. Operational requirements typically include high-vacuum systems (<10^{-3} Pa), DC or RF power supplies, and a feed gas system capable of delivering inert or reactive gases like Ar, Xe, O2, and N2 [2].

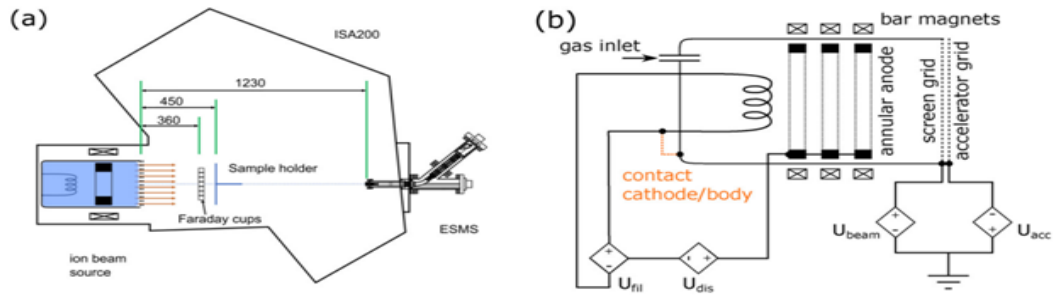

Fig. 2. (a) Schematic top view of a Kaufman-type ion source, and (b) Internal structure of the source.

At NASA's Marshall Space Flight Centre, a simple Kaufman source is used. The filament current is up to 6 A, and the bias filament negative with respect to the container is varied approximately from 20 V to 25 V. Xenon gas (Xe) is used. The image displays the source, and the schematic diagram of the applied circuit is shown in Fig. 3. The scientists apply two separate power supplies (HP 6030A), and a short pipe piece at a height of 5 cm is used for gas flow, exactly perpendicular to the filament line. Pieces of permanent magnets (PM) are used and mounted on top of the canister in a circle. This source provides an electron density of 10^6 cm^{-3} and temperatures ranging from 0.2 eV to 0.3 eV with a xenon gas flow. All of these are suitable for large chambers (Vertical 2 m diameter and 3 m height, horizontal 2 m x 2 m, respectively) [13].

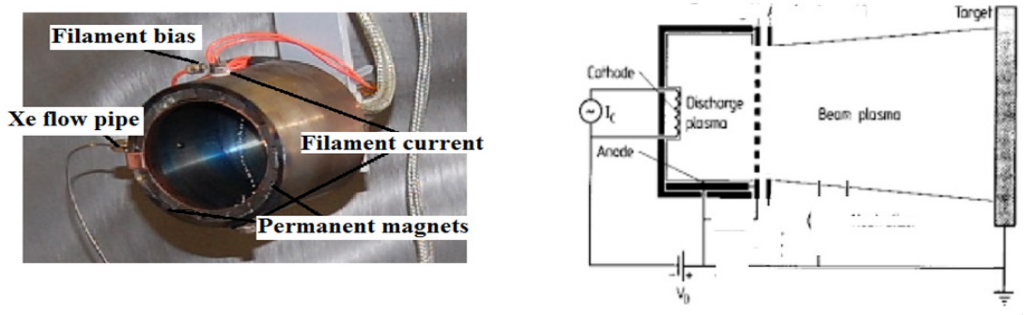

Fig. 3. Kaufman ion source used at the NASA Centre.

2.3. Penning Discharge/Plasma Ion Source

This source is one of the common sources used to simulate the LEO plasma environment. It is suitable for producing low temperature plasma with a density of

10^6 cm^{-3}. The Penning discharge plasma source operates based on the principle of applying a DC voltage between a cathode and an anode ring, with an axial magnetic field present. Electrons emitted from the cathode are trapped by the axial magnetic field, causing them to oscillate and increase their path length, thus enhancing the probability of collisions and ionization of the low-pressure gas (e.g., Xe, Ar) [6]. A feature of this source is its ability to sustain a discharge at relatively low pressures and voltages due to the efficient electron trapping and ionization processes. The outer cylinder is metallic and encircled with coils to generate the axial magnetic field required for electron trapping and enhanced ionization [7]. The electrons from the heated filament are accelerated toward the biased anode, striking the Argon atoms and leading to ionization.

This source is one of the common sources used to simulate the LEO plasma environment. It is suitable for producing low-temperature plasma with a density of ~10^6 cm^{-3}. Relevant ground-based LEO investigations have utilised penning discharges to study spacecraft interactions with the ionosphere [14]. The properties of such generated plasma involve low-temperature plasma with a density of 10^6 cm^{-3}. Operating conditions typically involve gas pressures in the range of 0.1 to 10 mTorr and magnetic field strengths from 10 to 500 Gauss [6], [15]. Resources include gases (Xe, Ar, He, H), DC voltage power supplies (20–200V, potentially up to kV), magnetic field sources (permanent magnets or electromagnets), and vacuum systems (0.1–10 mTorr) [6], [15]. Figure 4 shows a cross-sectional schematic and structure of a penning discharge plasma source [7]. Schematic diagrams and structure, for example, of the experimental configurations are shown in Fig. 5 [16], [17].

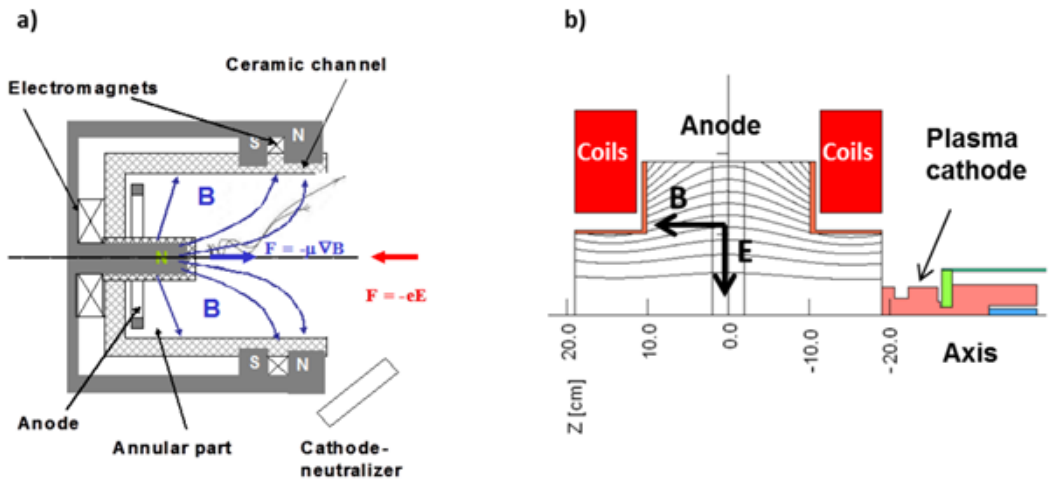

Fig. 4. (a) Cross-sectional schematic of a Penning discharge plasma source, featuring an annular ceramic channel surrounded by electromagnets that generate a radial magnetic field (B). Electrons are confined by the crossed electric (E) and magnetic (B) fields, enhancing ionization efficiency. The cathode-neutralizer maintains overall plasma neutrality. (b) Field line distribution along the axis, showing how magnetic and electric fields are structured around the anode and plasma cathode, optimising plasma confinement and extraction.

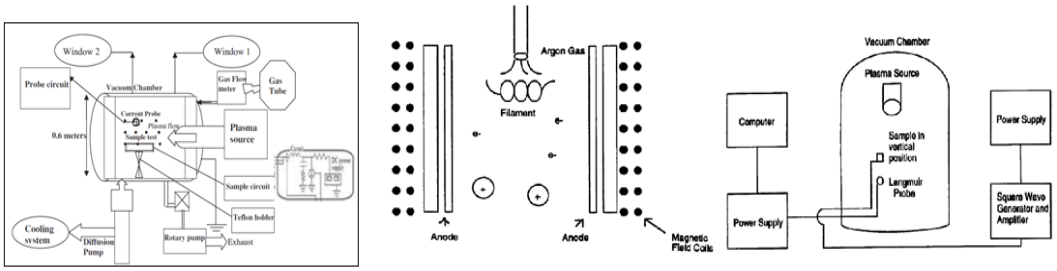

Fig. 5. Schematic diagrams of the discharge and penning ion source used in the experiment.

2.4. Electron Cyclotron Resonance (ECR)

The (ECR) is a source used to produce low-energy plasma from argon gas flow. In the work of Tahara and Masuyama (2006) [18], microwaves of maximum power of 1 kW and frequency of 2.45 GHz are introduced into a chamber of the ECR discharge. By applying an input power of 300 W, the argon gas flow rate is increased to over 8 sccm until the plasma is generated with a low temperature value of 1eV and an electron number density of 4.5 x 10^ (13) m^{-3}. Through the ECR source, stability and precise control over plasma density and electron temperature can be maintained [18].

Specific features of this plasma source include its ability to produce high-density plasmas at low pressures and the potential for independent control of ion energy and flux [19]. Relevant ground-based LEO-related works have utilised ECR plasma sources to generate plasmas with properties mimicking the ionosphere. These sources can produce low-density plasmas with adjustable ion and electron energies relevant to LEO conditions. The generated plasma properties often include electron temperatures around 0.1 eV to a few eV and ion densities in the range of 10^ (6) cm^{-3} [19]. ECR plasma sources are also uniquely applied in semiconductor processing and fusion research. Resources include a microwave source, magnets (permanent or electromagnets), a vacuum system (10^{-4} to 10^{-2} mbar), and various gases (e.g., (He, N_2, O_2, Ar) [19]. Figure 6 presents examples of multi-polar based systems driven by a single ECR plasma source [20], [21].

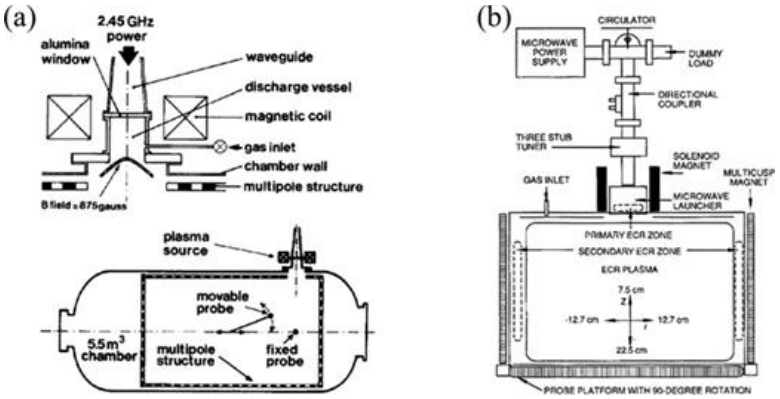

Fig. 6. Examples of multipolar based systems driven by a single ECR plasma source.

2.5. Radio Frequency (RF)

One of the more interesting configurations of plasma sources is the Radio Frequency (RF) discharge between two plane electrodes. Plasma is generated by applying the RF beam source under suitable pressure. In this arrangement, the plasma is capacitively coupled, and the power supply almost exclusively interacts with the plasma through displacement current. The "RF" discharge is typically used with electronegative gases, which can create negative plasma through the electrostatic acceleration of ions. The beam source includes a discharge tube, a water-cooled RF coil, an inert gas (argon or xenon), a viewport for observation, and a shutter. The radical beam allows for obtaining radicals from a small aperture, which is used for differential exhaust. The operating procedure involves using an RF generator (typically at 13.56 MHz) to create an oscillating electric field in CCP or an oscillating magnetic field in ICP. This field energizes electrons in the gas (e.g., Ar, O_2), leading to ionization and plasma formation [22]. A specific feature of RF sources, particularly ICP, is their ability to generate high-density plasmas with independent ion density and energy control.

While specific ground-based LEO investigations using RF plasma sources are not explicitly detailed in the provided references, RF plasma sources, especially ICPs, can generate plasmas with densities and energies relevant to the LEO environment. Researchers might utilise these sources to study the effects of simulated LEO plasma on spacecraft materials by adjusting parameters like RF power and gas pressure [23]. Resources include an RF generator, a matching network, a vacuum system, and various gases [4], [5], [22]. A diagram illustrates the "RF" principle, and the reaction mechanism is shown in Fig. 7, while the "RF" discharge and a schematic diagram illustrating the source applied and the experimental setup are shown in Fig. 8 [23], [24]. Moreover, RF plasma sources are also broadly used in industrial and research applications, including surface modification and thin film deposition [23].

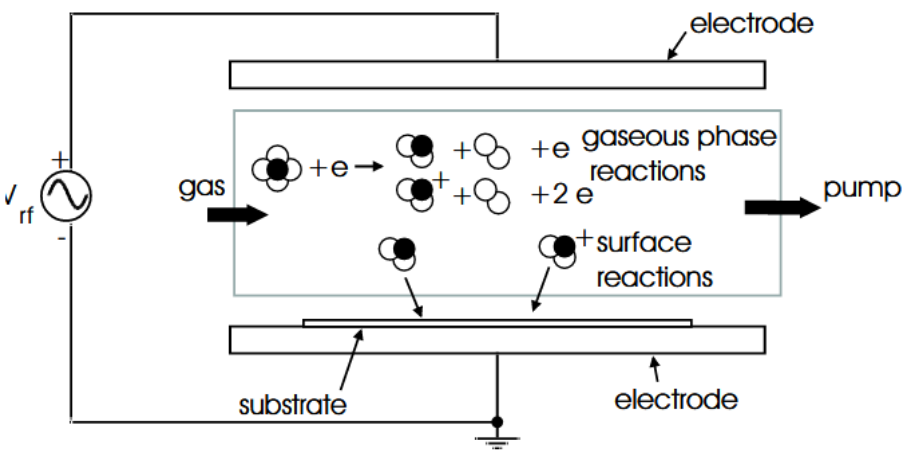

Fig. 7. "RF" principle and plasma-surface reactions.

Fig. 8. RF discharge tube and a schematic diagram of the experimental setup of the source with an RF generator (13.56 MHz).

2.6. Magnetic Filter-Equipped Plasma Source

The characteristics of the magnetically filtered plasma sources have been illustrated and discussed in previous studies by many authors [1], [25], [26]. Figure 9 shows a schematic diagram of the cross-section of the magnetic filter set and the plasma source [26]. These sources are particularly relevant for LEO ground-based simulations. For example, a 16-cm diameter plasma source using a transverse-field magnetic filter has been described for simulating LEO conditions, producing low electron temperature plasmas (0.14 to 0.4 eV) with streaming ion populations (4 eV to 6 eV) using argon "Ar" gas. These properties closely imitate the LEO environment [27]. In the work of Enloe et al. (2004) [25], the authors stated that the typical flow rate of argon gas used was about 16 sccm, resulting in a background pressure inside the vacuum chamber of 8.5 × 10^ (–5) Torr. The plasma is maintained and kept approximately steady through a bias voltage applied between the hot filament cathode and anode. The authors clarified that, for these data, although the anode was electrically separated from the discharge chamber, it was kept at the potential of the vacuum chamber. This discharge electrical potential varies between 10 V and 80 V. Typically, for the currents in the range of 10 A to 12 A required to heat the filament, there is a decrease in voltage of approximately 20 V across the filament. The system operates when the voltage required for the discharging process is held constant, while the filament current should be adjusted to regulate the current in the discharge occurring in the region between the filament cathode and the anode.

In the research work of Williams et al. (2004) [1], the authors used a power supply attached between an anode and the filament cathode to investigate the plasma created using argon gas flow. They stated that the magnetic filter was a better applicant to simulate LEO plasma. The source produces plasma of low electron temperature within the range of 0.14 eV to 0.45 eV. Rubin et al. (2009) [26] stated that the collection of experimental data in the expanding plasma downstream of the source was a good candidate for use as a LEO plasma simulator, as the expanding plasma has a very low electron temperature and contains streaming ions – the plasma environment encountered by satellites in the LEO orbit. The authors confirmed that this applied source

could produce plasma of streamed ion energies within the range of 2 eV to 5 eV and electron temperatures of 0.17 eV to 0.35 eV. These resulting data are obtained by the variation in the adaptable conditions of the operating system concerning the flow rate of the used gas and the discharge current. The authors showed that beyond the above demonstrated system, an optimisation for both the plasma source and the magnetic filter should be performed to enhance the properties of the plasma. This could help achieve the production of a higher reliability LEO plasma environment.

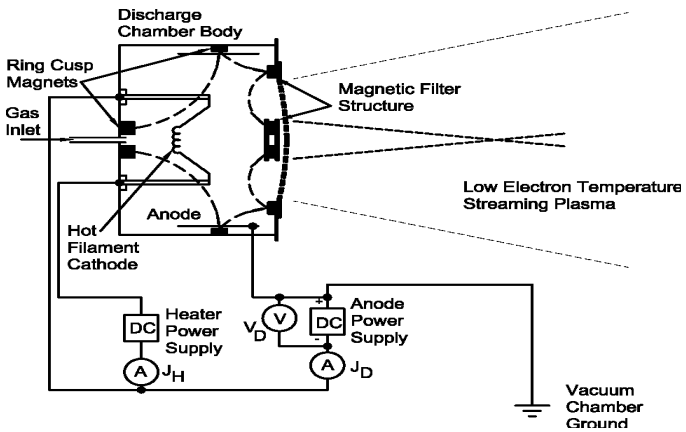

Fig. 9. Diagram of the magnetic filter set and operational plasma source.

3. PLASMA CHARACTERISATION AND MEASURING TECHNIQUES

Accurate characterisation of plasma environments is critical for validating ground-based simulations of space conditions, such as those in LEO orbit, and for understanding plasma-material interactions. While Langmuir probes are a cornerstone of plasma diagnostics, a comprehensive analysis requires a suite of advanced techniques to measure key parameters such as ion energy, electron temperature, density, and species composition. This section provides a detailed, professionally crated overview of several established diagnostic methods such as Retarding Potential Analyzers (RPAs), advanced Langmuir probe configurations, Faraday Probes, ExB Probes (Wien Filters) and non-intrusive optical techniques – each supported by in-text citations to publicly accessible sources.

3.1. Retarding Potential Analyzers (RPAs)

Retarding Potential Analyzers (RPAs) are electrostatic instruments designed to measure the ion energy distribution function (IEDF) along their axis. They are vital for studying ion acceleration, plasma potential variations, and energetic ion populations relevant to spacecraft charging and material sputtering in space environments. RPA consists of multiple grids and a collector plate. Grounded entrance grids define the acceptance angle and shield internal components from external

plasma potentials. A negatively biased grid (e.g., -50 V) repels electrons, while an ion-retarding grid with a swept positive potential filters ions based on their kinetic energy. A suppressor grid, if present, prevents secondary electron escape [28]. Design considerations of the RPAs include grid transparency and alignment to reduce collision effects, with spherical grids improving resolution for divergent flows [28]. RPAs are widely used in space plasma studies and laboratory experiments, such as ion beam and thruster plume analysis. A grid with an applied voltage repels the incoming ions. Only those ions with high enough energy to overcome the repulsion can come through the grid [29]. A diagram representing the RPA principle is shown in Fig. 10 [29]. In ground-based LEO plasma simulation, RPAs are applied for measuring ion energy distribution, which is crucial to understand spacecraft charging and erosion effects due to the ion impacts [1].

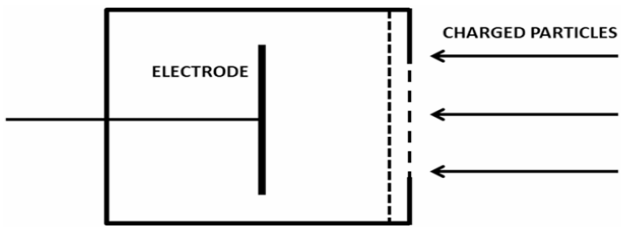

Fig. 10. RPA principal.

3.2. Langmuir Probes

Langmuir probes are considered a system used to determine the physical characteristics of plasma parameters. This instrumentation system works by inserting one or more electrodes immersed in the plasma and applying a fixed or time-varying electric potential between the electrodes. Langmuir probes provide localized measurements of plasma parameters such as electron temperature, electron density, ion density, and plasma potential through current-voltage (I-V) characteristics of an immersed electrode. There are various types of Langmuir probes including:

- Single Probe: Measures the full I-V curve but may perturb the plasma;
- Double Probe: Utilises two probes for a floating characteristic, reducing plasma perturbation [30];
- Triple Probe: Offers instantaneous measurements of electron temperature and ion density without the need for sweeping, making it ideal for fluctuating plasmas.

The simplest configuration for collecting different Langmuir probes is shown in Fig. 11 [31]. The choice of probe geometry (planar, cylindrical, and spherical) depends on the plasma environment (e.g., density, magnetic field, flow) and affects the applicable theoretical analysis for current collection [32]. In the study by Williams et al. (2004) [1], RPA was utilised to measure the ion energy distribution in ground-based LEO plasma simulation, replicating the charging effects observed on spacecraft surfaces. Polzin et al. (2023) used a Langmuir probe downstream of a magnetic fil-

ter plasma source to assess the electron temperature and plasma potential, validating the similarity to ionospheric-like LEO plasma [27].

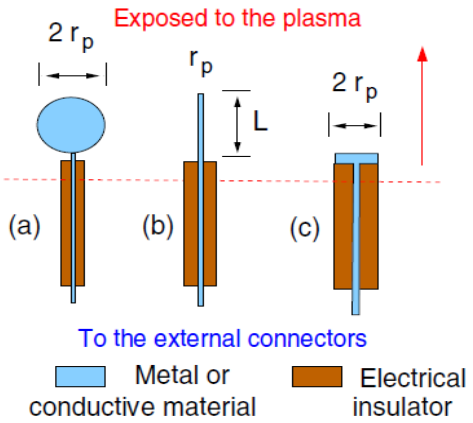

Fig. 11. Langmuir probes with radius r_p; a) spherical, b) cylindrical, and c) planar geometries.

3.3. Faraday Probes

Faraday probes measure ion current density in plasma beams, offering insights into beam profiles and thruster performance. Variants include planar probes with guard rings (PPGR) and Faraday cups (FC). The collector, which is negatively biased to repel electrons, measures ion current [33]. Materials like molybdenum could be utilised to minimise sputtering. A Faraday Cup probe is employed to measure the ion beam current from a hollow cathode discharge in order to simulate LEO plasma induced erosion on spacecraft materials [5]. The structure and components of the Faraday probe are shown in Fig. 12 [34].

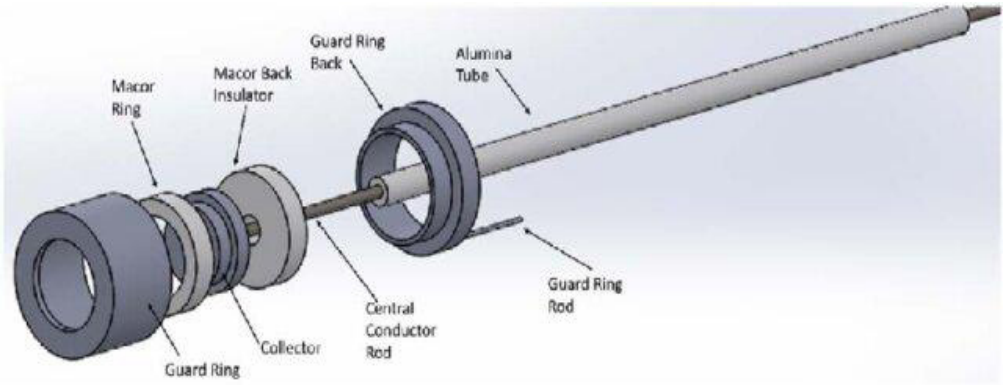

Fig. 12. View of Faraday probe.

3.4. ExB Probes (Wien Filters)

ExB probes use crossed electric (E) and magnetic (B) fields to resolve ion species by their charge-to-mass ratio. Some ions pass undeflected, while others are filtered, enabling "q / m" spectral analysis by varying (E) or (B) [35]. In the research by Yevgeny et al. (2019) [36], a modified ExB Penning discharge was analysed using both Langmuir probes and ExB energy filter to evaluate ion transport across the magnetic field, aiding in simulating magnetized LEO plasma conditions [4]. The images shown in Fig. 13 illustrate the structure of a Wien Filter probe [37].

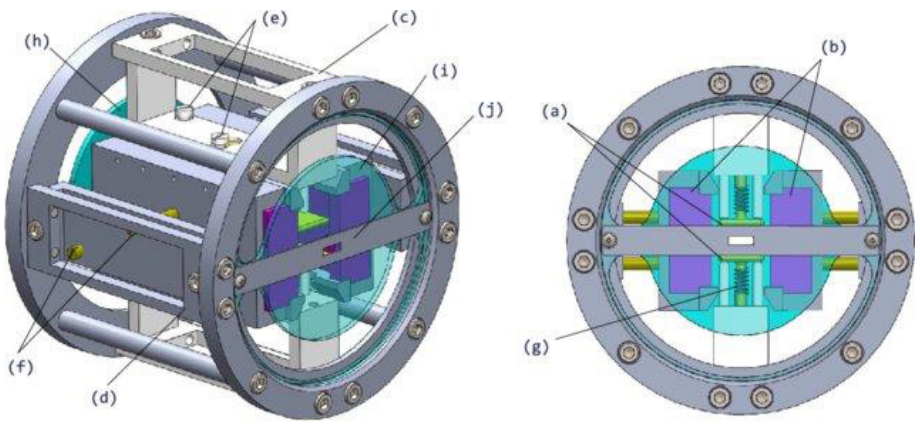

Fig. 13. Wien Filter probe: (a) electrostatic deflector plates, (b) permanent magnets, (c) deflector plate supporting bridge, (d) magnet supporting bridge, (e) deflector plate alignment screws, (f) magnet alignment screws, (g) plate positioning spring, (h) entrance plate, (i) exit plate, and (j) collimating slit.

3.5. Non-Intrusive Diagnostic Technique (NIST)

The key methods of the NIST technique can be summarised as follows [38], [39]:

- Optical emission spectroscopy (OES): This method identifies species and estimates electron temperature through the emitted light;
- LIF: It measures density and velocity distributions using laser-excited fluorescence;
- Mass Spectrometry: It is used for detailed species analysis (neutrals and ions);
- Microwave Interferometry for line-integrated electron density;
- Thomson Scattering for direct, localized measurement of temperature and electron density.

The review of NIST presented the application of optical emission spectroscopy (OES) in identifying species and excitation temperatures in low-pressure glow discharges. This application of OES parallels diagnostics in LEO plasma facilities [23]. Whilst the described diagnostics provide localized data, understanding spatial variations within the

plasma volume requires mapping. Mounting probes on computer-controlled linear or rotational translation stages enables systematic measurements at multiple points. Spatial mapping of parameters like electron density and current density of ions is achieved using translation stages, providing one, two, or three-dimensional profiles critical for validating simulations [39].

4. APPLIED CONDITIONS AND PLASMA PROPERTIES

We focus on understanding how these different sources generate plasma under specific operating conditions and how these properties compare to those found in the D, E, and F layers of the ionosphere. Examples of the conditions and plasma properties resulting from various sources applied in simulating the LEO plasma environment are given in Table 1. The data presented in the table help identify the optimal source configurations for achieving realistic ground-based simulation of LEO plasma environments.

At NASA's Marshall Space Flight Research Centre, the scientific team encountered several problems with the use of "Ar" gas in their experimental studies [13]. The use of argon resulted in higher filament temperatures and reduced lifespan. The electron temperature was consistently measured at 2–3 eV, which seems too high for "LEO" space plasma simulations. Many years ago, such a source was used in a bell jar measuring 60 cm in diameter and 90 cm in height. However, the source overheated within minutes of operation, prompting the scientists to implement water cooling resulting in a very complicated setup. Attempts to use a hollow cathode as a plasma source were unsuccessful due to the high gas flow requirement, leading to elevated neutral gas pressure in the chamber (above 100 μTorr) and increased electron temperature (above 2 eV).

Consequently, the scientists concluded that the hollow cathode was not a suitable source, particularly, for use in a small bell jar for space plasma simulation. The scientific team compared the mass number and ionization potential of argon and xenon. Argon has a mass number (A=40) and an ionization potential (I=15.2 eV), while Xenon has values of A=131 and I=12.1 eV. This indicates that an "Ar" atom spends approximately half the time in the ionization zone compared to "Xe". Additionally, xenon gas has a higher cross-section than argon. The 3.1 eV difference in ionization potentials influences the ionization probability exponent. As a result, the scientists concluded that the Kaufman source was not the optimal choice for "Ar" plasma. The use of the Kaufman source with xenon gas flowing in large chambers is more preferred and suitable to conduct real tests in a simulated plasma environment, and the magnetic field in the centre of the gap/hole is stronger than that at the cathode surface. They have recommended that plasma generation and the operating process depend on the choice of the type and operating pressure of the gas used [13]. Moreover, Goebel and Katz (2008) [33] confirmed that both "Ar" and "Xe" gases were frequently used due to their relatively high atomic mass, which allowed for better momentum transfer during sputtering processes, and their inert nature, which minimised unwanted chemical reactions with the simulated environment and spacecraft materials.

Table 1. Applied Sources and Plasma Characteristics

Source	Plasma Properties	Operating Conditions (Pressure, Voltage, Current)	Gas Species	Orbital Equivalent	Ref
Hollow Cathode Discharge	Electron temp: 0.5–1 eV, Density: 10^5–10^6 cm^{-3}	Pressure: 1–20 Torr, Voltage: up to 1000 V, Discharge Current: ≥ 30 mA	He, Ar	D Layer (low altitude, cold plasma) E Layer (denser, cooler plasma)	[3]-[5], [40]
Kaufman Ion Source	Ion energy: few eV to tens of eV, Density: 10^5–10^6 cm^{-3}	Pressure: <10^{-3} Pa (high vacuum) Beam Voltage: tunable (a few V to tens of V) DC/RF Power Supply	Ar, Xe, Kr, O_2, N_2	E Layer (mild ion density, flowing ions) Transition to F Layer (if high energies)	[1], [2]
Penning Discharge Source	Electron temp: ~0.1–2 eV, Density: ~10^6 cm^{-3}	Pressure: 0.1–10 mTorr, Magnetic Field: 10–500 Gauss, Voltage: 20–200 V (up to kV)	Ar, Xe, H_2, He	D Layer (low temp plasma) E Layer (with higher discharge energies)	[6], [7], [14]
Electron Cyclotron Resonance (ECR)	Electron temp: 0.1–few eV, Density: 10^5–10^6 cm^{-3}	Pressure: 10^{-4}–10^{-2} mbar, Microwave Power: 2.45 GHz, Magnetic Field: 875 Gauss	H_2, He, N_2, O_2, Ar	E Layer (low density plasma) F Layer (higher density at low energy)	[19], [41], [42]
Radio Frequency (RF) Plasma Source	Electron temp: adjustable, Density: 10^5–10^6 cm^{-3} (ICP mode higher)	Pressure: variable, Frequency: 13.56 MHz, Discharge Power: RF-dependent (adjustable)	Ar, O_2, Fluorocarbo	E Layer (for moderate density plasmas) Possibly lower F Layer (at higher density conditions)	[15], [22]
Magnetic Filtered Plasma Source	Electron temp: 0.14–0.4 eV, Ion energy: 4–6 eV, Low-density plasma	Moderate pressure (exact depends on setup) Transverse Magnetic Field, DC/RF Powered Plasma Generation	Ar, O_2	D Layer (cold, low energy plasma) E Layer (depending on ion energies)	[40], [27]

5. CONCLUSIONS

LEO plasma environments present unique challenges and opportunities for space missions, necessitating the development of specialised plasma sources that replicate the conditions encountered by satellites and spacecraft. To simulate these conditions on the ground for testing, various plasma sources have been developed, each with distinct operational characteristics and suitability for different applications. Plasma sources operated with different gases, such as argon or xenon, are effective for simulating LEO plasma conditions. They offer distinct advantages depending on the specific

requirements of the simulation or application, such as the need for high-density plasmas, low electron temperatures, or specific ion energies.

Understanding the properties and operational conditions of these sources is crucial for effectively replicating LEO plasma environments and advancing space research and technology. The presented work provides insight into various types of sources utilised in simulating LEO plasma environments. The explanation of factors such as the gas used to affect the properties of examples of the applied sources has been provided. Different techniques used for measuring the resulting plasma characteristics have also been given.

The recommendations to scientists and researchers include the estimation and identification of the optimum source as a LEO plasma simulator that satisfies the physical conditions and plasma parameters required to verify the best performance of the simulated ground tests for a specific application. This may help in understanding the necessity of developing experimental simulation ground tests related to the plasma sources used for testing the charging and arcs, and degradation of spacecraft structural materials due to plasma impact.

REFERENCES

1. Williams, J. D., Farnell, C. C., Shoemaker, P. B., Vaughn, J. A., & Schneider, T. A. (2004). Ground-based simulation of low earth orbit plasma conditions: plasma generation and characterization. In *8th Spacecraft Charging Technology Conference*, NASA/CP-2004-213091. SEE 20040111031. Available at: https://archive.org/stream/nasa_techdoc_20040111031/20040111031_djvu.txt
2. Raitses, Y., Chiu, Y. H., & Stratton, B. C. (2023). Characterization of a Broad Beam Kaufman-Type Ion Source Operated with CHF3 and O2. *Journal of Vacuum Science & Technology A*, *41* (5), 053104. https://doi.org/10.1116/6.0002766
3. Huber, M. C. E. (1984). Hollow Cathode Discharges – Analytical Applications. *NIST Technical Series Publications*, 89(2), 143–156. https://doi.org/10.6028/jres.089.009
4. Maldonado, S., & Choueiri, E. Y. (2023). Hollow Cathode Discharge Instability Onset in Electric Thrusters. *Journal of Applied Physics*, *135* (12), 123301. https://doi.org/10.1063/5.0188988
5. Csiky, G. A. (1969). Measurements of Some Properties of a Discharge from a Hollow Cathode. *NASA Technical Reports Server*. NASA-TN-D-4966. Available at: https://ntrs.nasa.gov/citations/19690008515
6. Kumar, R., Ahuja, R., Safvan, C. P., Kanjilal, D., & Roy, A. (2011). Development of penning ion source for 50 KeV ion accelerator. In *InPAC-2011: 5. DAE-BRNS Indian Particle Accelerator Conference*, 15–18 February 2011, New Delhi, India.
7. Dandl, R. A. (2019). Characterization of the ExB penning discharge using electrostatic probes. In *Electric Rocket Propulsion Society 36th International Electric Propulsion Conference*. 15–20 September 2019, University of Vienna, Vienna, Austria. IEPC-2019-433.
8. Vayner, B., Ferguson, D. C., & Galofaro, J. T. (2002). Experimental study of arcing on high voltage solar arrays. In *17th Space Photovoltaic Research and Technology Conference*. 11–13 September 2002, Cleveland, Ohio.
9. Vayner, B., Galofaro, J. T., & Ferguson, D. C. (2004). Interactions of High-Voltage Solar Arrays with Their Plasma Environment: Ground Tests. *Journal of Spacecraft and Rockets*, *41* (6), 1042. https://arc.aiaa.org/doi/abs/10.2514/1.B38346

10. Ferguson, D. C. (1991). *LEO Space Plasma Interactions*. N91-30249, 47–11. https://ntrs.nasa.gov/api/citations/19910020935/downloads/19910020935.pdf
11. Amemiya, H., & Ogawa, K. (1997). Characteristics of a Hollow-Cathode Discharge Containing Negative Ions. *J. Phys. D: Appl. Phys., 30* (5), 879. IOP Publishing Ltd. https://doi.org/10.1088/0022-3727/30/5/021
12. Butcher, K. S. A. (2021). Hollow Cathode Plasma Sources for Plasma Enhanced ALD and PECVD. *Coatings*, *11*(12), 1506. https://doi.org/10.3390/coatings11121506
13. Vayner Boris, V. (2024). Private communication.
14. Tyushev, M., Papahn Zadeh, M., Chopra, N. S., Raitses, Y., Romadanov, I., Likhanskii, A., … & Smolyakov, A. (2023). Mode Transitions and Spoke Structures in E×B Penning Discharge. *Physics of Plasmas*, 32, 013511. https://doi.org/10.1063/5.0238577
15. Winchester, M. R., & Payling, R. (2004). Radio-Frequency Glow Discharge Spectrometry: A Critical Review. *Spectrochimica Acta Part B, 59,* 607–666. https://doi.org/10.1016/j.sab.2004.02.013
16. Abdel-Aziz Yehia, A., Abd El-Hameed, A. M., El-Tokhy, F. S., Ghitas, A., Selim, I., & Sabry, M. (2013). Ground-Based Simulation for the Effect of Space Plasma on Spacecraft. *Advances in Space Research*, *51*, 133–142. https://doi.org/10.1016/j.asr.2012.12.014
17. Kennedy, M. D. (1995). *Low-Energy Radio-Frequency Sputtering of Copper, Anodized Aluminum, and Kapton by Argon Plasma Ions*. PhD Thesis, Department of Physics, Case Western Reserve University.
18. Tahara, H., & Masuyama, T. (2006). Ground-Based Experiment of Electric Breakdown of Spacecraft Surface Insulator in an Ambient Plasma Environment. *Plasma Science IEEE Transactions on*, *34* (5), 1959–1966. https://doi.org/10.1109/TPS.2006.883259
19. Chen, L., Zhang, Y., Zhang, S., & Li, J. (2025). Electron Cyclotron Resonance (ECR) Plasmas: A Topical Review through Representative Results Obtained over the Last 60 Years. *Journal of Applied Physics*, *137* (7), 070701. https://doi.org/10.1063/5.0249342
20. Pomathiod, L., Debrie, R., Arnal, Y., & Pelletier, J. (1984). Microwave Excitation of Large Volumes of Plasma at Electron Cyclotron Resonance in Multipolar Confinement. *Phys. Lett. A, 106* (6), 301–303. https://doi.org/10.1016/0375-9601(84)90524-3
21. Tsai, C. C., Haselton, H. H., Livesey, R. L., Schechter, D. E., & Whealton, J. H. (1991). A Compact Microwave Ion Source for Neutral Beam Injection. *Nuclear Instruments and Methods in Physics Research Section B: Beam Interactions with Materials and Atoms*, *56–57* (Part 2), 1166–1169. https://doi.org/10.1016/0168-583X(91)95749-X
22. Chabert, P., & Braithwaite, N. S. J. (2023). Impedance Matching Assistance Based on Frequency Modulation for Capacitively Coupled Plasmas. *Journal of Applied Physics*, *137* (3), 033301. https://doi.org/10.1063/5.0226790
23. Raith, A., & Hutton, R. C. (2004). Glow Discharge Optical Emission Spectrometry: A Review of Recent Developments. *Journal of Analytical Atomic Spectrometry*, *19* (1), 2–11. https://doi.org/10.1039/B309356K
24. Woo, H.-G. (2014). *Discharge Phenomena on Antenna Surface Radiating High-Power Microwave in High-Density Plasma Environment*. PhD Thesis, Kyushu Institute of Technology. Available at: https://kyutech.repo.nii.ac.jp/record/4120/files/D-227_kou_k_368.pdf
25. Enloe, C. L., Habash Krause, L., McHarg, M. G., Nava, O., Shoemaker, P. B., Ehmann, E., & Williams, J. D. (2004). *Characterization of a Plasma Source for Ground-Based Simulation of LEO Plasma Conditions.* American Institute of Aeronautics and Astronautics, AIAA-2004-5668. https://arc.aiaa.org/doi/pdfplus/10.2514/1.A34879
26. Rubin, B., Farnell, C., Williams, J., Vaughn, J., Schneider, T., & Ferguson, D. (2009). Magnetic Filter Type Plasma Source for Ground-Based Simulation of Low Earth

Orbit Environment. *Plasma Sources Science and Technology*, *18* (2), 025015. https://doi.org/10.1088/0963-0252/18/2/025015

27. Li, M., Liu, Y., & Lei, J. (2023). Design and Fabrication of a Magnetic Filter Source to Produce Ionospheric-Like Plasma. *AIP Advances*, *13* (4), 045208. https://doi.org/10.1063/5.0126931
28. Charles, C. (2009). Plasmas for Spacecraft Propulsion. *Journal of Physics D: Applied Physics*, *42* (16), 163001. https://doi.org/10.1088/0022-3727/42/16/163001
29. Lai, S. T., & Miller, C. (2020). Retarding Potential Analyzer: Principles, Designs, and Space Applications. *AIP Advances*, *10* (9), 095324. https://doi.org/10.1063/5.0014266
30. Allen, J. E. (2009). Probe Measurements in Laboratory Plasmas. *Plasma Sources Science and Technology*, *18* (1), 014004. https://doi.org/10.1088/0963-0252/18/1/014004
31. Cho, M., Ramasamy, R., Hikita, M., Tanaka, K., & Sasaki, S. (2002). *Journal of Spacecraft and Rockets*, *39* (3), 392–399. https://doi.org/10.2514/2.3838
32. Chen, F. F. (2006). *Introduction to Plasma Physics and Controlled Fusion* (2nd ed.). Springer.
33. Goebel, D. M., & Katz, I. (2008). *Fundamentals of Electric Propulsion: Ion and Hall Thrusters*. Wiley.
34. Yildiz, M. S., & Celik, M. (2019). Plume Diagnostics of BUSTLab Microwave Electrothermal Thruster Using Langmuir and Faraday Probes. *Plasma Science and Technology*, 21 (4), 045505. https://doi.org/10.1088/2058-6272/aaf280
35. Aanesland, A., Meige, A., & Chabert, P. (2009). Electric Propulsion Using Ion-Ion Plasmas. *Journal of Physics: Conference Series*, *162*, 012009. https://doi.org/10.1088/1742-6596/162/1/012009
36. Raitses, Y., Rodriguez, E., Skoutnev, V., Powis, A., Kraus, B., & Kaganovich, I. (2019). Characterization of the ExB Penning Discharge Using Electrostatic Probes. In *36th International Electric Propulsion Conference*, IEPC-2019-433. 15–20 September, 2019, University of Vienna, Vienna, Austria. Available at: https://htx.pppl.gov/conferencepapers.html
37. Cortázar, O. D., Megía-Macías, A., Tarvainen, O., Kalvas, T., & Koivisto, H. (2015). The Relationship Between Visible Light Emission and Species Fraction of the Hydrogen Ion Beams Extracted from 2.45 GHz Microwave Discharge. *Review of Scientific Instruments*, *86* (8), 083309. https://doi.org/10.1063/1.4928475
38. Griem, H. R. (1997). *Principles of Plasma Spectroscopy*. Cambridge University Press.
39. Mazouffre, S. (2016). Laser-Induced Fluorescence Spectroscopy for Electric Propulsion. *Plasma Sources Science and Technology*, *25* (3), 033002. https://doi.org/10.1088/0963-0252/25/3/033002
40. Lu, C., Zhang, Z., Sun, B., Zhang, X., & Li, J. (2023). Transition Characteristics in an Indium Tin Oxide Hollow Cathode. *Physics of Plasmas*, *32* (3), 033509. https://doi.org/10.1063/5.0135271
41. Patil, S., Sharma, S., Sengupta, S., Sen, A., & Kaganovich, I. (2022). Electron Bounce-Cyclotron Resonance in Capacitive Discharges at Low Magnetic Fields. *Physical Review Research*, *4* (1), 013059. https://doi.org/10.1103/PhysRevResearch.4.013059
42. Xie, Z.-Q. (1997). State of the art of ECR ion sources. In *Proceedings of the 1997 Particle Accelerator Conference* (Cat. No.97CH36167), (pp. 2662–2666). 16 May 1997, Vancouver, BC, Canada. https://doi.org/10.1109/PAC.1997.752725